

SPATIOTEMPORAL VARIABILITY ANALYSIS OF WATER HYACINTH (*Eichhornia crassipes*) AND ITS IMPACT ON THE LAKE TANA ECOSYSTEM USING REMOTE SENSING TECHNOLOGY

MARCH 2025

GETACHEW BAYABLE TIRUNEH

SPATIOTEMPORAL VARIABILITY ANALYSIS OF WATER HYACINTH (*Eichhornia crassipes*) AND ITS IMPACT ON THE LAKE TANA ECOSYSTEM USING REMOTE SENSING TECHNOLOGY

Dissertation Submitted in Partial Fulfillment of the Requirements for the Degree of
Doctor of Philosophy
in Environmental Engineering for Symbiosis
from the Graduate School of Science and Engineering, Soka University

By

Getachew Bayable Tiruneh

Supervisor: Prof. Dr. Victor S. Kuwahara

Soka University
Hachioji, Tokyo, Japan
March 2025

Copyright ©

WE, THE UNDERSIGNED MEMBERS OF THE COMMITTEE, HAVE APPROVED
THIS DISSERTATION

Spatiotemporal Variability Analysis of Water Hyacinth (*Eichhornia crassipes*) and Its
Impact on the Lake Tana Ecosystem Using Remote Sensing Technology

Dissertation Committee:

Prof. Dr. Victor S. Kuwahara
Soka University

Prof. Dr. Shinjiro Sato
Soka University

Prof. Dr. Hiroki Imamura
Soka University

Dr. Kanako Ishikawa
Lake Biwa Environmental Research Institute

Soka University, Tokyo

March 2025

ACKNOWLEDGEMENTS

First and foremost, I would like to express my deepest gratitude to my supervisor, Prof. Dr. Victor S. Kuwahara. His tireless guidance and unwavering support were invaluable throughout the journey of this dissertation. Accomplishing this task would have been immensely challenging without his expertise and encouragement. I sincerely thank my collaborative research advisors from Bahir Dar University Dr. Mulatie Mekonnen and Dr. Solomon Addisu, for their insightful guidance, steadfast support, and constructive feedback.

I extend my heartfelt gratitude to my esteemed dissertation committee members, Prof. Dr. Shinjiro Sato, Dr. Kanako Ishikawa, and Prof. Dr. Hiroki Imamura, for their willingness to review my dissertation and for providing invaluable critical comments and constructive feedback.

I am also grateful to the SATREPS EARTH Project Theme One members, especially Mr. Yoshiyuki Hirata, Dr. Ji Cai, Dr. Chunmeng Jiao, and Mr. Zelalem Liyew. Their invaluable advice and continuous feedback during our monthly meetings and throughout the manuscript writing process significantly enriched the quality of my work.

I extend sincere appreciation to the budget supporters who facilitated my research endeavors. Special thanks to Soka University for the research assistant's support and for providing the necessary resources, including computing facilities. I am also grateful to MEXT for the monthly stipend. Furthermore, I gratefully acknowledge the financial support provided by the Science and Technology Research Partnership for Sustainable Development (SATREPS), funded by the Japan Science and Technology Agency (JST) and the Japan International Cooperation Agency (JICA), as well as Bahir Dar University.

My heartfelt thanks also go to all Laboratory of Biological and Optical Oceanography members, including Koichi Yano, Robel Milashu, and Brittany Ashley, for their unwavering support in the laboratory. Your invaluable assistance is deeply appreciated.

Finally, I would like to express my profound gratitude to my family for their unwavering support and understanding throughout this journey. To my beloved wife, Hulualem Tebeje, thank you for caring for our children and managing household

responsibilities during my Ph.D. studies. I am also deeply indebted to my family members and relatives for their endless encouragement.

I extend my heartfelt thanks to everyone who contributed to this endeavor. Your support and dedication have been invaluable, and I sincerely appreciate each of your roles in this achievement.

Contents

ACKNOWLEDGEMENTS.....	v
ABSTRACT	xv
CHAPTER ONE.....	1
1. GENERAL INTRODUCTION	1
1.1 Overview of water hyacinth (<i>Eichhornia crassipes</i>).....	1
1.2 Impacts of water hyacinth	2
1.2.1. Impact of water hyacinth on water loss.....	3
1.2.2. Impact of water hyacinth on water quality parameters	4
1.3 Remote sensing of water hyacinth and its detection methods	5
1.4 Spatial and temporal distribution of water hyacinth.....	10
1.5. Water quality parameters	11
1.6. Goal and objectives of research.....	15
CHAPTER TWO.....	16
2. DETECTION OF WATER HYACINTH (<i>Eichhornia crassipes</i>) IN LAKE TANA, ETHIOPIA, USING MACHINE LEARNING ALGORITHMS	16
2.1. INTRODUCTION.....	16
2.2. MATERIALS AND METHODS.....	18
2.2.1. Description of the Study Area.....	18
2.2.2. Data types and processing	21
2.2.3. Sample point generation and water hyacinth detection methods	23
2.2.4. Accuracy assessment	26
2.3. RESULTS.....	27
2.3.1. Water hyacinth spectral reflectance curve.....	27
2.3.2. Performances of the machine learning algorithms	28

2.3.3. Feature importance	36
2.4. DISCUSSION	37
2.5. CONCLUSIONS	40
3. SPATIOTEMPORAL VARIABILITY OF WATER HYACINTH (<i>Eichhornia crassipes</i>) AND ITS ASSOCIATED WATER LOSS IN LAKE TANA, ETHIOPIA....	41
3.1. INTRODUCTION.....	41
3.2. MATERIALS AND METHODS.....	44
3.2.1. Data and processing	44
3.2.2. Sample point generation and classification	45
3.2.3. Water loss estimation.....	46
3.3. RESULTS.....	48
3.3.1. Spatiotemporal distribution of water hyacinth	48
3.3.2. Water hyacinth evapotranspiration and its associated water loss	51
3.4. DISCUSSION	54
3.4.1. Spatiotemporal distribution of water hyacinth	54
3.4.2. Water hyacinth evapotranspiration and its associated water loss	57
3.5. CONCLUSION.....	58
4. SPATIOTEMPORAL VARIABILITY OF LAKE SURFACE WATER TEMPERATURE AND WATER QUALITY PARAMETERS AND ITS INTERRELATIONSHIP WITH WATER HYACINTH BIOMASS IN LAKE TANA, ETHIOPIA	60
4.1. INTRODUCTION.....	60
4.2. MATERIALS AND METHODS.....	64
4.2.1 Data collection and processing.....	64

4.2.2 Water hyacinth biomass and water quality parameter estimation.....	66
4.2.3 Validation of MODIS LSWT and Sentinel-2 water quality indices	68
4.2.4. Data analysis	72
4.3. RESULTS.....	74
4.3.1 Spatial distribution of lake surface water temperature.....	74
4.3.2 Trend and inter-annual variability analysis of lake surface water temperature	75
4.3.3 Spatial distribution of turbidity and chlorophyll <i>a</i> (Chl- <i>a</i>) indices	82
4.3.4 Temporal variability analysis of turbidity and Chl- <i>a</i> indices.....	83
4.4. DISCUSSION	87
4.4.1 Spatiotemporal variability analysis of lake surface water temperature.....	87
4.4.2 Spatiotemporal variability analysis of turbidity and Chl- <i>a</i>	91
4.5. CONCLUSION.....	96
CHAPTER FIVE	98
5. GENERAL DISCUSSION.....	98
5.1. Introduction.....	98
5.2. Findings and potential applications.....	99
5.2. 1. Performances of the machine learning algorithms for water hyacinth detection	99
5.2.2. Spatiotemporal dynamics of water hyacinth and associated water loss due to water hyacinth evapotranspiration	100
5.2.3. Spatiotemporal distribution of physical and biological water quality parameters and their relationship with water hyacinth biomass.....	101
5.3 Integration of NDVI-based spatial distribution of water hyacinth into a portal system.....	103
5.4 Future research directions	104
REFERENCES	107

Tables

Table I-1: Summary of remote sensing satellite and water hyacinth detection methods in prior studies	9
Table II-1. Landsat-8 (OLI) Level 2 Tier 1 and Sentinel-2 (MSI) Level 2A surface reflectance bands used in the study	22
Table II-2. Equations and sources of spectral indices used in this study	23
Table III-1. Annual maximum (Max.) water hyacinth spatial coverage, lake surface area, and expansion rates (2015–2023).	51
Table III-2. The Modified Mann–Kendall trend test analysis of water hyacinth evapotranspiration (2016–2023).....	53
Table III-3. The Modified Mann–Kendall trend test analysis of water loss due to water hyacinth evapotranspiration (2016–2023).....	54
Table IV-1. Summary of satellite data used in the present study	66
Table IV-2. Evaluation of chlorophyll- <i>a</i> estimation algorithms..	67
Table IV-3. The Modified Mann-Kendall trend test analysis of spatial average LSWT (°C) (2001-2022)	77
Table IV-4. The Modified Mann-Kendall trend test analysis of interannual variability of LSWT (2001-2022)	81
Table IV-5. Correlation between spatially averaged water hyacinth biomass and mean LSWT, turbidity, and Chl- <i>a</i> index in the northeastern region of Lake Tana near water hyacinth-infested areas (January 2016 – December 2022).....	86

Figures

Figure I-1. Worldwide distribution of water hyacinth (Yan et al., 2017).....	2
Figure I-2. Number of publications on remote sensing of water hyacinth in the Scopus database (1988–2023).....	6
Figure II-1. Map of Lake Tana including land elevation, depth, and <i>in-situ</i> sampling locations.....	19
Figure II-2. Mean monthly rainfall (blue) and air temperature (orange) in the Lake Tana region (1981–2022), including standard deviation for both variables.....	20
Figure II-3. Water evaporation (Ev) of Lake Tana, derived from MODIS data, covering the period from January 2015 to December 2023	21
Figure II-4. Average spectral reflectance curves of different land-use/cover types in and around Lake Tana from Sentinel-2 during (a) post-rainy season (October 2021), (b) dry season (January 2022), (c) pre-rainy season (March 2022), and (d) rainy season (June 2022).....	28
Figure II-5. Comparison of machine learning classifiers for the post-rainy season (October 2021): Sentinel-2 imagery classified by (a) CART, (b) RF, and (c) SVM, and Landsat-8 imagery classified by (d) CART, (e) RF, and (f) SVM land-use/cover maps. The black oval shapes highlight areas of misclassification.....	29
Figure II-6. Comparison of machine learning classifiers for the dry season (January 2022): Sentinel-2 imagery classified by (a) CART, (b) RF, and (c) SVM, and Landsat-8 imagery classified by (d) CART, (e) RF, and (f) SVM land-use/cover maps. The black oval shapes highlight areas of misclassification.	30
Figure II-7. Comparison of machine learning classifiers for the pre-rainy season (March 2022): Sentinel-2 imagery classified by (a) CART, (b) RF, and (c) SVM, and Landsat-8	

imagery classified by (d) CART, (e) RF, and (f) SVM land-use/cover maps. The black oval shapes highlight areas of misclassification.....	31
Figure II-8. Comparison of machine learning classifiers for the summer season (June 2022): Sentinel-2 imagery classified by (a) CART, (b) RF, and (c) SVM, and Landsat-8 imagery classified by (d) CART, (e) RF, and (f) SVM land-use/cover maps. The black oval shapes highlight areas of misclassification.	32
Figure II-9. Comparison of average overall accuracy (OA) and <i>Kappa</i> coefficient (KC) for the three classifiers applied to Sentinel-2 MSI and Landsat-8 OLI imagery.	34
Figure II-10. Comparison of average user accuracy, producer accuracy, and F1-score for the three classifiers applied to Sentinel-2 imagery	35
Figure II-11. Comparison of average user accuracy, producer accuracy, and F1-score for the three classifiers applied to Landsat-8 imagery	36
Figure II-12. Relative feature importance of the RF classified images for post-rainy season (a), dry season (b), pre-rainy season (c), and (d) rainy season from Sentinel-2 images.	37
Figure III-1. Comparison of Ev estimates from the MODIS MOD16A2 gap-filled dataset with Ev estimates by Damtie et al. (2021) based on National Meteorological Agency data from Bahir Dar station (January–December 2020)	47
Figure III-2. Spatiotemporal distribution of water hyacinth in the northeastern section and across Lake Tana, showing maximum spatial coverage from 2015 to 2023 (a), and a time series of water hyacinth spatial coverage and water surface area from October 2015 to December 2023 (b)..	50
Figure III-3. Time series of water hyacinth evapotranspiration and air temperature from October 2015 to December 2023	52
Figure III-4. Time series of water surface area and Precipitation (2015–2022).....	56

Figure III-5. Time series of water hyacinth evapotranspiration and associated water loss from October 2015 to December 2023.	58
Figure IV-1. Regression analyses include (a) linear regression comparing MODIS Terra LSWT with measured water temperature, (b) linear regression comparing Sentinel-2 NDTI with <i>in-situ</i> turbidity, (c) linear regression comparing Sentinel-2 NDCI with <i>in-situ</i> Chl- <i>a</i> , (d) quadratic polynomial regression comparing Sentinel-2 NDTI with <i>in-situ</i> turbidity, and (e) quadratic polynomial regression comparing Sentinel-2 NDCI with <i>in-situ</i> Chl- <i>a</i>	70
Figure IV-2. Mean seasonal and annual spatial distribution of LSWT derived from MODIS Terra (2001–2022) along depth contours at two-meter (2 m) intervals across the dry season (December–February), pre-rainy season (March–May), rainy season (June–August), and post-rainy season (September–November).....	75
Figure IV-3. Mean seasonal and annual spatial slope of LSWT for Lake Tana (2001-2022) based on a pixel-based linear regression model	76
Figure IV-4. Seasonal and annual time series and trends of spatial average (a) LSWT (°C) over two decades (2001-2022), (b) Normalized Difference Turbidity Index (NDTI)-represent turbidity (2016-2022), and (c) Normalized Difference Chlorophyll Index (NDCI)-represent Chl- <i>a</i> (2016-2022)	78
Figure IV-5. Innovative trend analysis of seasonal and annual spatial average LSWT (°C) time series, with the X-axis representing the first half (2001-2011) and the Y-axis representing the second half (2012-2022)	79
Figure IV-6. (a) Interannual variability of LSWT based on the coefficient of variation (CV%) (2001–2022); (b) mean seasonal spatial distribution of the Normalized Difference Turbidity Index (NDTI, representing turbidity levels) with two-meter (2 m) interval depth contours; and (c) mean seasonal spatial distribution of the Normalized Difference Chlorophyll Index (NDCI, representing Chl- <i>a</i> concentration) with two-meter (2 m) interval depth contours (2016–2022).....	82

Figure IV-7. Predicted (a) turbidity and (b) Chl- <i>a</i> concentrations of Lake Tana (June 2023).	83
Figure IV-8. Seasonal spatial slopes of NDTI and NDCI based on a pixel-based linear regression model (2016-2022).	85
Figure IV-9. Spatial distribution of water hyacinth biomass (WH) in the post-rainy season (2015–2022) in the northeastern part of Lake Tana, along with a time series graph showing WH biomass trends from 2016 to 2022.	89
Figure IV-10. (a) Time series of LSWT and air temperature (2001–2021), showing a positive and statistically significant correlation ($r = 0.56$, $P < 0.05$) between mean annual LSWT and air temperature. and (b) Time series of Lake Surface Water Temperature Anomaly (LSWTA), Pacific Ocean Sea Surface Temperature Anomaly (SSTA) in the Niño 3.4 region, and Global Tropics SSTA (GTSSTA) (2001–2022). A positive and statistically significant correlation was found between LSWTA and Niño 3.4 SSTA ($r = 0.52$) and between LSWTA and GTSSTA ($r = 0.43$, $P < 0.05$).	91
Figure V-1. Portal-based visualization of water hyacinth spatial distribution and coverage in Lake Tana, derived using NDVI threshold values (0.6 to 1), enabling temporal filtering from October 2015 onwards based on Sentinel-2 data.	103

ABSTRACT

Water is the most important resource on Earth, providing essential socio-economic and ecological benefits. However, freshwater sources like Lake Tana are declining due to pollution, agricultural expansion, urbanization, climate change, and poor watershed management. These factors degrade water quality and promote the spread of invasive aquatic weeds like water hyacinth, a major concern for environmentalists and water resource managers due to its negative impacts on aquatic life, ecosystems, and human livelihoods. In tropical highland lakes like Lake Tana, Ethiopia, water hyacinth affects biodiversity, fisheries, navigation, tourism, and water quality, while also causing water loss through higher evapotranspiration rates in infested areas. Yet, in its native ecosystems, water hyacinth enhances habitat complexity, provides shelter and feeding grounds, and aids in water purification by absorbing pollutants. Understanding the distribution and ecological impact of water hyacinths is crucial for developing strategies that mitigate its harmful effects while recognizing its potential benefits. Traditional field surveys are costly and time-consuming, but satellite data provides a more efficient alternative for monitoring water hyacinth and water quality across large areas. Combining satellite imagery with *in-situ* measurements enables frequent and comprehensive monitoring of lake surface water temperature (LSWT), turbidity, and chlorophyll-*a* (Chl-*a*). Previous studies on water hyacinth in Lake Tana primarily used parametric algorithms, such as maximum likelihood classifiers with spectral bands, and relied on lower-resolution Landsat imagery (Landsat-5 and -8), with most conducted before 2019. However, updated information on water hyacinth distribution since 2019 is needed for effective management strategies. Besides, water loss due to water hyacinth evapotranspiration has not been thoroughly explored, with existing studies in Lake Tana using plant coefficients from other regions, highlighting the need for further research with region-specific coefficients. Additionally, research on the spatiotemporal variability of physical and biological water quality parameters, such as LSWT, turbidity, and Chl-*a*, is spatially limited and temporally fragmented. Furthermore, the relationship between water hyacinth biomass and water quality parameters has not been thoroughly investigated. Therefore, the overall objective of this doctoral research was to analyze the spatiotemporal

distribution of water hyacinth and its impact on hydrology and water quality using remote sensing technology.

As the demand for accurate mapping of water hyacinth using machine learning algorithms on satellite data increases, comparing the performance of different algorithms is essential to identify the most effective detection approach. Chapter Two aimed to evaluate the performance of Classification and Regression Tree (CART), Random Forest (RF), and Support Vector Machine (SVM) algorithms in detecting water hyacinths using Landsat-8 and Sentinel-2 imagery within the Google Earth Engine (GEE) platform. To capture seasonal variations, cloud-masked monthly median composite data from October 2021, January 2022, March 2022, and June 2022 were selected to represent the post-rainy, dry, pre-rainy, and rainy seasons, respectively. To enhance detection accuracy, spectral indices were combined with spectral bands. All methods achieved over 95% overall accuracy with Sentinel-2 data and over 90% with Landsat-8 data, with F1 scores for water hyacinth detection exceeding 93% across all methods and datasets. Although the differences in performance were small, Random Forest (RF) emerged as the most accurate. The overall accuracy and F1 score for the water hyacinth class were highest during the post-rainy season for all classifiers, while the lowest values were observed during the dry season. These findings indicate that RF is the most effective algorithm for detecting water hyacinth, and the post-rainy season has the highest accuracy across all classifiers, making it the optimal period for detection in Lake Tana.

Chapter Three examines the spatiotemporal dynamics of water hyacinth and its associated water loss due to evapotranspiration. Cloud-masked Sentinel-2 Level-1C imagery, combined with spectral bands and indices, was utilized to estimate the weed's spatial and temporal distribution. The Random Forest (RF) algorithm was applied to assess the spatiotemporal distribution of water hyacinths from 2015 to 2023. MODIS MOD16A2 potential evapotranspiration (PET) data from NASA's AppEEARS platform were used to estimate lake water evaporation. High populations of water hyacinths were observed in the northeastern sector of Lake Tana. From 2015 to 2023, the spatial coverage of water hyacinth increased significantly at a rate of $0.06 \text{ km}^2/\text{month}$ ($P < 0.05$), peaking in the post-rainy season

and reaching its lowest levels in the pre-rainy season. The annual maximum expansion rates increased significantly from 2015 to 2019 but declined by 4%, 1%, and 52% in 2020, 2021, and 2022, respectively, likely due to removal efforts. A significant positive correlation between water hyacinth coverage and lake surface area suggests that lake expansion into floodplains creates optimal conditions for weed proliferation, especially in shallow, nutrient-rich areas. Water loss due to water hyacinth evapotranspiration also increased significantly, totaling approximately 176 million m³ from October 2015 to December 2023, representing about 0.61% of the lake's total volume. This water loss was most pronounced in the post-rainy season and lowest in the pre-rainy season, highlighting the substantial impact of water hyacinth on Lake Tana's hydrology.

Chapter Four investigates the spatiotemporal variability of lake surface water temperature (LSWT), turbidity, and chlorophyll-*a* (Chl-*a*) and their association with water hyacinth biomass in Lake Tana. The study utilized MODIS Land/LSWT, Sentinel-2 MSI imagery, and *in-situ* water quality data. Validation results showed strong positive correlations between MODIS LSWT and measured water temperature ($r = 0.90$), *in-situ* turbidity and the normalized difference turbidity index (NDTI, $r = 0.92$), and *in-situ* Chl-*a* and the normalized difference chlorophyll index (NDCI, $r = 0.84$). LSWT trends varied across the lake, with increasing trends in the northeastern, northwestern, and southwestern regions, and decreasing trends in the western, southern, and central areas (2001–2022). The spatial average LSWT trend decreased significantly in the pre-rainy (0.01 °C/year), rainy (0.02 °C/year), and post-rainy seasons (0.01 °C/year), but increased non-significantly in the dry season (2001–2022, $P < 0.05$). Similarly, spatial average turbidity decreased significantly in all seasons except in the pre-rainy season (2016–2022). Spatial average Chl-*a* also decreased significantly in the pre-rainy and rainy seasons, while showing a non-significant increasing trend in the dry and post-rainy seasons (2016–2022). Water hyacinth biomass showed a non-significant positive correlation with LSWT but significant negative correlations with turbidity and Chl-*a*, indicating that water hyacinth slightly increases LSWT while reducing turbidity and phytoplankton biomass. High spatiotemporal variability was observed in LSWT, turbidity, and Chl-*a*, accompanied by overall decreasing trends.

This study identified Random Forest (RF) as the most accurate method for detecting water hyacinth and provided the first comprehensive quantification of its spatiotemporal distribution and ecological impacts using remote sensing technology. The findings highlight the importance of integrated management strategies to mitigate the negative effects of water hyacinth while acknowledging its potential role in water purification. This research offers valuable insights for assessing water hyacinth's spatial and temporal distribution, its ecological impacts, and the implications for sustainable water resource management, environmental protection, and pollution prevention. These insights enable policymakers and stakeholders to make informed decisions and develop strategic plans.

CHAPTER ONE

1. GENERAL INTRODUCTION

1.1 Overview of water hyacinth (*Eichhornia crassipes*)

Water hyacinth (*Eichhornia crassipes*) is a perennial, herbaceous, free-floating aquatic plant native to the Amazon Basin (Hill & Coetzee, 2008). Characterized by its broad, waxy, canopy-like leaves and purple, clustered flowers that grow in spikes, the plant can vary in height from a few centimeters to nearly a meter, with leaves approximately 15–20 cm in length and width (Harun et al., 2021; Jafari, 2010). Water hyacinth reproduces both sexually through seed propagation and asexually through stolon vegetative reproduction, contributing to its invasive success (Harun et al., 2021). Its seeds can remain viable for up to 20 years and may germinate in moist soil or warm, shallow waters (Lu et al., 2007). The plant's high dispersal capability, buoyant propagules, and well-developed phenotypic plasticity enable it to adapt effectively to both its native and introduced environments (Zhang et al., 2010). Several factors influence the rate of water hyacinth infestation, including temperature, nutrient availability, salinity, light, wind, water currents, carbon dioxide levels, waves, turbidity, and changes in water levels (Harun et al., 2021; Wilson et al., 2005; Zarkami et al., 2021). Generally, higher temperatures and increased nitrogen and phosphorus levels promote its growth (Wilson et al., 2005; Zarkami et al., 2021), while higher salinity levels can inhibit proliferation by reducing growth and increasing mortality rates, affecting invasions in coastal areas (Bick et al., 2020).

Water hyacinth, native to Brazil, began spreading globally in the 19th century (Hill & Coetzee, 2008). Introduced as an ornamental plant, it reached North America in the late 1800s, Africa in the early 1900s, and Europe by the 1930s (Yan et al., 2017). Today, it has naturalized in over 50 countries, including regions in Central America, Asia, Australia, and New Zealand (Dersseh et al., 2019b; Yan et al., 2017; Figure I-1). Since the late 1800s, the species has spread worldwide through human activities, bird migration, animal movement, and interconnected watersheds and rivers (Churko et al., 2024). Water hyacinth thrives in

favorable environmental conditions, particularly high temperatures, and nutrient-rich waters, making it more prevalent in tropical and subtropical water bodies where these factors support its proliferation. In Ethiopia, water hyacinth was first introduced as an ornamental species in 1965 around the Aba Samuel Dam, later spreading to surrounding rivers and lakes (Dersseh et al., 2019b). Although there is no clear record of how or when the plant was introduced to Lake Tana, Ethiopia's largest freshwater lake, its presence was officially recognized in 2011 (Wondie et al., 2012). Since then, water hyacinth has spread at an alarming rate due to its rapid growth rate, ease of propagation, and high adaptability to harsh conditions (Cai et al., 2023; Yan et al., 2017), as well as favorable environmental conditions such as high temperatures and nutrient availability (Abebe et al., 2023; Churko et al., 2024; Dersseh et al., 2020). Understanding the spatiotemporal distribution and growth patterns of water hyacinths in Lake Tana is crucial for developing targeted and effective mitigation strategies essential for protecting the lake's ecosystem and ensuring sustainable water resource management.

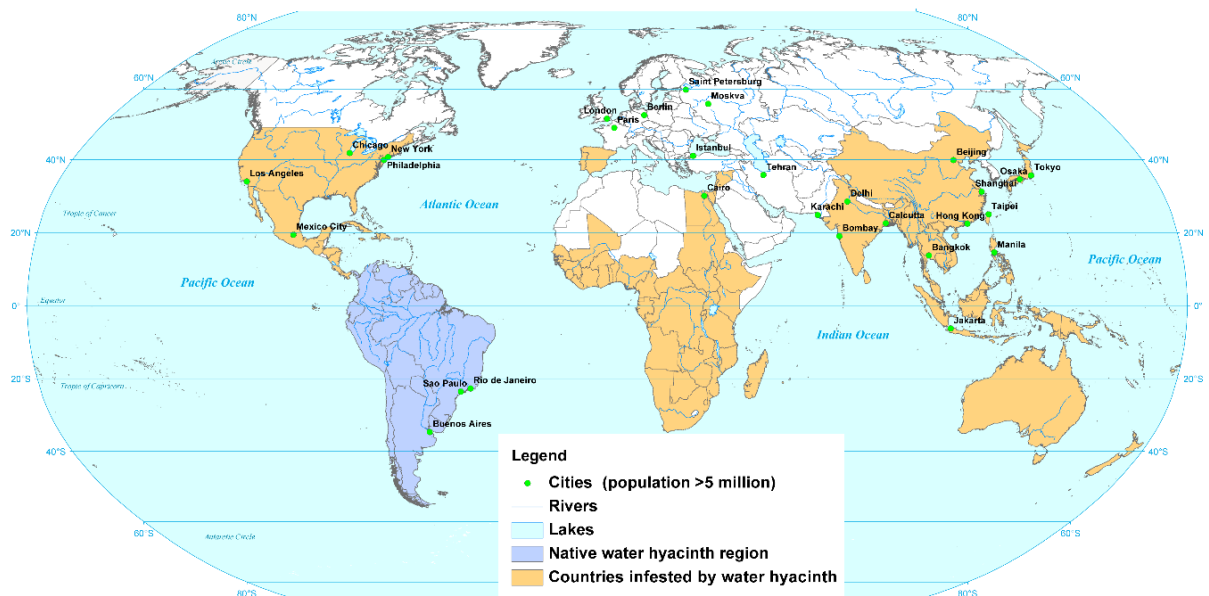


Figure I-1. Worldwide distribution of water hyacinth (Yan et al., 2017)

1.2 Impacts of water hyacinth

Water hyacinth disrupts biodiversity, hydrology, and water quality in freshwater ecosystems (Thamaga & Dube, 2018). It reduces water storage capacity and influences lake

hydrology through increased evapotranspiration (Sasaqi et al., 2019; Dersseh et al., 2019b). The plant also affects aquatic life, including phytoplankton, zooplankton, benthos, invertebrates, and vertebrates, primarily through environmental and trophic interactions (Yan et al., 2017). The spread of water hyacinth reduces phytoplankton and zooplankton productivity, lowers dissolved oxygen levels, decreases fish production, and blocks waterways. It clogs irrigation channels, impacts hydroelectric power generation, impairs fishing and transportation, hinders tourism, restricts swimming, and poses threats to human health (Churko et al., 2024; Villamagna & Murphy, 2010; Harun et al., 2021; Dersseh et al., 2019b; Dersseh et al., 2020; Damtie et al., 2022). However, in its native ecosystems, water hyacinth enhances habitat complexity, provides shelter and feeding grounds, and aids in water purification through pollutant absorption (Brendonck et al., 2003; Villamagna & Murphy, 2010). It also holds the potential for bioremediation by reducing nutrient and contaminant levels (Villamagna & Murphy, 2010). A comprehensive understanding of its spatiotemporal distribution and ecological impact is essential for developing balanced strategies that mitigate its harmful effects while recognizing its potential benefits in native ecosystems.

1.2.1. Impact of water hyacinth on water loss

Water hyacinth significantly reduces the water storage capacity of lakes due to its high evapotranspiration rates (Damtie et al., 2021; Dersseh, et al., 2019b). The plant absorbs water through its roots to support metabolic processes, with transpiration being a key mechanism. During transpiration, water is lost as vapor through stomata, cuticles, or lenticels, with approximately 90% of absorbed water released through stomata (Maylani et al., 2020). This process is influenced by internal factors such as leaf size, thickness, and the number and location of stomata, as well as external factors like light intensity, temperature, and humidity. In aquatic plants like water hyacinth, the high density of stomata on the upper leaf surface further accelerates evaporation (Maylani et al., 2020). Studies reported that water loss through evapotranspiration from water hyacinths can be 3.2 to 3.7 times greater than natural evaporation from open water surfaces (Damtie et al., 2021; Matthew Cock, 2001; Rashed,

2014; Van Der Weert & Kamerling, 1974). This increased water loss poses a significant threat by reducing the volume of water available for developmental projects, impacting water-dependent industries, and affecting irrigation-based agriculture (Arp et al., 2017). To address these challenges, further research is essential to fully understand and quantify the effects of water hyacinth on water volume loss, particularly in lakes where this invasive species is prevalent, such as Lake Tana.

1.2.2. Impact of water hyacinth on water quality parameters

Water hyacinth has a significant impact on water quality, primarily through the formation of dense mats that disrupt various aquatic processes (Villamagna & Murphy, 2010). The most common effects of these mats include reduced phytoplankton productivity and lower dissolved oxygen levels beneath them (Perna & Burrows, 2005). For example, Tobias et al. (2019) reported significantly reduced dissolved oxygen levels in areas with water hyacinth patches compared to open water areas in the San Francisco Estuary. These mats hinder oxygen transfer from the air to the water's surface and block light essential for photosynthesis in both phytoplankton and submerged vegetation (Villamagna & Murphy, 2010). Unlike phytoplankton and submerged vegetation, water hyacinth does not contribute oxygen to the water column (Meerhoff et al., 2003). Other impacts of this invasive plant include increased sedimentation rates due to its complex root system and the stabilization of pH levels and temperature (Villamagna & Murphy, 2010). It also contributes to elevated water temperature, turbidity, chemical oxygen demand (COD), and biological oxygen demand (BOD) (Kiyemba et al., 2023). Water hyacinth influences water temperature through two main mechanisms: (1) by reducing water movement, which can increase temperatures by extending the water's residence time, and (2) by shading the water surface, which can lower temperatures by blocking solar radiation temperatures (Tobias et al., 2019). Additionally, higher temperatures observed under water hyacinth mats may result from heat generated by the decomposition of organic matter beneath the mats (Gezie et al., 2018).

While water hyacinths are widely known for their detrimental impacts, they can also enhance water quality in certain contexts (Rodríguez et al., 2012). This invasive plant

effectively removes heavy metals from wastewater through root uptake and accumulation (Harun et al., 2021), achieving up to 99.5% removal of chromium from industrial mine wastewater (Saha et al., 2017) and other metals such as zinc, lead, iron, copper, and nickel from landfill leachates (Abbas et al., 2019). Additionally, water hyacinths remove ammonia and phosphorus (Nash et al., 2019), with phosphorus removal rates reaching up to 77.2% from rice mill wastewater (Kumar & Deswal, 2020). Yan et al. (2017) noted water hyacinth's effectiveness in treating eutrophic waters by removing phosphorus and nitrogen and enhancing denitrification, which can account for approximately 34.4% of total nitrogen removal, though this rate varies with nutrient levels and environmental conditions. Water hyacinths also help remove suspended solids near the water's surface, clarifying previously turbid water (Toft et al., 2003). In highly turbid conditions, the plant can act as a turbidity sink by slowing water flow and promoting sedimentation, which may reduce overall turbidity despite the addition of detritus (Zimmels et al., 2006). Minimum Chlorophyll-*a* (Chl-*a*) concentrations have also been reported at sites with water hyacinths compared to open waters (Dersseh et al., 2022). However, the impact of this invasive weed on physical and biological water quality parameters, such as water temperature, turbidity, and Chl-*a*, has not been thoroughly investigated in Lake Tana. A comprehensive understanding of these impacts will aid in developing targeted interventions to mitigate the negative effects while potentially leveraging any benefits they may offer.

1.3 Remote sensing of water hyacinth and its detection methods

Over the past 30 years, numerous satellite-borne sensors have been utilized to gather data on water hyacinths (Cavalli et al., 2009). A review of remote sensing publications indexed in the Scopus database reveals a notable increase in research focusing on the spatiotemporal distribution of this invasive species in lakes and rivers. From 1988 to 2023, the number of publications on remote sensing of water hyacinths increased significantly (Figure I-2). This trend highlights the growing application of remote sensing technologies for monitoring water hyacinths, driven by their ability to provide rapid, large-scale, and detailed assessments. Remote sensing is particularly valuable for tracking water hyacinth

invasions due to its capacity for timely, cost-effective, and broad-scale monitoring of aquatic weeds (Thamaga & Dube, 2018). Satellite data enable comprehensive analysis by capturing the spatiotemporal distribution of aquatic macrophytes (Dube et al., 2014; Shekede et al., 2008). Frequent overpasses and extensive spatial coverage provided by satellite sensors are essential for short- and long-term monitoring, facilitating the evaluation of invasive species management efforts (Penatti et al., 2015). As a result, satellite imagery has become a critical data source in ecological and environmental research (Aplin, 2005), offering high-quality information suited for mapping water hyacinth infestations and supporting effective management strategies. However, these methods can be limited by cloud cover and meteorological conditions, particularly during the rainy season (Thamaga & Dube, 2018).

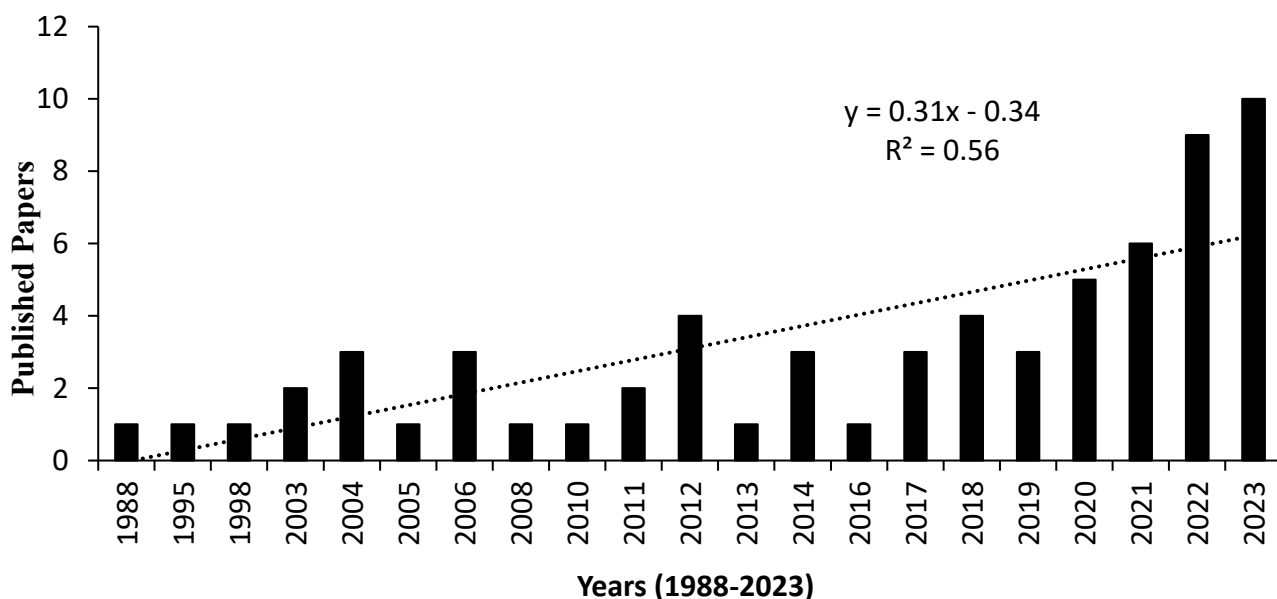


Figure I-2. Number of publications on remote sensing of water hyacinth in the Scopus database (1988–2023)

Various remote sensing technologies, including optical systems and Synthetic Aperture Radar (SAR), play a vital role in detecting, mapping, and monitoring water hyacinths in large water bodies (Datta et al., 2021). Notable open-access satellite sensors for monitoring water hyacinth include Sentinel-1 (SAR) (Belayhun & Mekuriaw, 2024), Sentinel-2 (optical), MERIS, Oceansat-2, Landsat-1-9, ASTER, ALOS, AVNIR-2, SPOT-5,

and NISAR (Datta et al., 2021). Optical images from sensors such as Landsat-8 and Sentinel-2 are particularly effective due to their broad spectral range, relatively high resolution, and open-access availability. These images are useful for distinguishing water hyacinth mats from algal blooms and other aquatic macrophytes, as submerged macrophytes exhibit lower reflectance in the near-infrared spectrum compared to water hyacinths. Although higher-resolution commercial satellite data, such as RapidEye, QuickBird, WorldView-2, and SkySat, offer significant benefits, few studies have utilized these datasets for water hyacinth monitoring due to their high cost (Thamaga & Dube, 2018). Nonetheless, Sentinel-2's enhanced spectral and spatial resolution (10 meters) has greatly improved the detection and estimation of water hyacinth spatial coverage and has been widely employed in recent studies (Damtie et al., 2021, 2022; Dersseh et al., 2020; Mucheye et al., 2022).

Accurately detecting water hyacinths in complex environments poses challenges due to their spectral similarity with other vegetation types and varying growth stages (Xie et al., 2008). Traditional per-pixel classifiers, such as the Maximum Likelihood Classifier (MLC), which rely on statistical patterns, often struggle with mixed pixels, reducing accuracy, especially in imagery with limited spectral, temporal, and spatial resolution (Thamaga & Dube, 2018). However, recent advancements in machine learning techniques, including Classification and Regression Trees (CART), Random Forest (RF), Support Vector Machines (SVM), and Artificial Neural Networks (ANN), have significantly improved detection accuracy in these challenging environments due to their ability to handle large datasets (Abdel-Rahman et al., 2014; Thamaga & Dube, 2018).

Various researchers have employed different classification methods for water hyacinth detection using satellite data (Table I-1). For instance, Shekede et al. (2008) and Djihouessi et al. (2021) utilized normalized difference vegetation index (NDVI) from Landsat-1 to Landsat-8 and Sentinel-2 images, respectively. More advanced techniques, such as RF and SVM, have been applied by Mukarugwiro et al. (2019) and Pádua et al. (2022) to enhance detection accuracy. Other methods include the use of Linear Discriminant Analysis (LDA) by Thamaga and Dube (2018) to map seasonal water hyacinth dynamics, achieving approximately 80% accuracy. Dube et al. (2018) employed discriminant analysis (DA) and

partial least squares discriminant analysis (PLS-DA) on Landsat 8 imagery, achieving 95% accuracy. Thamaga and Dube (2019) further applied LDA with Sentinel-2 data, achieving accuracy of 80.79% during the wet season and 79.04% during the dry season.

Machine learning methods for water hyacinth detection using satellite data have demonstrated their effectiveness in various studies (Agjee et al., 2015; Mukarugwiro et al., 2019; Pádua et al., 2022). Pádua et al. (2021) compared different machine learning algorithms and reported that RF achieved the highest accuracy (94%) compared to SVM, Gaussian Naive Bayes, k-nearest neighbors, and ANN using UAV and Sentinel-2 data. Mukarugwiro et al. (2019) also reported that RF (85%) outperformed SVM (65%) in detecting water hyacinths in Rwanda's water bodies. Additionally, Ade et al. (2022) achieved 90% overall accuracy using RF with Sentinel-2 data, while Singh et al. (2022) utilized a hierarchical classification approach, achieving 93% overall accuracy and an F1 score of 87%. These reports demonstrate the effectiveness of machine learning algorithms in detecting water hyacinths.

In previous studies of Lake Tana, various classification methods have been applied to different satellite data to detect and estimate the spatiotemporal variability of water hyacinths (Table I-1). For example, Asmare et al. (2020) applied Decision Tree and MLC to Landsat-8 data (2013–2017), while Worqlul et al. (2020) used MLC with PlanetScope imagery (2017–2018). Damtie et al. (2021) employed MLC with Sentinel-2 imagery (2019), and Dersseh et al. (2020) used RF with Sentinel-2 imagery (2015–2019). Abebe et al. (2023) manually digitized water hyacinth from Sentinel-2 imagery (2016–2018), and Mucheye et al. (2022) used Sentinel-2 NDVI with a 0.6 threshold to estimate biomass and spatial coverage. Despite the variety of methods and satellite data used, no comprehensive comparative analysis has evaluated the effectiveness of these classification techniques in Lake Tana. This highlights the need for further research to identify the most accurate detection methods and to estimate the spatiotemporal variability of water hyacinths.

Table I-1: Summary of remote sensing satellite and water hyacinth detection methods in prior studies

Remote sensing satellite	Water hyacinth detection method	Reference
Landsat-2 and Landsat-5	NDVI	Shekede et al., 2008
MODIS	NDVI	Kiage & Obuoyo, 2011
Landsat 5	NDVI	Dube et al., 2014
Landsat-5	NDVI	Robles et al., 2015
Landsat-7 and Landsat-8	Discriminant Analysis	Dube et al., 2017a
Landsat- 8	Partial Least Squares Discriminant Analysis and Discriminant Analysis	Dube et al., 2017b
Landsat-1- 8	Discriminant Analysis	Dube et al., 2018
Landsat-7, Landsat-8 and Sentinel-2	NDVI	Ongore, 2018
Sentinel-2	FVC	Ghoussein et al., 2019
Landsat-8	Random Forest and Support Vector Machine	Mukarugwiro et al., 2019
Sentinel-2	Linear Discriminant Analysis	Thamaga & Dube, 2019
Landsat-8	Decision Tree and Maximum Likelihood Classifier	Asmare et al., 2020
Sentinel-2 and WorldView-2	Maximum Likelihood Classifier	Baretheur, 2020
Sentinel-2	Random Forest	Dersseh et al., 2020
Landsat-8 and Sentinel-2	Random Forest	Singh et al., 2020
PlanetScope	Maximum Likelihood Classifier	Worqlul et al., 2020
Landsat-8	NDVI, EVI, SAVI, CI Green, ARVI, MSAVI, MSI and DVI	Al-lami et al., 2021
Sentinel-2	Maximum Likelihood Classifier	Damtie et al., 2021
Sentinel-2	NDVI	Djihouessi et al., 2021
Landsat-5 and Landsat-8	NDVI	Kleinschroth et al., 2021
Landsat-5,7 and Landsat-8	Random Forest	Mukarugwiro et al., 2021
Sentinel-2	Random Forest	Ade et al., 2022
Sentinel-2	NDVI	Gerardo & de Lima, 2022
Sentinel-2	NDVI	Mucheye et al., 2022
Sentinel-2	Random Forest, Support Vector Machine, Gaussian Naive Bayes, K-nearest Neighbors and Artificial Neural Network	Pádua et al., 2022
Landsat-7 and 8	NDVI	Yismaw et al., 2024
Landsat-8 and Sentinel-2	Classification and Regression Tree, Random Forest, Support Vector Machine, and NDVI	This study

Where FVC: Fractional Vegetation Cover; NDVI: Normalized Difference Vegetation Index; EVI: Enhanced Vegetation Index; SAVI: Soil-Adjusted Vegetation Index; CI green: Chlorophyll Index Green; ARVI: Atmospherically Resistant Vegetation Index; MSAVI:

Modified Soil-Adjusted Vegetation Index; MSI: Moisture Stress Index; and DVI: Difference Vegetation Index.

In this study, three widely used machine learning algorithms—CART, RF, and SVM—were evaluated on the Google Earth Engine (GEE) platform to detect water hyacinths in Lake Tana using freely available Landsat-8 and Sentinel-2 imagery. These GEE-available algorithms were selected for their ability to handle outliers and provide reliable classification in complex environments. GEE, an innovative platform for geospatial big data analysis (Zhao et al., 2024), is an ideal tool for integrating machine learning models with satellite data to monitor water hyacinth dynamics and support environmental management decisions. The spatiotemporal variability of water hyacinths in the lake was then determined using the method that achieved the highest accuracy.

1.4 Spatial and temporal distribution of water hyacinth

Understanding the spatiotemporal distribution of water hyacinths is crucial, as their rapid growth forms dense mats that impair biodiversity, reduce water storage capacity, degrade water quality, and affect livelihoods (Villamagna & Murphy, 2010). Since 2011, Lake Tana, Ethiopia's largest freshwater body, has been severely infested by this weed, which has spread rapidly due to favorable environmental conditions (Cai et al., 2023; Dersseh et al., 2020). Accurate tracking of its spread and dynamics is essential for effective management (Abebe et al., 2023). Reliable and timely information on the spatiotemporal distribution and extent of water hyacinth is necessary to understand its expansion, growth, and the vulnerable areas of the lake (Abebe et al., 2023; Thamaga & Dube, 2018). Temporal patterns, such as seasonal growth spurts, highlight critical periods for intervention. For instance, the weed often proliferates after the rainy season, driven by nutrient runoff from agriculture (Cai et al., 2023). Understanding these patterns enables policymakers to develop targeted strategies to control its spread. A detailed understanding of the rate and direction of water hyacinth spread, as well as its impacts, is essential (Thamaga & Dube, 2018). Single-date assessments cannot provide a complete understanding of the spatiotemporal variability of water hyacinths (Abebe et al., 2023). Comprehensive data on the spatial and temporal

distribution, including seasonal variability, is crucial for effective water resource management (Molinos et al., 2015). Continuous monitoring of aquatic weed proliferation is crucial for proper management, the development of effective control strategies, and the prioritization of the most infested areas (Abebe et al., 2023; Albright et al., 2004). Previous studies on Lake Tana's water hyacinth infestation have primarily relied on single-time assessments. However, Dersseh et al. (2020) and Abebe et al. (2023) attempted to analyze its spatiotemporal dynamics from 2015 to 2019 using only Sentinel-2 spectral bands. Long-term spatiotemporal studies that account for monthly and seasonal variability, as well as the weed's impact on water loss in the lake using spectral bands and indices, have not been thoroughly investigated. Additionally, conflicting reports on the extent of weed coverage have caused disagreements among stakeholders (Dersseh et al., 2020). Therefore, further research is needed to resolve these discrepancies and provide a more comprehensive understanding of the annual and seasonal dynamics of water hyacinth and its impact on water loss in Lake Tana.

1.5. Water quality parameters

Monitoring water quality is crucial for both ecological health and human well-being (Vasistha & Ganguly, 2020). Water temperature, turbidity, and chlorophyll-*a* (Chl-*a*) are essential parameters for assessing water quality and the overall health of lake ecosystems.

Water Temperature: Lake water temperature is an important indicator that explains the lake's physical properties, chemical processes, biodiversity, and hydrodynamic phenomena (Yu et al., 2020). It influences lake stratification, affecting species distribution and aquatic plant and animal communities (Sima et al., 2013; Yu et al., 2020). Temperature also affects the solubility and availability of chemical constituents in water, notably dissolved oxygen, which decreases as temperature rises. Additionally, water temperature impacts the distribution and interaction of contaminants such as nutrients (Gholizadeh et al., 2016). Lake surface water temperature (LSWT), measured within the top one meter, is vital for ecosystem research (Sharma et al., 2015), as most interactions between lakes and their environment occur at the air-water interface (Rouse et al., 2005). LSWT influences various physical,

chemical, and biological processes in aquatic environments (Aguilar-Lome et al., 2021; Crosman & Horel, 2009; Reinart & Reinhold, 2008; Trumpickas et al., 2009; Xiao et al., 2013) and is a key indicator of ecological health (Yang et al., 2022; Yang et al., 2018). Spatiotemporal analysis of LSWT is crucial for managing lake environments and regional ecological conditions (Yu et al., 2020)

While various satellite data sources, including the Advanced Very High-Resolution Radiometer (AVHRR) (Chavula et al., 2009), Landsat (Wloczyk et al., 2006; Mushtaq et al., 2021), and the Moderate Resolution Imaging Spectroradiometer (MODIS) (Xiao et al., 2013), have been used to derive LSWT, MODIS remains the most suitable choice for large lakes. This is due to its high temporal resolution, moderate spatial resolution, extensive spectral range, extended temporal coverage, and high accuracy (Reinart & Reinhold, 2008; Crosman & Horel, 2009; Schneider et al., 2009; Xiao et al., 2013; Xie et al., 2022), with a mean LSWT error within ± 0.6 Kelvin across 10 validation datasets (Wan, 2014). For example, Tavares et al. (2019) evaluated MODIS LSWT and Landsat 7-derived LSWT using *in-situ* measurements and reported that MODIS LSWT (RMSE: 1.05 °C) outperformed Landsat 7-derived LSWT (RMSE: 1.07 °C), suggesting MODIS for general LSWT studies and Landsat-derived LSWT for small lakes. In cloud-prone places like the Ethiopian Highlands, MODIS's high temporal resolution provides an advantage by increasing the possibility of obtaining cloud-free data. MODIS LSWT is thus the most reliable method for long-term LSWT monitoring, offering valuable insights into lake thermal structure and regional air temperature changes (Tavares et al., 2019).

Turbidity: Turbidity measures the reduction in optical transparency of water due to suspended materials blocking light transmission (Matos et al., 2024). It serves as an indicator of sedimentation processes (Kayalik & Çorumluoğlu, 2022). Sources of turbidity include natural processes like erosion and sedimentation, as well as human activities such as urban runoff, industrial discharges, pesticides, and microplastics (De Carlo et al., 2004; Li et al., 2019; Scheffer, 1999). High turbidity affects light penetration, which is critical for photosynthetic organisms. Elevated turbidity can impair photosynthesis, disrupt aquatic ecosystems, and signal the presence of other contaminants affecting water quality (Bessell-

Browne et al., 2017; Wang & Seyed-Yagoobi, 1994; De Roos et al., 2017; Jung et al., 2014). It can also reduce filtration efficiency and damage infrastructure by clogging and eroding pipes, pumps, and valves. Regulations often set maximum turbidity levels for drinking water; the World Health Organization recommends keeping turbidity below 1 NTU before disinfection and up to 5 NTU in resource-limited areas (Matos et al., 2024). Therefore, understanding the spatiotemporal distribution of turbidity is fundamental for effective water resource management.

Satellite-based remote sensing enables the measurement of solar radiation reflected by surface waters across various wavelengths, which are correlated with different water quality parameters (Hossain et al., 2010). This approach offers three key advantages over traditional ground sampling methods: 1) near-continuous spatial coverage for large-scale assessments, 2) the ability to monitor remote and inaccessible regions, and 3) access to historical data through archived imagery, enabling evaluation of past water quality (Gholizadeh et al., 2016). Despite its lower spatial resolution compared to *in-situ* measurements, remote sensing provides valuable spatial and temporal datasets for understanding water quality trends on a broader scale. Numerous studies have employed remote sensing imagery, including MODIS, Landsat-5, Landsat-8, and Sentinel-2 images, for turbidity estimation (Dewantoro et al., 2024; Hossain et al., 2021; Lobo et al., 2015; Ouma et al., 2020; Worqlul et al., 2020). With its relatively higher spatial resolution, Sentinel-2's Multi-Spectral Instrument (MSI) enhances turbidity estimation accuracy (Lacaux et al., 2007). Remote sensing technology has been applied using various algorithms, including single-band approaches focusing on the red or near-infrared bands (Nechad et al., 2010; Dogliotti et al., 2015) and band combinations such as red–near-infrared or red–green, including the Normalized Difference Turbidity Index (NDTI) (Garg et al., 2020; Toming et al., 2016; Lacaux et al., 2007). Researchers suggest that band combinations generally yield more accurate estimations than single-band methods (Sebastiá-Frasquet et al., 2019; Garg et al., 2020). While pure water reflects more in the green than in the red wavelength region, higher turbidity increases reflectance in the red region (Garg et al., 2020).

Chlorophyll-*a* (Chl-*a*): Chl-*a* is a vital pigment for photosynthesis and a key indicator of lake eutrophication and phytoplankton biomass. It provides insights into biochemical processes in lakes, aiding in the assessment of water quality and ecosystem health (Hossain et al., 2021; Wu et al., 2022; Zhao et al., 2024). It links nutrient enrichment, particularly phosphorus, with increased phytoplankton productivity (de Raús Maúre et al., 2021). Elevated Chl-*a* levels often signal algal blooms driven by eutrophication, which disrupt ecological balance and pose risks to drinking water quality (Gholizadeh et al., 2016). Increased Chl-*a* concentrations are associated with several ecological and public health risks. Studies have identified thresholds for Chl-*a* that correspond to varying levels of water quality degradation and health concerns. For instance, Heath et al. (1998) reported that Chl-*a* concentrations exceeding 30 µg/L substantially increase the risk of algal-related health problems. Similarly, Carney (1998) noted that taste and odor issues can emerge at 9-10 µg/L concentrations, with more severe impairments occurring at 15-20 µg/L and higher levels. Furthermore, Chorus and Bartram (1999) reported that while a Chl-*a* concentration of 10 µg/L presents a low probability of health risks, levels around 50 µg/L pose moderate risks, particularly when cyanobacteria are involved. To manage these concerns, Smith et al. (2002) recommended maintaining Chl-*a* levels below 15 µg/L to avoid taste and odor issues linked to geosmin.

Estimating Chl-*a* concentrations in turbid and optically complex inland waters is particularly challenging due to the influence of suspended sediments and yellow substances in addition to phytoplankton (Wang & Chen, 2024). Cloud cover poses a significant challenge in obtaining accurate remote sensing data for mapping water quality parameters, further complicating the estimation process. Despite these challenges, remote sensing has proven invaluable for monitoring Chl-*a* concentrations across diverse aquatic environments, including lakes and rivers (Shi et al., 2015). Several satellite-based sensors have contributed significantly to this effort, including the Medium Resolution Imaging Spectrometer (MERIS) on the European Space Agency's ENVISAT satellite, which provided long-term data on lake water quality from 2002 to 2012 (Odermatt et al., 2018). Its successor, the Ocean and Land Colour Instrument (OLCI) on Sentinel-3 satellites, launched under the European Copernicus

program, continues this legacy, with data available from 2016 onward (Pahlevan et al., 2022). The Operational Land Imager (OLI) on the Landsat-8 satellite has provided high spatial resolution monitoring of lake water quality since 2013 (Andrzej Urbanski et al., 2016). Additionally, the Multi-Spectral Instrument (MSI) aboard Sentinel-2, operational since 2015, offers high spatial and temporal resolution imagery, enhancing water quality monitoring efforts (Pahlevan et al., 2020). Sentinel-2 provides high temporal, spatial, and spectral resolution, making it an essential tool for monitoring inland lake water quality, including Chl-*a* concentrations (Wang & Chen, 2024). While sensors like MODIS offer long-term temporal data (Lei et al., 2020), their coarser spatial resolution makes them less suitable for Chl-*a* estimation in inland lakes. Higher-resolution satellite data, such as Sentinel-2, is essential for accurate Chl-*a* estimation. Understanding the spatiotemporal distribution of Chl-*a* concentrations is essential for protecting ecological health and assessing water quality.

1.6. Goal and objectives of the research

This doctoral research aimed to analyze the spatiotemporal distribution of water hyacinth and its impact on hydrology and water quality using remote sensing technology. The study objectives were:

1. To compare the performance of different non-parametric machine-learning algorithms for water hyacinth detection (*Chapter II*): The research evaluated CART, RF, and SVM algorithms to identify the most accurate method for detecting water hyacinths.
2. To analyze the spatiotemporal dynamics of water hyacinth and associated water loss due to evapotranspiration (*Chapter III*): The study assessed the spatial and temporal expansion of water hyacinths, identified key environmental factors driving their growth, and quantified water loss through evapotranspiration.
3. To examine the spatiotemporal distribution of physical and biological water quality parameters and their interrelationship with water hyacinth biomass (*Chapter IV*): The research investigated spatial and temporal variations in water quality parameters, such as LSWT, turbidity, and Chl-*a*, and their relationships with water hyacinth biomass.

CHAPTER TWO

2. DETECTION OF WATER HYACINTH (*Eichhornia crassipes*) IN LAKE TANA, ETHIOPIA, USING MACHINE LEARNING ALGORITHMS

2.1. INTRODUCTION

Lake Tana, the largest highland lake in Ethiopia, holds ecological, religious, historical, and economic significance (Worqlul et al., 2020). It accounts for approximately 33% of the total volume of inland water resources and 52% of the total water surface area in the country (Goshu et al., 2010). However, the lake is currently infested with the rapidly reproducing herbaceous water hyacinth (*Eichhornia crassipes*), recognized as one of the world's most invasive weeds (Karim et al., 2011; Thamaga & Dube, 2018). This invasive aquatic plant poses significant ecological, economic, and social impacts (Datta et al., 2021). Detecting and mapping water hyacinths using the most accurate machine learning algorithms on satellite data is crucial for decision-makers, as it provides accurate and up-to-date information on weed infestations, supporting the development of effective aquatic weed management and control strategies.

Remote sensing images are widely used to determine the spatial and temporal distribution of ground objects (Hoshino et al., 2012; Mucheye et al., 2022; Ritchie et al., 2003). Satellite data provides a cost-effective and efficient solution for monitoring the spatial and temporal distribution of water hyacinth infestations at large scales and short intervals (Datta et al., 2021). Machine learning algorithms are increasingly applied in classifying and detecting ground objects from satellite images due to their superior efficiency and accuracy compared to traditional parametric algorithms, such as maximum likelihood classifiers (MLCs) (Gibson et al., 2020; Liu et al., 2022; Pham et al., 2020; Sheykhmousa et al., 2020; Sun et al., 2019). When detecting water hyacinth distribution, machine learning algorithms offer significant improvements in detection accuracy, enabling better cleanup efforts and hotspot forecasting (Datta et al., 2021). Among the machine learning algorithms, classification and regression tree (CART), random forest (RF), and support vector machine

(SVM) algorithms are widely used for remote sensing image analysis due to their classification accuracy (Loukika et al., 2021). RF and SVM algorithms are known for their robustness and accuracy in image classification tasks, and the ability to handle high-dimensional data (Cortes & Vapnik, 1995; Belgiu & Drăgu, 2016); the CART algorithm is known for its interpretability and simplicity (Brieman et al., 1984). Deep learning techniques, such as convolutional neural networks (CNNs), also show promising results for image classification tasks but are computationally intensive and require extensive ground truth training data (Sewak et al., 2018). Due to variations in the texture and spectral reflectance of ground features, machine learning algorithms produce variable results for pattern recognition tasks in satellite data (Liu et al., 2022). Furthermore, the relative performance of algorithms can vary by season due to changes in the physiological characteristics of plants and the influence of their life cycles on spectral reflectance. Although machine learning algorithms are widely applied across interdisciplinary fields, there is a notable lack of comparative studies specifically evaluating their performance for water hyacinth detection in Lake Tana.

Previous studies utilized different classifiers, such as the maximum likelihood classifier (MLC) (Asmare et al., 2020; Damtie et al., 2021, 2022; Worqlul et al., 2020), decision tree (Asmare et al., 2020), and random forest (RF) (Dersseh et al., 2020a), to assess the spatial and temporal distribution of water hyacinths in Lake Tana. However, these studies did not focus on identifying optimal detection methods. Most studies on Lake Tana have focused exclusively on the northeastern part, utilizing Level 1 top-of-atmosphere (TOA) satellite imagery without applying atmospheric corrections and relying solely on spectral bands for water hyacinth detection. For example, Dersseh et al. (2020) employed the RF method with Sentinel-2 MSI Level-1C TOA data to detect water hyacinth and estimate its areal coverage but restricted the analysis to the shoreline boundary and used only spectral bands without atmospheric corrections. Similarly, Worqlul et al. (2020) applied the MLC method to PlanetScope Level 1 TOA products, also without atmospheric corrections. Atmospheric corrections, however, are critical for accurately estimating the spatial coverage and spatiotemporal patterns of aquatic plants in lake environments (Mucheye et al., 2022; Pahlevan et al., 2021). Additionally, Asmare et al. (2020) used a decision tree algorithm to

detect water hyacinth in Landsat-8 images but did not evaluate the classifier's accuracy, even though accuracy is essential for assessing classifier performance. To our knowledge, no comparative studies have evaluated the effectiveness of different common machine-learning algorithms for water hyacinth detection across seasons in Lake Tana. Given the unique characteristics of the lake and the species, certain algorithms may perform better under different conditions.

The spectral reflectance of water hyacinth varies with age and season, highlighting the need to identify the most suitable machine learning algorithm for detection across different seasons. Non-parametric machine learning methods, such as random forest (RF), classification and regression trees (CART), and support vector machines (SVM), are well-suited for handling outliers in training data (Breiman, 2001) and often excel in analyzing complex and non-linear datasets. This study aimed to compare the performance of three non-parametric machine learning algorithms —CART, RF, and SVM— for detecting water hyacinths and to quantify their accuracy using atmospherically corrected Sentinel-2 and Landsat-8 imagery. The analysis integrated spectral bands and indices within the Google Earth Engine (GEE) platform across different seasons. By identifying the most accurate method for water hyacinth detection and spatial distribution estimation, this study provides critical insights to support the development of efficient and targeted management strategies, contributing to the sustainable conservation of Lake Tana.

2.2. MATERIALS AND METHODS

2.2.1. Description of the Study Area

Lake Tana, a shallow freshwater lake in the northwestern region of Ethiopia, extends from 10°45'54.1" N to 12°50'15.9" N latitude and 36°10'24.9" E to 38°50'54.48" E longitude (Figure II-1). Situated at an elevation of approximately 1,786 meters above sea level, Lake Tana spans a surface area ranging from 2,989 km² to 3,064 km². It is the source of the Blue Nile River (McCartney et al., 2010) and serves as a crucial natural reservoir for hydroelectric power generation. Currently, most of the water that once flowed through the Blue Nile is diverted to the Beles basin to generate 460 megawatts (MW) of electricity (Alemu et al.,

2020). Lake Tana is fed by over 40 rivers and streams, with the Gilgel Abay, Ribb, Gumara, and Megech Rivers contributing 95% of its water (Setegn et al., 2009). Gilgel Abay, entering from the south, is the largest contributor, draining 35% of the Lake Tana basin. Gumara and Ribb each drain 27% of the basin and flow into the lake from the east, while the Megech River, with a drainage area covering 11% of the basin, enters from the north (Alemu et al., 2020). The lake's annual inflow averages around 4,986 cubic megameters, while its outflow is approximately 3,753 cubic megameters per year (McCartney et al., 2010).

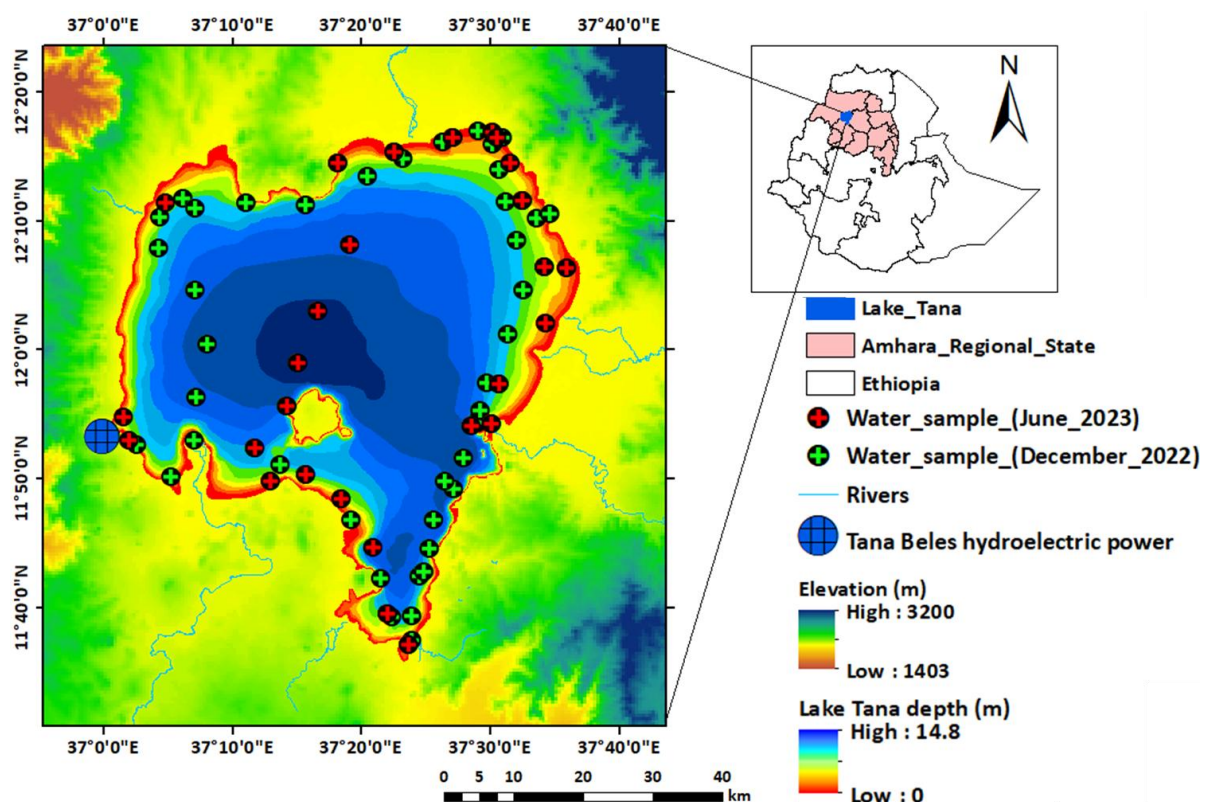


Figure II-1. Map of Lake Tana including land elevation, depth, and *in-situ* sampling locations

The regional climate is characterized by four distinct seasons: *Bega* (dry season, December to February), *Belg* (pre-rainy season, March to May), *Kiremit* (rainy season, June to August), and *Tsedey* (post-rainy season, September to November) (Alemu & Bawoke, 2020; Birara et al., 2018). The highest precipitation occurs in July and August, with mean monthly rainfall ranging from 388 mm to 427 mm and an annual mean rainfall of

approximately 1,531 mm (Figure II-2). Air temperature exhibits high daily variability but relatively low seasonal variability, with daytime maximums ranging from 19°C to 31°C and nighttime minimums ranging from 13°C to 20°C (Cai et al., 2023). The mean monthly air temperature is highest from March to May and lowest from July to September (Figure II-2). Similarly, lake water evaporation peaks between March and May and reaches its minimum from June to September (Figure II-3). Water evaporation from the lake decreased significantly from 2015 to 2023 at a rate of 0.069 mm/month (Figure II-3). This study was conducted within and around the shoreline of Lake Tana, with a 2 km buffer zone extending outward from the shoreline.

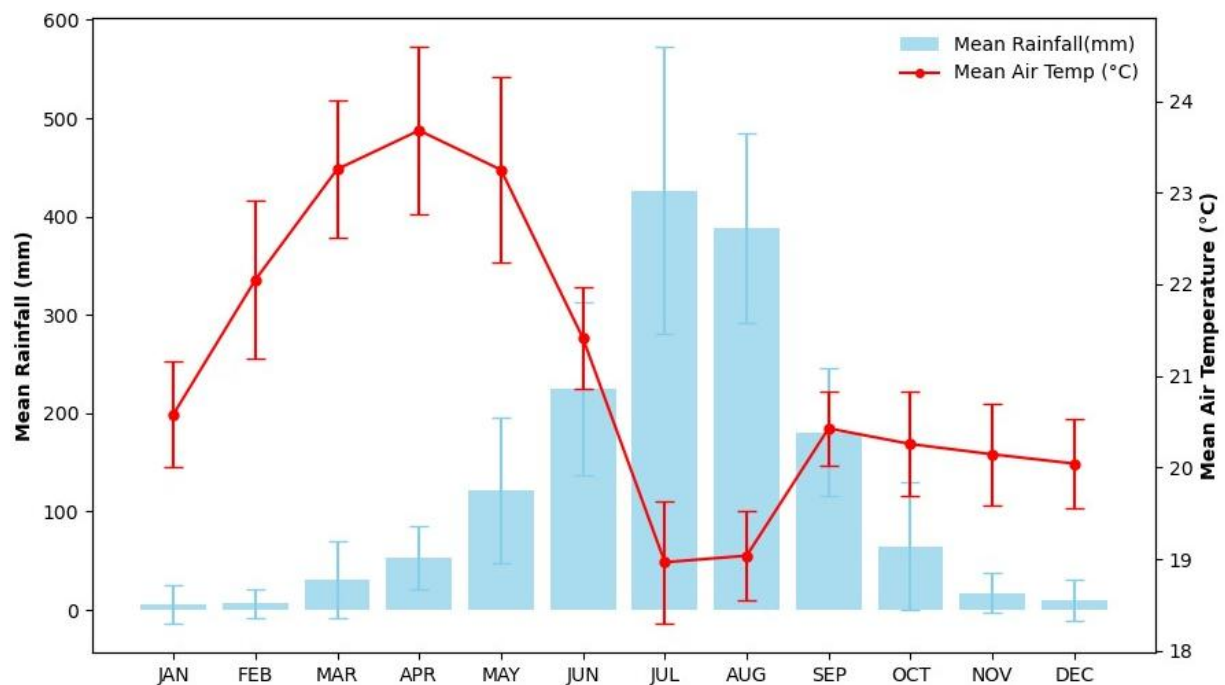


Figure II-2. Mean monthly rainfall (blue) and air temperature (orange) in the Lake Tana region (1981–2022), including standard deviation for both variables. Data were sourced from the NASA/POWER website: <https://power.larc.nasa.gov/>

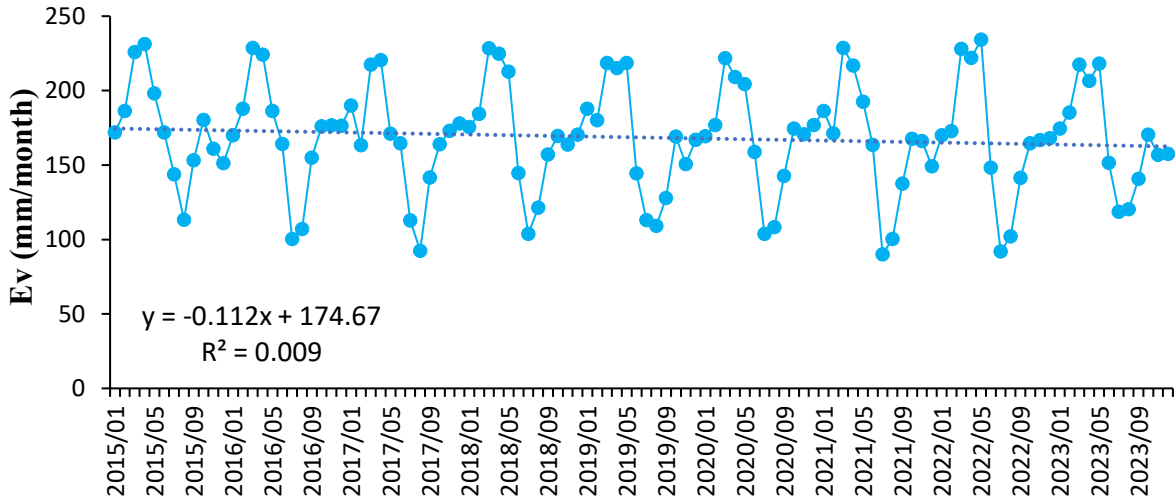


Figure II-3. Water evaporation (Ev) of Lake Tana, derived from MODIS data, covering the period from January 2015 to December 2023

2.2.2. Data types and processing

In this study, atmospherically corrected Level 2A Sentinel-2 multispectral instrument (MSI) and Level 2 Landsat-8 operational land imager (OLI) Tier 1 surface reflectance data were utilized. A cloud mask algorithm available on the Google Earth Engine (GEE) platform was applied to remove unclear pixels caused by cloud contamination across all images. Median temporal composite methods were used to fill gaps in cloudy images. Monthly median composites of Landsat-8 and Sentinel-2 images from October 2021, January 2022, March 2022, and June 2022 were selected to represent the post-rainy, dry, pre-rainy, and rainy seasons, respectively. Images with less than 5% cloud cover were used for the post-rainy, dry, and pre-rainy seasons. However, due to high cloud contamination during the rainy season, images with less than 10% cloud cover, acquired in June 2022, were used to represent this season. The study utilized Landsat-8 data bands two through seven (B2–B7) at a 30 m resolution, as well as Sentinel-2 data comprising four bands at a 10 m resolution and six bands at a 20 m resolution (Table II-1). Sentinel-2 bands with a 10 m resolution were downsampled to 20 m using a resampling technique to balance spatial resolution and computational efficiency, thereby improving overall detection accuracy.

Table II-1. Landsat-8 (OLI) Level 2 Tier 1 and Sentinel-2 (MSI) Level 2A surface reflectance bands used in the study

Sentinel-2			Landsat-8		
Band	Resolution (m)	Wavelength (nm)	Band	Resolution (m)	Wavelength (μm)
B2 (Blue)	10	496.6	B2 (Blue)	30	0.45–0.51
B3 (Green)	10	560	B3 (Green)	30	0.53–0.59
B4 (Red)	10	664.5	B4 (Red)	30	0.64–0.67
B5 (Red edge 1)	20	703.9	B5 (Near-infrared)	30	0.85–0.88
B6 (Red edge 2)	20	740.2	B6 (Shortwave infrared 1)	30	1.57–1.65
B7 (Red edge 3)	20	782.5	B7 (Shortwave infrared 2)	30	2.11–2.29
B8 (Near-infrared)	10	835.1			
B8A (Red edge 4)	20	864.8			
B11 (Shortwave infrared 1)	20	1613.7			
B12 (Shortwave infrared 2)	20	2202.4			

In addition to the raw spectral bands presented in Table II-1, the classifiers were provided with four derived environmental indices related to water and vegetation. Initially, nine spectral indices were generated: the normalized difference vegetation index (NDVI), enhanced vegetation index (EVI), chlorophyll index green (CLG), normalized difference water index (NDWI), simple ratio index (SRI), modified normalized difference water index (MNDWI), green normalized difference vegetation index (GNDVI), optimized soil-adjusted vegetation index (OSAVI), and difference vegetation index (DVI). To reduce data redundancy and identify less correlated indices, a pairwise correlation analysis between the bands and indices was performed using the *ee.Reducer.pearsonsCorrelation()* function in the Google Earth Engine (GEE). Five indices—GNDVI, OSAVI, DVI, EVI, and CLG—were found to be highly correlated and were excluded. The remaining four indices—NDVI, SRI, NDWI, and MNDWI (Table II-2)—were less correlated and were used as inputs for the classifiers, along with the spectral bands, to improve water hyacinth detection accuracy.

Table I-2. Equations and sources of spectral indices used in this study

Index	Equation	Source
NDVI	$(\text{NIR} - \text{Red})/(\text{NIR} + \text{Red})$	(Tucker, 1979)
NDWI	$(\text{Green} - \text{NIR})/(\text{Green} + \text{NIR})$	(McFeeters, 1996)
SRI	NIR/Red	(Jordan, 1969)
MNDWI	$(\text{Green} - \text{SWIR})/(\text{Green} + \text{SWIR})$	(Xu, 2006)

2.2.3. Sample point generation and water hyacinth detection methods

Based on field surveys, literature, and Google Earth images, Landsat-8 and Sentinel-2 images were classified into four land-use/land-cover (LULC) classes: water (clear and turbid), water hyacinth, other vegetation, and bare land. The other vegetation class included various vegetation types such as crops, wetlands, grazing lands, and forests, while the bare land class encompassed sediment deposition areas, cultivated land without crops, buildings, and rock outcrops. Field visits, GPS data, and the visual interpretation of Landsat-8 and Sentinel-2 images, supported by high-resolution Google Earth images, expert opinions, field background knowledge, and reports from the Lake Tana Protection and Development Agency (LTPDA), were used to manually digitize and delineate these classes. A handheld GPS device (GARMIN-72) was used to collect field data on water hyacinth patches in March 2022 within Lake Tana. Additionally, visual interpretation of multi-temporal images and Google Earth high-resolution imagery were employed to collect sample points. The process involved: (1) selecting sample points from Landsat-8 and Sentinel-2 images with the help of field knowledge, previous studies, and LTPDA reports, and (2) exporting these points to Keyhole Markup Language (KML) format for validation and reliability checks in Google Earth Pro using high-resolution imagery.

Irregular polygons for the four LULC classes were delineated in the March 2022 image using GPS points and sample points collected through visual interpretation of Landsat-8 and Sentinel-2 imagery. Similarly, irregular polygons for the four LULC classes were

delineated in October 2021, January 2022, and June 2022 based on sample points obtained through visual interpretation of the respective images. After delineating these polygons, stratified random sampling was carried out within each polygon. The polygons were evenly distributed across the study area to define strata effectively. Image classification accuracy depends on the number and distribution of training samples. To address the limitations caused by missing or unbalanced training samples, a stratified sampling method was employed using the GEE platform. This approach ensured an equal number of samples were extracted from each class, avoiding issues of over- or under-fitting (Zeng et al., 2020). According to the rule of thumb, each class requires at least 50 training samples for classification (Thomas et al., 2004). The stratified sampling method facilitated the generation of samples from all available classes, resulting in 1,200 labeled samples (300 per class). Of these, 70% were used for training and the remaining 30% for validation.

Three non-parametric machine learning methods available on the GEE platform were employed and selected for their robust ability to handle outliers in training data. A detailed explanation of each classifier and the associated processes is provided below:

Classification and regression tree (CART): The CART technique efficiently handles large datasets compared to traditional methods like the maximum likelihood classifier (MLC) (Zhao et al., 2024). CART is a binary decision classification tree (Breiman et al., 1984) that employs logical if-then scenarios to recursively partition the feature space into smaller regions, or nodes, based on the values of one or more input features. This is achieved by selecting the feature and threshold value that produces the most "pure" child nodes (Shetty, 2019). CART is straightforward to interpret but is influenced by sample size per class. Additionally, it may result in complex tree architectures when dealing with high-dimensional data (Loukika et al., 2021). CART can be prone to overfitting, particularly with deep and complex trees. To mitigate this, pruning techniques—such as setting a minimum number of observations per leaf—can be applied. In this study, hyperparameter tuning for maximum nodes and minimum leaf population was conducted to optimize classification accuracy. The *ee.Classifier.smileCart()* function in the GEE JavaScript API was used to create and train the CART classifier with specified training data, feature bands, and indices. The trained classifier

was then applied to the target imagery using the *classify ()* function, assigning each pixel to one of the predefined classes.

Random forest (RF): Introduced by Breiman (2001), RF is an ensemble learning method that uses multiple CART trees to make predictions. It creates multiple trees by selecting random subsets of the data and combining their predictions for increased accuracy and stability. Due to the randomness in sample and feature selection, RF offers strong noise resistance, high generalization ability, and effective processing of high-dimensional data without manual feature selection (Belgiu & Drăgu, 2016). Hyperparameter tuning for the bag fraction and the number of trees was performed to achieve optimal classification accuracy. The *ee.Classifier.smileRandomForest()* function in the GEE JavaScript API was used to train the RF classifier with the training data and selected features. The *classify ()* function was subsequently employed to classify the target imagery.

Support vector machine (SVM): SVM is a supervised classification algorithm that formulates a classification function based on an optimal hyperplane to separate classes (Kamal et al., 2020; Cortes & Vapnik, 1995). It determines the locality of decision boundaries between classes by maximizing the margin between the hyperplane and the nearest data points, known as support vectors (Huang et al., 2002; Oommen et al., 2008). SVM uses the principle of structural risk minimization (SRM) to ensure the hyperplane best separates the data points. It supports various kernels—linear, polynomial, and radial basis functions (RBF)—to model different data types. Important parameters influencing SVM performance include the cost parameter (C), gamma, and kernel functions. For large datasets, the linear kernel is computationally efficient and can handle high-dimensional data (Hsu et al., 2008). This study used the linear kernel SVM method for water hyacinth detection. A grid search technique was employed to set the best cost parameter (C) and select a linear kernel. The *ee.Classifier.libsvm()* function, a wrapper for the LIBSVM library, was used to create the SVM classifier. The *ee.Classifier.svm()* function was applied to train the classifier, and the *classify()* function was used to classify the target imagery.

2.2.4. Accuracy assessment

This study employed an independent validation sample set to evaluate the accuracy of classified images, ensuring reliability and consistency in the assessment process. The classified images produced using CART, RF, and SVM algorithms on Landsat-8 and Sentinel-2 images were validated using a confusion matrix in the GEE environment. The performance of the machine learning classifiers was evaluated using commonly adopted metrics: overall accuracy (OA; Eq. 1) and the *Kappa* coefficient (K; Eq. 2) (Loukika et al., 2021).

$$OA = \frac{\text{Number of Correctly Classified Samples}}{\text{Number of Total Samples}} \times 100 \quad \text{Eq. 1}$$

Overall accuracy (OA) measures the proportion of correctly classified samples relative to the total number of reference samples, providing an overall percentage of classification accuracy (Congalton, 1991).

$$K = \frac{N \sum_{i=1}^r X_{ii} - \sum_{i=1}^r (X_{i\cdot} \times X_{\cdot i})}{N^2 - \sum_{i=1}^r (X_{i\cdot} \times X_{\cdot i})} \quad \text{Eq. 2}$$

In Eq.2, r represents the number of rows and columns in the confusion matrix, X_{ii} is the number of observations in row i and column i , $X_{i\cdot}$ is the marginal total of row i , $X_{\cdot i}$ is the marginal total for column i , and N is the total number of samples. The *Kappa coefficient* accounts for the degree of agreement between predicted and actual classifications beyond random chance.

Furthermore, user accuracy (UA) (Eq. 3), which is equivalent to precision, and producer accuracy (PA) (Eq. 4), which corresponds to recall, were both used to evaluate classification performance at the class level (Nasiri et al., 2022). UA measures the proportion of correctly classified samples for each class relative to the total number of samples assigned to that class, while PA measures the proportion of correctly classified samples relative to the total number of reference samples for that class. Additionally, the F1 score (Eq. 5), which is the harmonic mean of UA and PA, balances the trade-off between precision and recall and provides a single metric for assessing classification performance (Hurskainen et al., 2019).

The F1 score is widely regarded as an optimal performance metric because it equally emphasizes both UA and PA (Elmahdy et al., 2020; Nasiri et al., 2022).

$$\begin{aligned} \text{UA} &= \frac{\text{Number of Correctly Classified Samples in each class}}{\text{Number of Samples Classified to that class}} = \text{Precision} \\ &= \frac{\text{True positive (TP)}}{\text{True positive (TP) + False positive (FP)}} \end{aligned} \quad \text{Eq. 3}$$

$$\begin{aligned} \text{PA} &= \frac{\text{Number of Correctly Classified Samples in each class}}{\text{Number of Samples from Reference Data in each Class}} = \text{Recall} \\ &= \frac{\text{True positive (TP)}}{\text{True positive (TP) + False negative (FN)}} \end{aligned} \quad \text{Eq. 4}$$

$$\text{F1 score} = \frac{2 \times \text{Precision} \times \text{Recall}}{\text{Precision} + \text{Recall}} \quad \text{Eq.5}$$

Spectral reflectance curves from Sentinel-2 images were analyzed to identify the most effective bands for distinguishing water hyacinths from other land use/land cover (LULC) types. The RF classifier's feature importance was further evaluated using the *explain ()* method in GEE, providing insights into the contribution of specific spectral bands and indices to classification accuracy across different seasons.

2.3. RESULTS

2.3.1. Water hyacinth spectral reflectance curve

Seasonal spectral response curves for water, water hyacinth, cultivated land, grazing land, and forest around Lake Tana were analyzed using Sentinel-2 data (Figure II-4). The spectral reflectance of each land use/cover (LULC) type varied seasonally. Water hyacinth exhibited the highest reflectance in the Red Edge 2 (B6), Red Edge 3 (B7), Near-Infrared (B8), and Red Edge 4 (B8A) bands during the post-rainy, dry, and pre-rainy seasons. In contrast, at the beginning of the rainy season, water hyacinths had lower spectral reflectance compared to forest and grazing land in these bands. During the post-rainy season, forests had higher reflectance than cultivated land, grazing land, and water in the B6, B7, B8, and B8A

bands. However, in the dry and pre-rainy seasons, forest reflectance was lower than that of cultivated land and grazing land, respectively. Overall, water hyacinth reflectance peaked during the post-rainy season and was lowest at the beginning of the rainy season (Figure II-4).

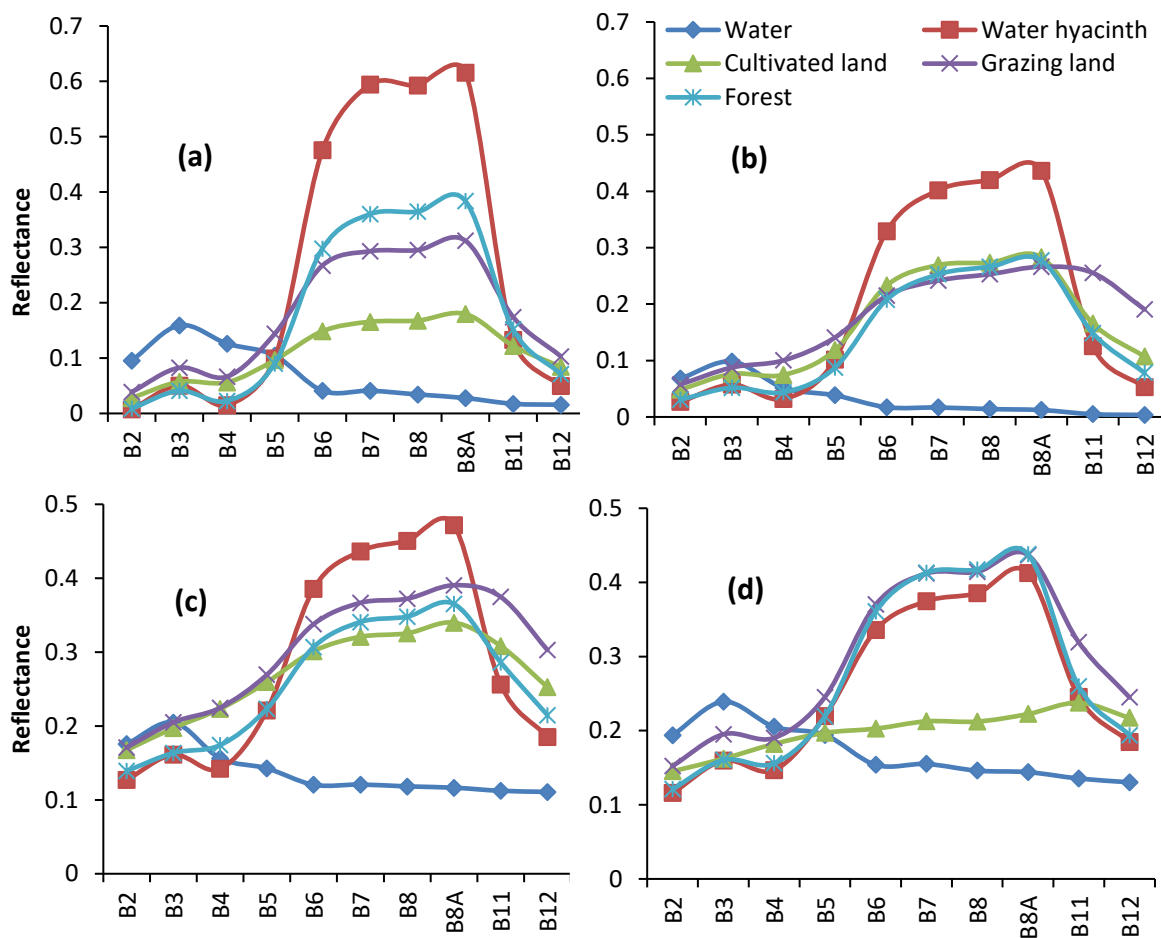


Figure II-4. Average spectral reflectance curves of different land-use/cover types in and around Lake Tana from Sentinel-2 during (a) post-rainy season (October 2021), (b) dry season (January 2022), (c) pre-rainy season (March 2022), and (d) rainy season (June 2022).

2.3.2. Performances of the machine learning algorithms

All three machine learning classifiers—SVM, CART, and RF—were able to detect the spatial distribution of water hyacinths in Lake Tana using Sentinel-2 images (Figures II-5–II-8). However, CART and SVM exhibited some misclassification of other vegetation

types as water hyacinths, as highlighted by the black oval shapes in the figures (Figures II-5a, c; II-6a, c; II-7a, c; II-8a, c). Misclassification was more prevalent in SVM during the post-rainy, dry, and rainy seasons (Figures II-5c, II-6c, II-8c), while in CART, it was more prevalent during the pre-rainy season (Figure II-7a). Similarly, the RF classifier showed some misclassification of other vegetation as water hyacinths during the dry season (Figure II-6b). Additionally, CART misclassified some water as other vegetation during the post-rainy and dry seasons (Figures II-5a, II-6a), and both CART and SVM misclassified some water hyacinths as other vegetation during the dry season (Figures II-6a, c).

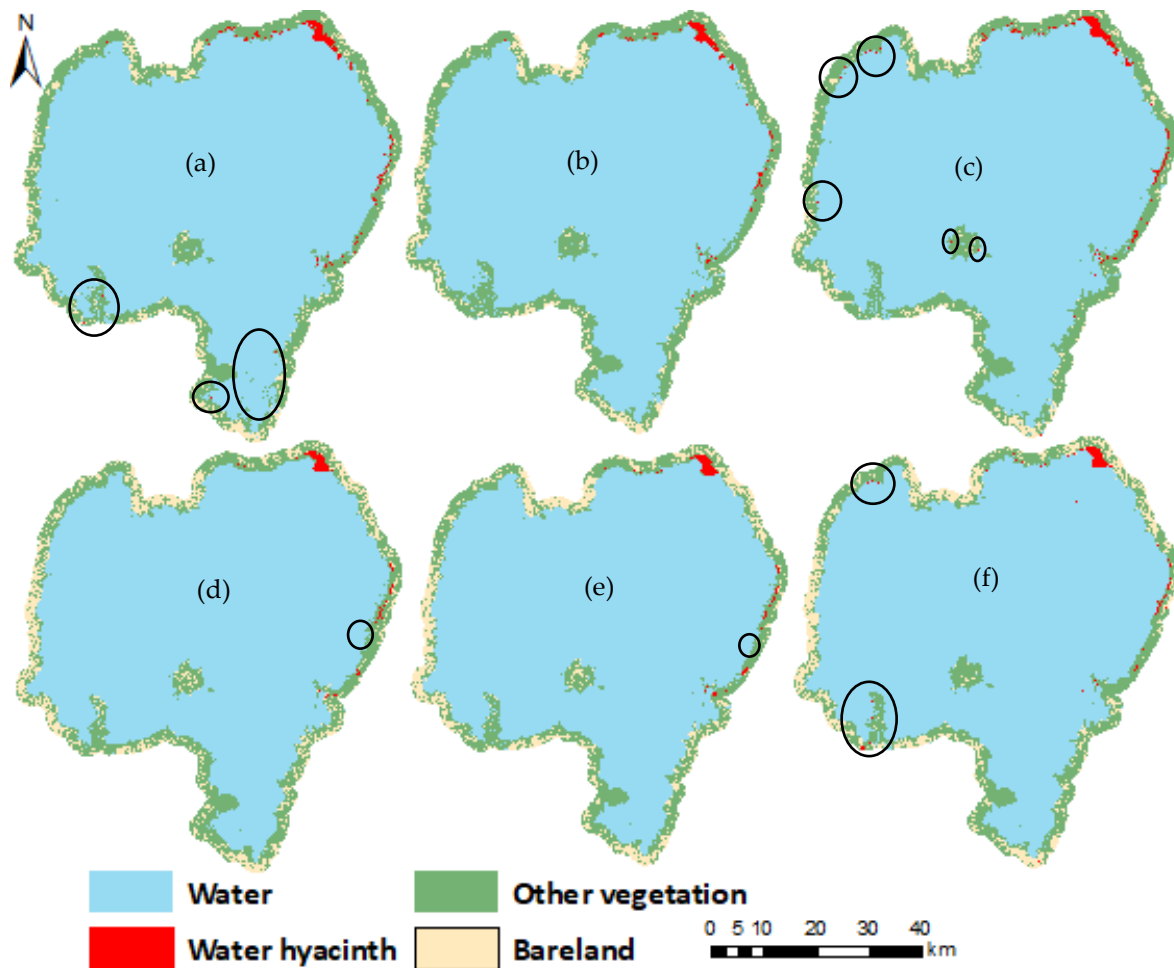


Figure II-5. Comparison of machine learning classifiers for the post-rainy season (October 2021): Sentinel-2 imagery classified by (a) CART, (b) RF, and (c) SVM, and Landsat-8 imagery classified by (d) CART, (e) RF, and (f) SVM land-use/cover maps. The black oval shapes highlight areas of misclassification.

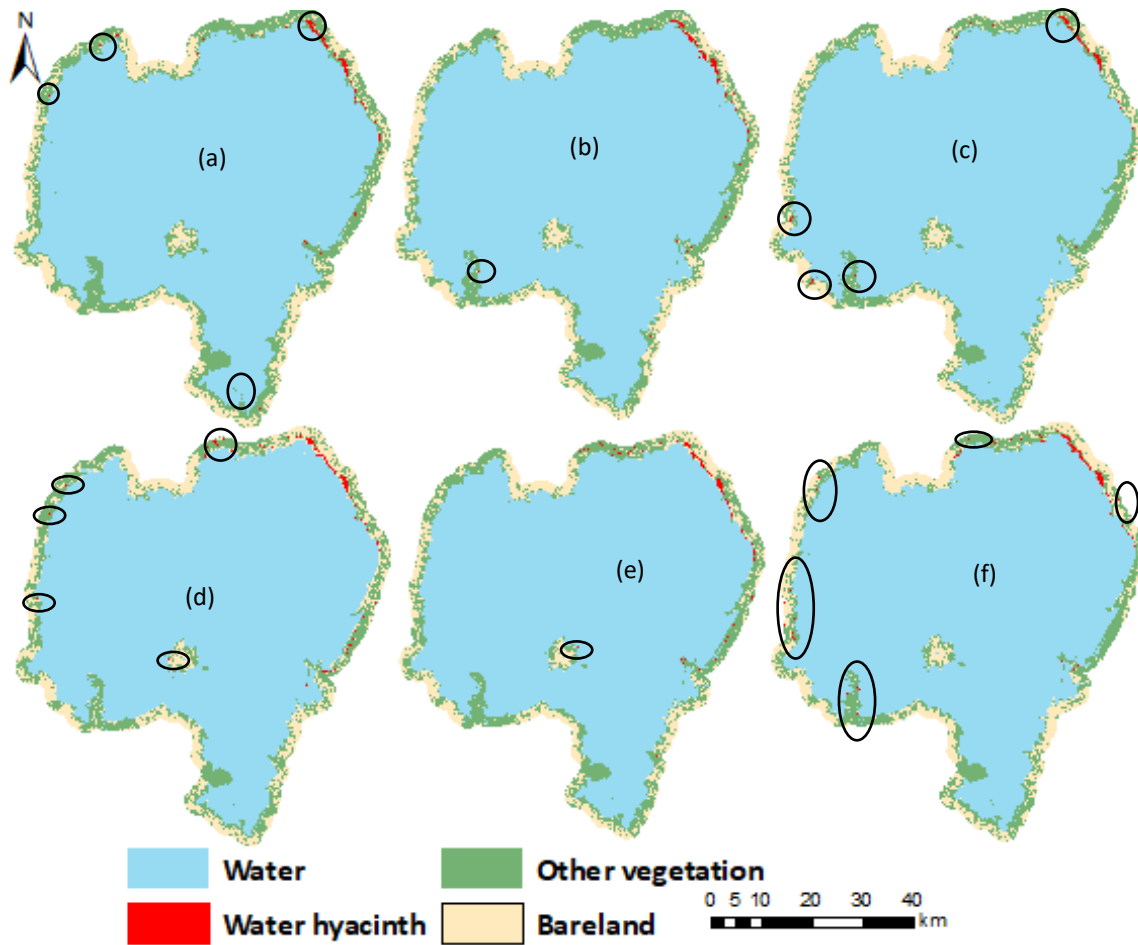


Figure II-6. Comparison of machine learning classifiers for the dry season (January 2022): Sentinel-2 imagery classified by (a) CART, (b) RF, and (c) SVM, and Landsat-8 imagery classified by (d) CART, (e) RF, and (f) SVM land-use/cover maps. The black oval shapes highlight areas of misclassification.

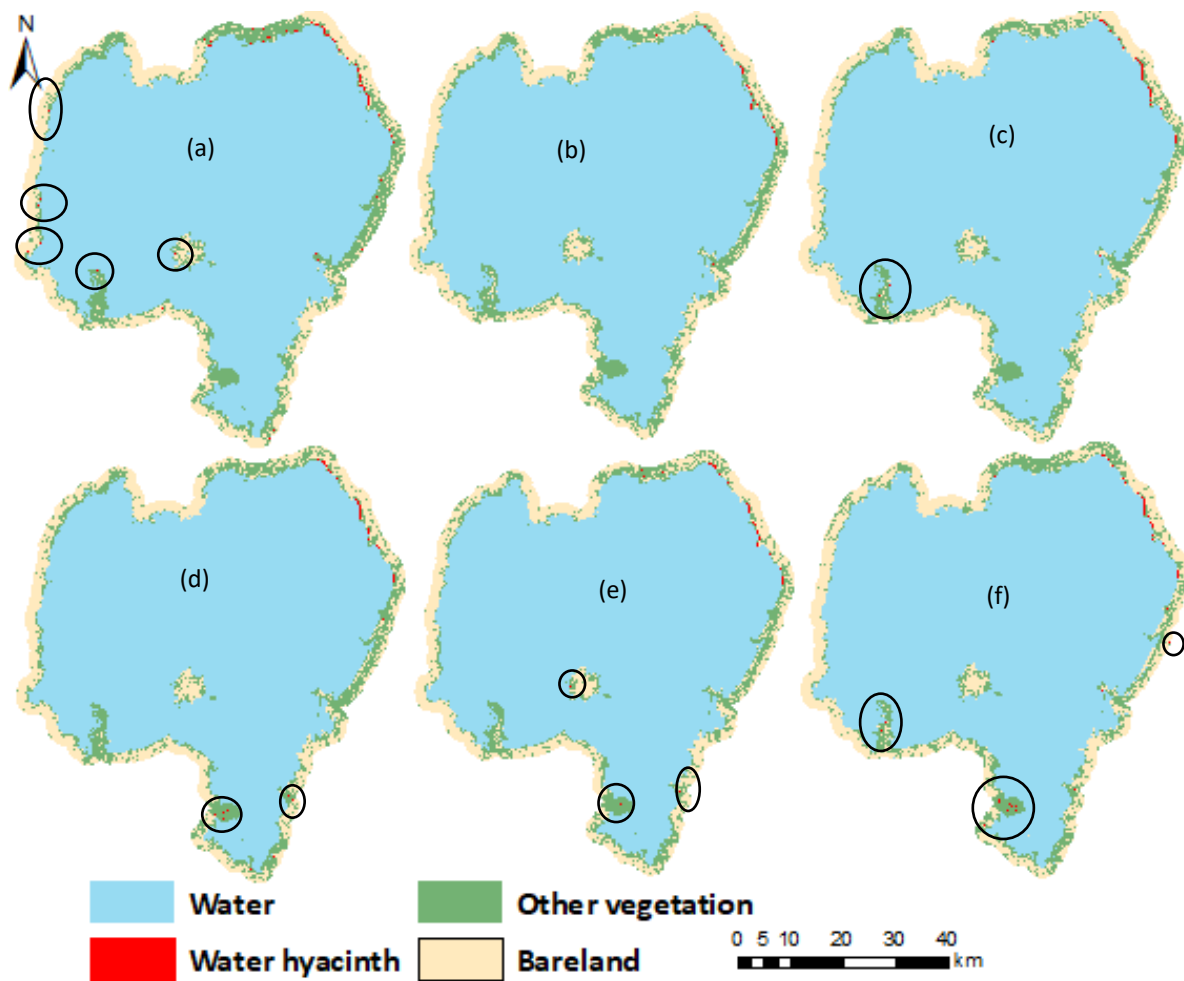


Figure II-7. Comparison of machine learning classifiers for the pre-rainy season (March 2022): Sentinel-2 imagery classified by (a) CART, (b) RF, and (c) SVM, and Landsat-8 imagery classified by (d) CART, (e) RF, and (f) SVM land-use/cover maps. The black oval shapes highlight areas of misclassification.

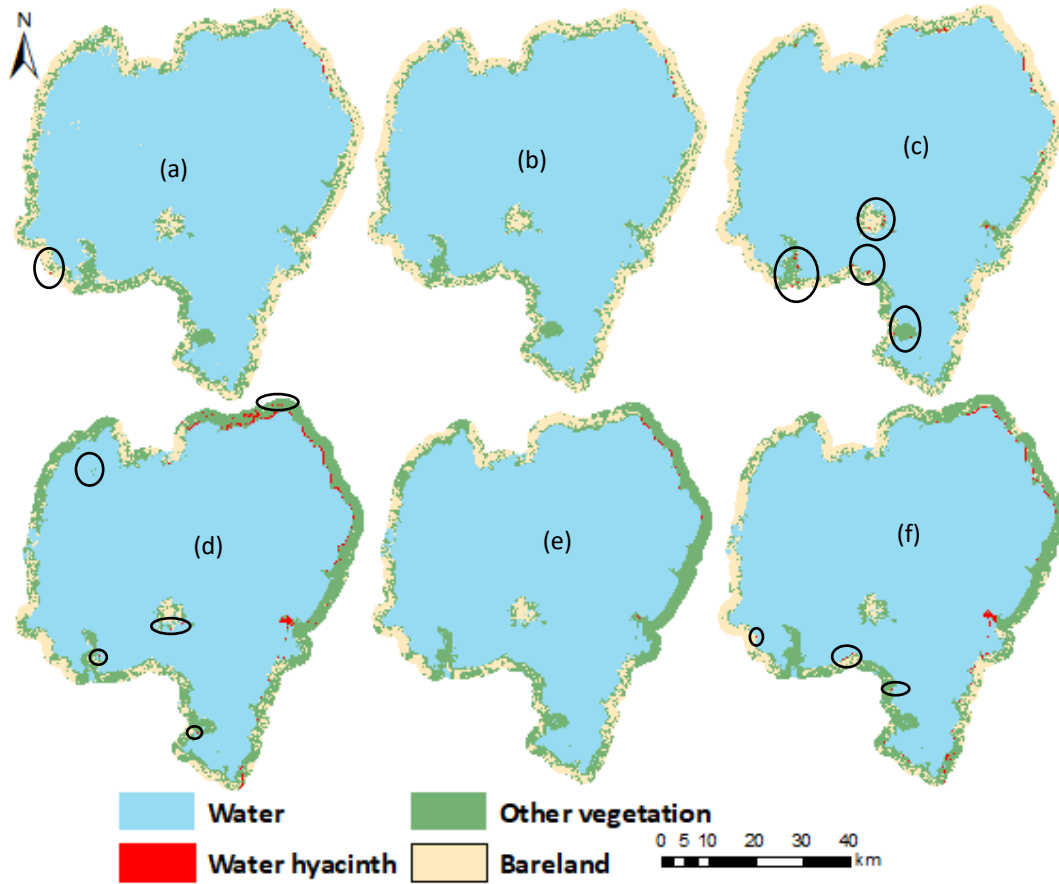


Figure II-8. Comparison of machine learning classifiers for the rainy season (June 2022): Sentinel-2 imagery classified by (a) CART, (b) RF, and (c) SVM, and Landsat-8 imagery classified by (d) CART, (e) RF, and (f) SVM land-use/cover maps. The black oval shapes highlight areas of misclassification.

SVM, CART, and RF were also able to detect the spatial distribution of water hyacinths in Lake Tana using Landsat-8 images (Figures II-5–II-8). However, during the dry, pre-rainy, and rainy seasons, CART and SVM exhibited some misclassification of other vegetation as water hyacinth, as indicated by the black oval shapes in the figures (Figure II-6d, f; Figure II-7d, f; Figure II-8d, f). Misclassification of other vegetation as water hyacinth was most prevalent in SVM during the post-rainy, dry, and pre-rainy seasons (Figures II-5f, II-6f, II-7f). CART also showed higher misclassification of other vegetation types as water hyacinth, particularly during the rainy season (Figure II-8d). Similarly, RF misclassified some vegetation as water hyacinth during the dry and pre-rainy seasons in Landsat-8 images

(Figures II-6e; II-7e). Additionally, water was misclassified as other vegetation in the CART classifier during the post-rainy and rainy seasons in Landsat-8 data (Figures II-5d, II-8d). Likewise, RF misclassified water as vegetation during the post-rainy season in Landsat-8 images. Overall, the RF algorithm demonstrated higher accuracy in detecting water hyacinths than SVM and CART across all seasons and in both Landsat-8 and Sentinel-2 images, as corroborated by field observations and visual evidence presented in the figures (Figures II-5–II-8).

The spatial coverage of water hyacinth and other LULC types varied across the three methods in all seasons. For example, during the post-rainy season, the estimated spatial coverage of water hyacinth was 22 km², 25 km², and 29 km² for RF, CART, and SVM, respectively, in Sentinel-2 images. In contrast, the coverage in Landsat-8 images was 20 km², 18 km², and 21 km² for RF, CART, and SVM, respectively. In the post-rainy season Sentinel-2 image, differences of 2.7 km² and 6.6 km² in water hyacinth spatial coverage were observed between RF and CART, and RF and SVM, respectively. This indicates that the misclassification of other LULC types as water hyacinths was more prevalent with the SVM method compared to the others during the post-rainy season. The largest misclassification of other LULC types occurred in the rainy season Landsat-8 CART and SVM classified images, with area differences of 10.13 km² and 8.59 km² compared to the RF results, respectively. Overall, in both Sentinel-2 and Landsat-8 datasets, the spatial coverage of water hyacinth and other LULC types differed significantly across the methods (RF, CART, and SVM) in all seasons.

This study revealed that Sentinel-2 classified images consistently achieved an overall accuracy exceeding 95% across all classifiers. RF demonstrated the best performance, with accuracy ranging from 97% to 99% and *Kappa* coefficients between 0.97 and 0.99. SVM and CART closely followed, with overall accuracies between 97% and 98%, and *Kappa* coefficients ranging from 0.96 to 0.98 for SVM and 0.96 to 0.97 for CART. RF had the highest average overall accuracy (98.3%), while SVM (97.6%) and CART (97.5%) showed nearly comparable performance (Figure II-9).

For Landsat-8 classified images, overall accuracy exceeded 93% for all classifiers. RF achieved the highest range of accuracy (95% to 98%) and *Kappa* coefficients (0.94 to 0.97), while SVM and CART demonstrated slightly lower accuracy (94% to 96%) and *Kappa* coefficients (0.92 to 0.95). Despite smaller differences, RF consistently outperformed SVM and CART, with an average accuracy of 96.8% compared to 94.8% for SVM and 95% for CART (Figure II-9). Although all classifiers performed well, overall accuracy classification accuracy and *Kappa* coefficients were slightly lower with Landsat-8 compared to Sentinel-2. Overall, RF emerged as the most effective method across both datasets and seasons, providing the highest accuracy and reliability in LULC classification—including water hyacinth detection—around Lake Tana.

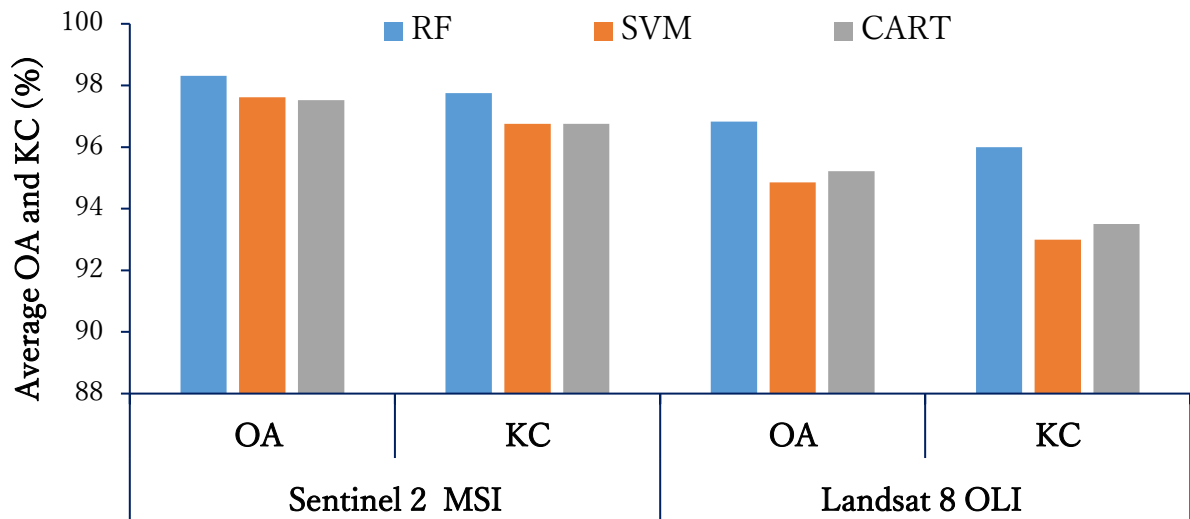


Figure II-9. Comparison of average overall accuracy (OA) and *Kappa* coefficient (KC) for the three classifiers applied to Sentinel-2 MSI and Landsat-8 OLI imagery.

Sentinel-2 classified images for water hyacinth detection consistently achieved high user accuracies across all methods (RF, CART, and SVM) in all seasons. RF achieved the highest range (97% to 100%), followed by SVM (96% to 100%) and CART (94% to 100%). Producer accuracy also exceeded 91% across all methods and seasons. The average F1 score was highest for RF (99%), followed by SVM (98.2%) and CART (98.1%) (Figure II-10). Although the differences in user accuracy, producer accuracy, and F1 scores were small, RF consistently outperformed SVM and CART in Sentinel-2 images. The highest F1 scores (100%) and *Kappa* coefficients (0.97 to 0.98) were recorded during the post-rainy season,

while the lowest F1 scores (94% to 95%) and *Kappa* coefficients (0.96 to 0.97) were observed during the dry season across all classifiers.

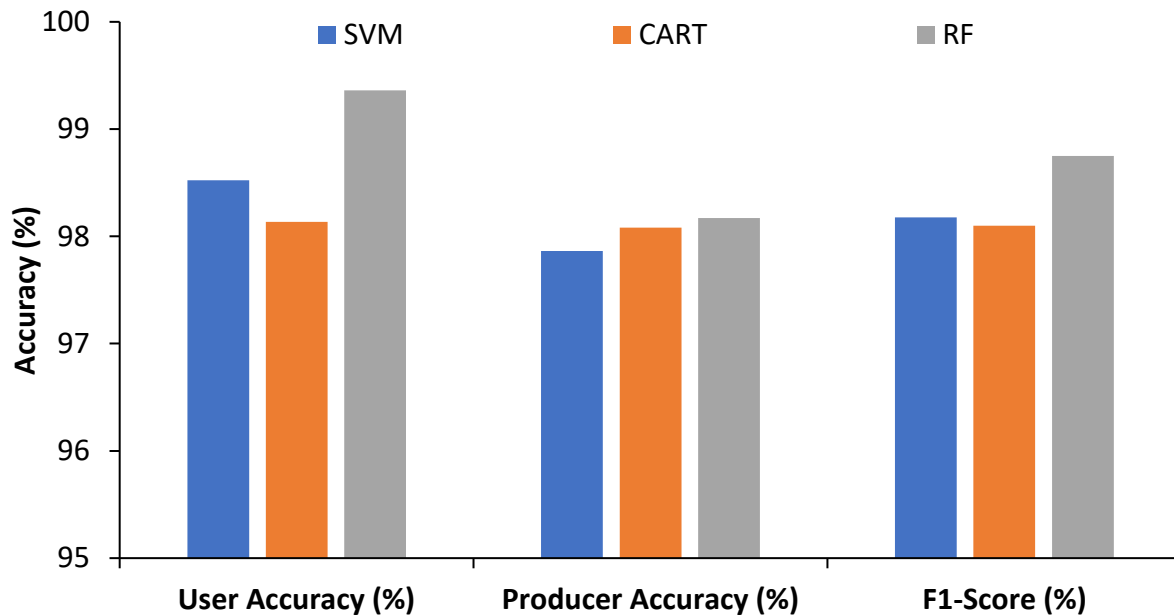


Figure II-10. Comparison of average user accuracy, producer accuracy, and F1-score for the three classifiers applied to Sentinel-2 imagery

User accuracy for water hyacinth detection using Landsat-8 imagery ranged from 93% to 98% for RF, 90% to 99% for CART, and 88% to 98% for SVM across all seasons. Producer accuracy was similarly high, ranging from 96% to 100% for RF, 94% to 99% for CART, and 88% to 100% for SVM. The F1 scores reflected these trends, ranging from 94.8% to 98.9% for RF, 92% to 98.9% for CART, and 88.9% to 98.9% for SVM. RF consistently outperformed CART and SVM across all metrics—overall accuracy, *Kappa* coefficient, user accuracy, producer accuracy, and F1 score—in both Landsat-8 and Sentinel-2 classified images (Figure II-9; Figure II-10; Figure II-11). However, the average accuracy for Landsat-8 classified images was lower than that of Sentinel-2 for all classifiers. The highest accuracy was observed during the post-rainy season for all classifiers in both datasets.

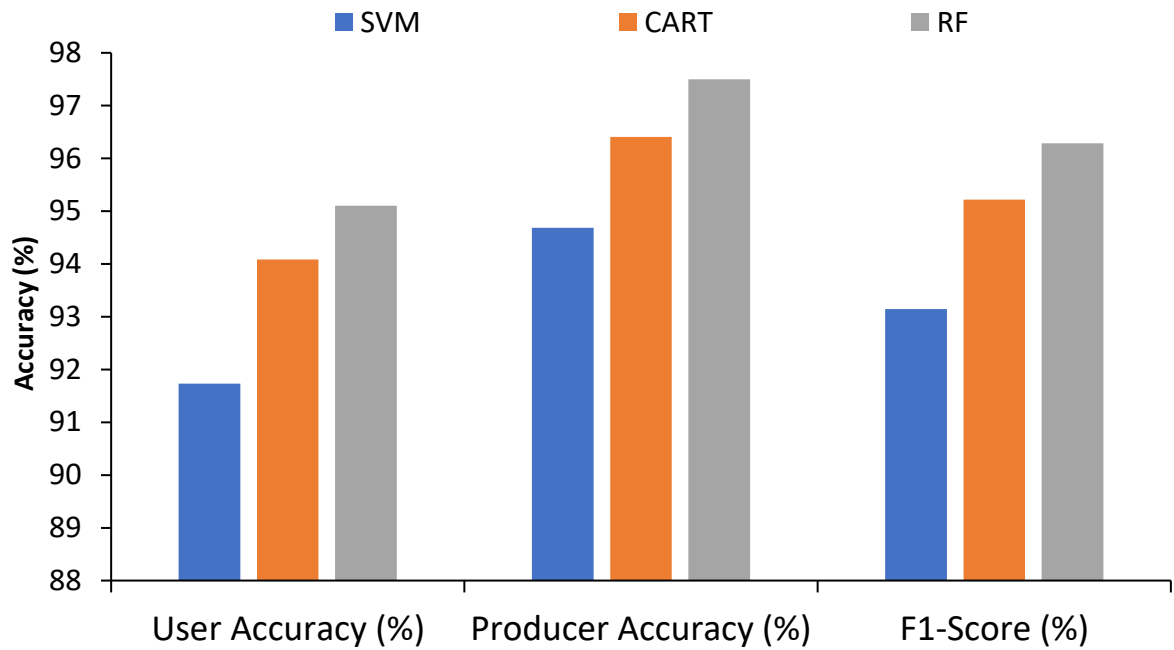


Figure II-11. Comparison of average user accuracy, producer accuracy, and F1-score for the three classifiers applied to Landsat-8 imagery

2.3.3. Feature importance

The importance of spectral bands and indices in the RF classifier varied across seasons (Figure II-12). In the Sentinel-2 datasets, both spectral indices and spectral bands were identified as the most significant variables for classification. Specifically, the Shortwave Infrared 2 (B12) band showed the highest contribution to image classification during the post-rainy and dry seasons. In contrast, the Simple Ratio Index (SRI) and Blue (B2) band were the most influential during the pre-rainy and rainy seasons, respectively.

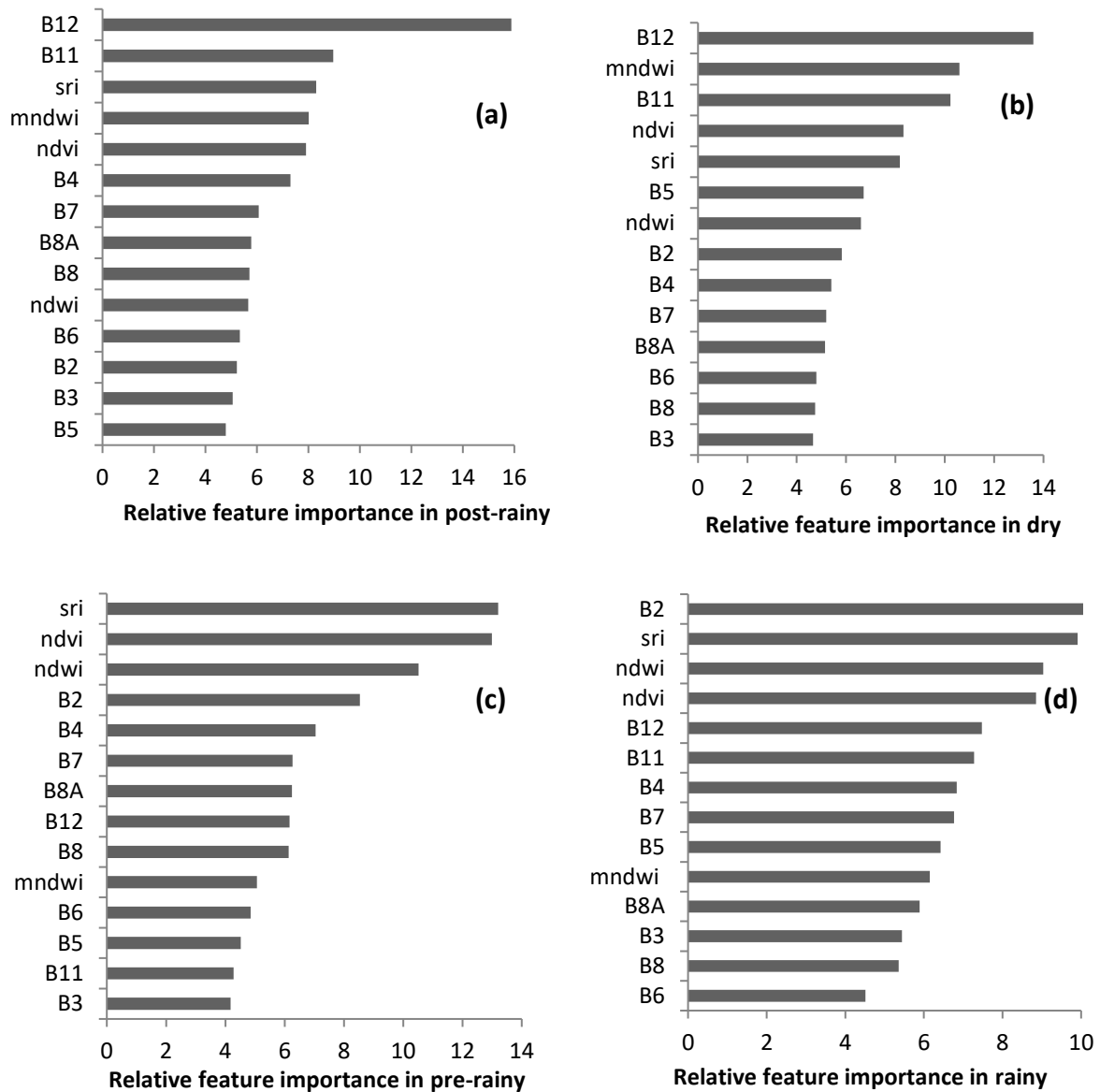


Figure II-12. Relative feature importance of the RF classified images for post-rainy season (a), dry season (b), pre-rainy season (c), and (d) rainy season from Sentinel-2 images.

2.4. DISCUSSION

Seasonal spectral response curves derived from Sentinel-2 data were analyzed to distinguish water hyacinth from other land use/land cover (LULC) types (Figure II-4). Previous research has similarly utilized satellite data and field measurements to differentiate water hyacinths from other LULCs. For example, Datta et al. (2021) employed Sentinel-2

imagery to separate water hyacinths from other aquatic macrophytes, noting that submerged macrophytes exhibited lower reflectance in the near-infrared (NIR) band. Likewise, Verma et al. (2003) reported that water hyacinths in southern Texas waterways had higher NIR reflectance compared to related species and water, based on field measurements. In this study, water hyacinths exhibited higher reflectance in the NIR and red-edge regions during the post-rainy, dry, and pre-rainy seasons (Figure II-4), consistent with findings from earlier studies (Verma et al., 2003; Datta et al., 2021). However, during the rainy season, water hyacinths displayed lower spectral reflectance in these bands compared to forest and grazing land. These results highlight the seasonal variability in spectral responses and reinforce the utility of Sentinel-2 data for accurately distinguishing water hyacinths from other LULC types under varying environmental conditions.

Each common machine learning algorithm has unique strengths and weaknesses (Loukika et al., 2021). For example, while SVM is highly sensitive to hyperparameters, RF is more robust, effectively managing noise and parameter variability (Chang et al., 2019; Jin et al., 2018). SVM performs well with limited training samples (Shao & Lunetta, 2012), whereas CART's performance is also sensitive to sample size (Loukika et al., 2021). In this study, RF consistently outperformed SVM and CART for water hyacinth detection in both Landsat-8 and Sentinel-2 datasets, demonstrating superior F1 scores, overall accuracy, and *Kappa* coefficients across all seasons. CART and SVM showed nearly equivalent performance, supporting the conclusion that RF's robustness against noise and sensitivity to parameters makes it a highly effective algorithm. These findings align with Mukarugwiro et al. (2019), who reported RF's superiority over SVM for water hyacinth detection in Rwandan water bodies. Similarly, Loukika et al. (2021) and Shetty et al. (2021) confirmed RF's effectiveness for LULC classification. Additionally, Shetty et al. (2021) noted similar performances for CART and SVM in LULC classification. However, Shao and Lunetta (2012) observed that SVM outperformed CART when using MODIS images with limited training data points, highlighting SVM's strength in scenarios with fewer samples. These differences emphasize the importance of selecting an algorithm based on dataset characteristics, including size and complexity.

RF, CART, and SVM were all able to detect and distinguish water hyacinths from other LULC types in Lake Tana using Landsat-8 and Sentinel-2 images (Figures II-5 to II-8). However, SVM and CART exhibited misclassification issues, detecting other vegetation types as water hyacinths, likely due to the similar spectral reflectance characteristics of dense vegetation and water hyacinths. Moreover, in Landsat-8 images, CART and RF misclassified some water as vegetation during the post-rainy and rainy seasons, possibly due to high algae or phytoplankton concentrations in the lake, which can alter the spectral reflectance of water. These findings emphasize the importance of considering seasonal and environmental factors when employing machine learning algorithms for LULC classification.

The average accuracy of RF, CART, and SVM exceeded 95% for Sentinel-2 and 90% for Landsat-8 images. Despite small differences in accuracy among the methods, there was notable variation in the estimated spatial coverage of water hyacinth. For example, during the post-rainy season, water hyacinth spatial coverage was estimated at 22 km², 25 km², and 29 km² for RF, CART, and SVM, respectively, in Sentinel-2 images, and 20 km², 18 km², and 21 km² for RF, CART, and SVM in Landsat-8 images. While classification accuracy does not always increase with higher spatial and spectral resolution (Fisher et al., 2018), Sentinel-2 images in this study achieved higher F1 scores, overall accuracy, and *Kappa* coefficients compared to Landsat-8. The overall accuracy for Sentinel-2 averaged 97.8%, whereas Landsat-8 achieved 95.5%. This superior accuracy of Sentinel-2 is likely attributed to its higher spatial resolution and the inclusion of red-edge bands. These findings align with Thamaga and Dube (2018), who also observed Sentinel-2 outperforming Landsat-8 in detecting water hyacinths in South Africa's Greater Letaba River system. Although the accuracy difference between datasets was relatively small, the estimated spatial coverage of water hyacinth varied significantly depending on the algorithm and satellite data used. These results underscore the importance of selecting the most suitable algorithm and dataset for accurately estimating the spatial coverage of water hyacinths.

The F1 score for the water hyacinth class was highest during the post-rainy season for all three classifiers in both datasets, while the lowest value occurred during the dry and pre-rainy seasons. This decline in accuracy during the dry and pre-rainy seasons is likely due

to the presence of irrigated crops around Lake Tana, as some dense irrigated crops exhibit reflectance values similar to those of water hyacinths, making differentiation challenging. Additionally, during the dry and pre-rainy seasons, water hyacinth leaves undergo color changes and drying, which alter their reflectance and negatively impact classification accuracy. In contrast, the leaves turn bright green with higher reflectance at the end of the rainy season (post-rainy season), enhancing detection accuracy significantly (Dersseh et al., 2020). Moreover, the importance of spectral bands and indices in the RF classifier varied seasonally, reflecting the need for season-specific tuning of the classifier.

2.5. CONCLUSIONS

This study evaluated the performance of RF, SVM, and CART machine learning algorithms for detecting water hyacinths in Lake Tana using Landsat-8 and Sentinel-2 images within the GEE platform. All three methods were able to detect water hyacinth, with Sentinel-2 outperforming Landsat-8 by achieving over 95% overall accuracy and an F1 score exceeding 93% across all seasons, compared to over 90% overall accuracy and an 89% F1 score for Landsat-8. Among the classifiers, RF consistently demonstrated superior performance, achieving the highest overall accuracy, *Kappa* coefficient, and F1 score across all seasons. The average overall accuracy was 97.8% for Sentinel-2 and 95.5% for Landsat-8 images. The F1 score for the water hyacinth class was highest during the post-rainy season for all classifiers in both datasets, identifying this as the optimal season for water hyacinth detection. These findings suggested RF as the most accurate algorithm for water hyacinth detection, particularly when applied to Sentinel-2 and Landsat-8 images during the post-rainy season. Accurate classification methods and accurate spatial coverage estimation are critical for devising effective water hyacinth management and control strategies, contributing to sustainable ecosystem management in Lake Tana.

CHAPTER THREE

3. SPATIOTEMPORAL VARIABILITY OF WATER HYACINTH (*EICHHORNIA CRASSIPES*) AND ITS ASSOCIATED WATER LOSS IN LAKE TANA, ETHIOPIA

3.1. INTRODUCTION

Water is one of Earth's most vital resources, offering critical socio-economic and ecological benefits (Thamaga & Dube, 2018). However, freshwater systems, including lakes, are increasingly under threat from pollution, agricultural expansion, urbanization, climate change, and poor watershed management (Danbara, 2014; Das, 2021; Lymburner et al., 2016; Mucheye et al., 2022; Tauchnitz et al., 2020; Tibebe et al., 2019). These pressures contribute to lake eutrophication and facilitate the spread of invasive aquatic species like water hyacinths (Cai et al., 2023; Tibebe et al., 2019). Water hyacinth poses significant challenges for environmental conservation and water resource management due to its detrimental effects on aquatic ecosystems and human livelihoods (Thamaga & Dube, 2018). The invasive species disrupts habitats, food chains, nutrient cycles, and aquatic communities, ultimately altering the entire food web (Coetzee et al., 2014). Recognized for its harmful impact, the International Union for Conservation of Nature (IUCN) lists water hyacinth among the world's top 100 worst invasive species (Téllez et al., 2008), while it ranks as one of the top 10 most problematic weeds globally (Dersseh et al., 2020).

In tropical highland lakes like Lake Tana in Ethiopia, water hyacinth affects biodiversity, navigation, tourism, and water quality (Damtie et al., 2022). Additionally, it contributes to water loss through elevated evapotranspiration rates in infested areas (Abebe et al., 2023; Damtie et al., 2021). First identified in Lake Tana in 2011, water hyacinth has since spread rapidly, posing a serious threat to the lake's ecological balance and water resources. Lake Tana has a total shoreline of approximately 385 km, with over 30% now affected by water hyacinth infestation. The severity of this infestation varies both spatially and temporally. Therefore, understanding the spatiotemporal distribution and growth

dynamics of water hyacinth is essential for developing effective mitigation and management strategies.

Accurate and timely information on the spatial and temporal distribution of water hyacinths is crucial for effective control efforts (Shekede et al., 2008). Currently, data on water hyacinth distribution in Lake Tana is collected through traditional field surveys conducted by the Lake Tana and Other Water Bodies Protection and Development Agency (LTPDA). However, these surveys are labor-intensive, costly, and often constrained by challenges such as limited accessibility, security concerns, budget limitations, and inadequate infrastructure, making timely updates difficult. Freely available satellite data, such as Sentinel-2 imagery, provides a more efficient and cost-effective alternative. These satellite sensors enable frequent monitoring and deliver accurate, up-to-date information on water hyacinth spatiotemporal distribution, which is crucial for understanding its dynamics (Mukarugwiro et al., 2021; Thamaga & Dube, 2018).

Water hyacinths, with their high density of stomata on the upper leaf surface, significantly increase water loss through transpiration, resulting in much higher evapotranspiration rates compared to open-water surfaces (Maylani et al., 2020). The dense mats formed by water hyacinths exacerbate this effect, further increasing evapotranspiration and posing a serious environmental challenge (Damtie et al., 2021; Sasaqi et al., 2019). While there is ongoing debate about the evapotranspiration rates of water hyacinths compared to open water, numerous studies have consistently reported significantly higher water loss associated with the presence of water hyacinths (Arp et al., 2017; Timmer & Weldon, 1966; Damtie et al., 2021; Rashed, 2014). For example, while open-water evaporation averages 4.3 mm/day, water hyacinth-infested areas can experience evapotranspiration rates as high as 7.8 mm/day (Maylani et al., 2020). Similarly, experimental tanks infested with water hyacinths demonstrated a 53% increase in evapotranspiration compared to open water (Arunpandi et al., 2022). These elevated rates contribute significantly to reduced water storage capacity in lakes infested by water hyacinths, including Lake Tana (Damtie et al., 2021). A literature review conducted by Dersseh et al. (2019) indicates that water hyacinth-covered water bodies exhibit higher evapotranspiration rates than open water under environmental conditions

similar to those in Lake Tana. However, despite studies from other regions on water hyacinth's impact on lake hydrology, limited efforts have specifically examined its effect on water loss due to evapotranspiration in Ethiopia, particularly in Lake Tana (Dersseh et al., 2019).

Previous studies on the spatiotemporal distribution of water hyacinth in Lake Tana have predominantly relied on parametric algorithms (Abebe et al., 2023; Asmare et al., 2020; Damtie et al., 2021, 2022; Worqlul et al., 2020). While Dersseh et al. (2020) utilized random forests (RF), their analysis was limited to spectral bands. Additionally, Abebe et al. (2023) manually digitized water hyacinth from Sentinel-2 imagery to assess spatial coverage but faced challenges distinguishing it from other aquatic vegetation. Most studies used maximum likelihood classifiers and lower-resolution Landsat-5 and Landsat-8 imagery, with the majority conducted before 2019. Despite these efforts, previous studies have largely focused on single-time analyses, with only Dersseh et al. (2020) and Abebe et al. (2023) covering the period from 2016 to 2019. Seasonal and annual spatial coverage analyses incorporating data from all months remain unexplored for the period from 2015 to 2023. This lack of temporal depth limits our understanding of water hyacinth's distribution patterns and growth dynamics. Moreover, water loss due to water hyacinth evapotranspiration has not been thoroughly studied. Existing research in Lake Tana (Abebe et al., 2023; Damtie et al., 2021) has relied on water hyacinth plant coefficients derived from other regions, underscoring the need for further research with region-specific coefficients. Expanding research on these aspects will provide critical insights into the spatiotemporal dynamics and hydrological impacts of water hyacinths, essential for developing effective management strategies.

Therefore, this study aims to analyze the spatiotemporal dynamics of water hyacinth and its associated water loss due to evapotranspiration. Specifically, the objectives were to (1) determine the spatiotemporal coverage of water hyacinth from 2015 to 2023 and (2) estimate the water loss caused by water hyacinth evapotranspiration during this period.

3.2. MATERIALS AND METHODS

3.2.1. Data and processing

This study was conducted within and around the shoreline of Lake Tana, with a 1 km buffer zone extending outward from the shoreline. Sentinel-2 Multispectral Instrument (MSI) Level-1C imagery from 2015 to 2023 was utilized to assess the spatiotemporal distribution of water hyacinths. The dataset includes four bands (blue, green, red, and near-infrared) at a 10 m resolution and six bands (red edge 1–4, shortwave infrared 1, and shortwave infrared 2) at a 20 m resolution (Table II-1). To balance spatial resolution with computational efficiency, 10 m resolution bands were resampled to 20 m. Given the challenges of obtaining completely cloud-free imagery in the Lake Tana region, cloud masking was performed in GEE using the QA60 band to exclude cloud-covered pixels. Different cloud cover thresholds were applied based on seasonal variability: less than 10% during the dry, pre-rainy, and post-rainy seasons, and less than 20% during the rainy season (June), which is characterized by higher cloud cover. Monthly median compositing was applied to address data gaps caused by cloud masking, reducing the influence of outliers and erroneous values. To ensure reliable surface reflectance values, atmospheric correction was conducted using the Satellite Invariant Atmospheric Correction (SIAC) package in GEE, converting imagery from top-of-atmosphere to surface reflectance. Due to the limited temporal coverage of Sentinel-2A surface reflectance data, this study utilized Harmonized Sentinel-2 Level-1C data spanning from 2015 to 2023.

A Random Forest (RF) classifier was applied to estimate the spatiotemporal distribution of water hyacinth. The classifier inputs included raw Sentinel-2 spectral bands (blue, green, red, near-infrared, red edge 1–4, shortwave infrared 1 and 2) (Table II-1) and four derived environmental indices: Normalized Difference Vegetation Index (NDVI), Simple Ratio Index (SRI), Normalized Difference Water Index (NDWI), and Modified Normalized Difference Water Index (MNDWI) (Table II-2). These indices were selected based on pairwise correlation analysis to minimize multicollinearity with other input variables (Bayable et al., 2023). To enhance detection accuracy, these indices (NDVI, SRI, NDWI, and MNDWI) and the spectral bands were used together as classifier inputs.

(Thamaga & Dube, 2019). Normalization was performed to ensure consistent data scaling across the spectral bands and indices, improving the RF classifier's accuracy and computational efficiency in detecting water hyacinth. In addition to the Harmonized Sentinel-2 data, Potential Evapotranspiration (PET) data from the MODIS MOD16A2 gap-filled dataset was utilized to estimate lake water evaporation. This dataset was accessed and processed through NASA's Application for Extracting and Exploring Analysis Ready Samples (AppEEARS) tool (<https://appeears.earthdatacloud.nasa.gov/>).

3.2.2. Sample point generation and classification

Images were classified into three land use/land cover (LULC) classes: water (clear and turbid), water hyacinth, and other LULC. The Google Earth Engine (GEE) platform, a highly effective and free cloud-based tool (Gorelick et al., 2017; Zhang et al., 2017), was used for processing and analyzing satellite image data. Field surveys, which included GPS points collected using a handheld Garmin-72 GPS device and smartphone photographs, were conducted on water hyacinth patches in Lake Tana during March 2022, December 2022, and June 2023. These data, along with the visual interpretation of Sentinel-2 images, were used to digitize the LULC classes for these months. Additionally, high-resolution Google Earth images, expert opinions, field knowledge, and reports from the Lake Tana and Other Water Bodies Protection and Development Agency (LTPDA) supported the manual digitization of water, water hyacinth, and other LULC. Irregular polygons representing the three LULC classes from 2015 to 2023 were delineated through expert opinions, field knowledge and Sentinel-2 image visual interpretation. A stratified random sampling method was applied within these delineated polygons to generate random samples. To ensure representative sampling, LULC delineations were evenly distributed across the study area to define strata. The number of training samples was determined proportionally to the area of each LULC class, as this significantly influences classification accuracy. For the classification process, a minimum of 50 training samples per class was required, following the rule of thumb (Thomas et al., 2004). Various experiments using a trial-and-error approach identified the optimal number of training samples for achieving high classification accuracy. Ultimately, 1,800

labeled samples were generated: 800 for water, 400 for water hyacinth, and 600 for other LULC classes. These samples were split, with 70% used for training and 30% for validation, ensuring robust accuracy. The RF algorithm was employed to estimate the spatiotemporal distribution of water hyacinth from 2015 to 2023 due to its superior classification performance (Bayable et al., 2023). Water hyacinth spatial coverage was calculated using the grouped reducer and the *reduceRegion()* function in GEE. Each RF-classified image was evaluated using metrics such as overall accuracy, *Kappa* coefficient, user accuracy, producer accuracy, and F1 score. Additionally, the annual water hyacinth expansion rate was calculated by comparing the maximum water hyacinth spatial coverage over consecutive years. For instance, the expansion rate for 2023 was computed as follows (Dersseh et al., 2020):

$$\begin{aligned} \text{Annual expansion rate 2023(\%)} \\ = \frac{\text{Max area coverage of WH 2023} - \text{Max area coverage of WH 2022}}{\text{Max area coverage of WH 2022}} \times 100 \end{aligned}$$

3.2.3. Water loss estimation

To estimate the water loss due to water hyacinth evapotranspiration, three parameters are required: open-water evaporation, water hyacinth evapotranspiration, and the spatial coverage of water hyacinth. This estimation of water loss due to water hyacinth in the lake assumed that all weeds were spread across the lake water, expanding at the expense of the lake's water. Potential Evapotranspiration (PET) data from MODIS MOD16A2 was selected for its reliability and suitability in estimating open-water evaporation. Since open-water evaporation rates rarely reach 100% of PET values, an adjustment factor was applied to approximate the actual evaporation rate (Ev). According to the US Geological Survey (USGS), Ev is approximately 80% of the PET value (Barclay & Sumner, 2006). The formula for calculating Ev is as follows:

$$\text{Open water evaporation (Ev)} = 0.8 * \text{PET (Barclay \& Sumner, 2006)}$$

A comparison with a similar study conducted in Lake Tana by Damtie et al. (2021), which utilized Ev estimates from the National Meteorological Agency (NMA) Bahir Dar station data (January–December 2020), revealed a strong correlation ($r = 0.82$, $r^2 = 0.67$) with Ev estimates derived from MODIS data (Figure III-1). This indicates that MODIS Ev data is reliable for estimating water evaporation in Lake Tana.

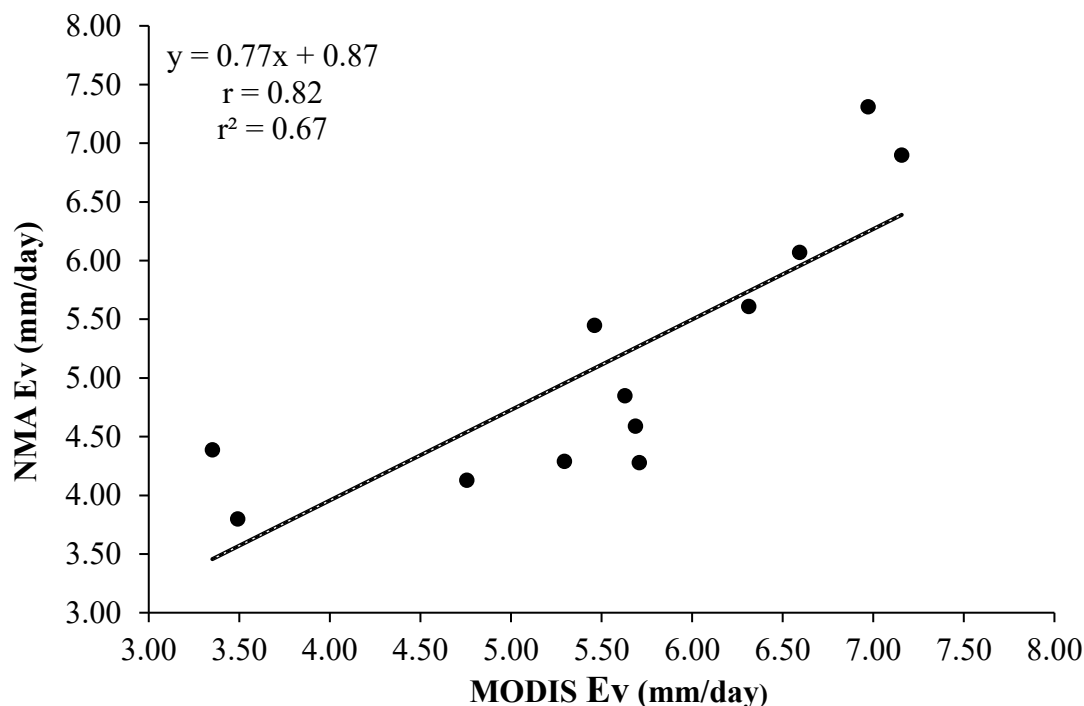


Figure III-1. Comparison of Ev estimates from the MODIS MOD16A2 gap-filled dataset with Ev estimates by Damtie et al. (2021) based on National Meteorological Agency data from Bahir Dar station (January–December 2020)

The plant coefficient (K_c) of water hyacinth reported in the literature ranges from 0.65 to 9.8 (Abebe et al., 2023; Damtie et al., 2021; Jiménez-Rodríguez et al., 2019; Rashed, 2014; Van Der Weert & Kamerling, 1974). According to FAO's irrigation and drainage paper, the K_c value for water hyacinth is 1.1 under light to moderate wind conditions and 1.15 under strong wind conditions in tropical and subtropical regions (Doorenbos & Pruitt, 1977). Similarly, a study conducted in Lake Zeway, Ethiopia, reported a K_c value of 1.42 for water hyacinth (Teshome & Amente, 2022). However, no specific study has determined the K_c value for Lake Tana. Given the absence of Lake Tana-specific studies, this research adopted

the K_c value of 1.42 from Teshome and Amente (2022), as it reflects environmental conditions relevant to Ethiopia. The evapotranspiration of water hyacinth (ET_{wh}) was calculated using the evaporation from open water surfaces (E_v) and the plant coefficient (K_c) of water hyacinth (Rashed, 2014).

$$ET_{wh} = E_v K_c$$

The volume of water loss due to water hyacinth evapotranspiration was then estimated using the following equation (Rashed, 2014).

$$\text{Water loss} = (ET_{wh} * \text{Area of water hyacinth}) * 0.001$$

where water loss is in cubic meters (m³), the area of water hyacinth is in square meters (m²), and ET_{wh} is in millimeters (mm). Furthermore, the modified Mann-Kendall trend test was applied to analyze trends in water hyacinth spatial coverage, evapotranspiration, and water loss from 2015 to 2023. The magnitude of change was quantified using Sen's slope, a robust nonparametric method.

3.3. RESULTS

3.3.1. Spatiotemporal distribution of water hyacinth

All RF-based classifications of Sentinel-2 images from October 2015 to December 2023 consistently achieved overall accuracy above 95%, with *Kappa* coefficients exceeding 0.95. The overall accuracy ranged from 97% to 99.9%, while *Kappa* coefficients varied between 0.97 and 0.99. Water hyacinth detection achieved producer accuracy of 92.68% to 100% and user accuracy of 97% to 100%. Additionally, the F1 score for water hyacinth detection ranged from 95% to 100% during this period.

Water hyacinths are predominantly concentrated in the northern, northeastern, and eastern parts of Lake Tana, with the most severe infestations occurring in the northeastern section (Figure III-2a). During the early study period (2015–2017), the weed was mainly confined to the northern and northeastern areas of the lake (Figure III-2a). However, between 2017 and 2023, it expanded into the eastern and southeastern regions. The highest spatial

distribution of water hyacinth was observed from 2018 to 2021 (Figure III-2). Seasonal variations in spatial coverage were evident, with the weed typically peaking during the post-rainy season and reaching its minimum in the pre-rainy season (Figure III-2b). Over the study period (2015–2023), the spatial coverage of water hyacinth increased significantly at a rate of 0.06 km²/month ($P < 0.05$), as determined by the modified Mann-Kendall trend test.

The annual maximum spatial coverage of water hyacinth in Lake Tana varied over time, ranging from 2.81 km² in November 2015 to 24.69 km² in November 2019 (Table III-1, Figure III-2). Specific values for the annual maximum coverage in different years were as follows: 2.81 km² in November 2015, 4.98 km² in November 2016, 11.26 km² in November 2017, 20.86 km² in December 2018, 24.69 km² in November 2019, 23.58 km² in September 2020, 23.35 km² in October 2021, 11.10 km² in November 2022, and 15.13 km² in November 2023 (Table III-1). The annual maximum spatial coverage expansion rates showed substantial increases during certain intervals: 77% (2015 to 2016), 126% (2016 to 2017), 85% (2017 to 2018), 18% (2018 to 2019), and 36% (2022 to 2023) (Table III-1). Conversely, declines in the annual maximum spatial coverage were observed, with decreases of 4% (2019 to 2020), 1% (2020 to 2021), and 52% (2021 to 2022) (Table III-1). Overall, the annual maximum spatial coverage of water hyacinth increased by 438.94% from 2015 to 2023, reflecting significant long-term expansion trends (Table III-1).

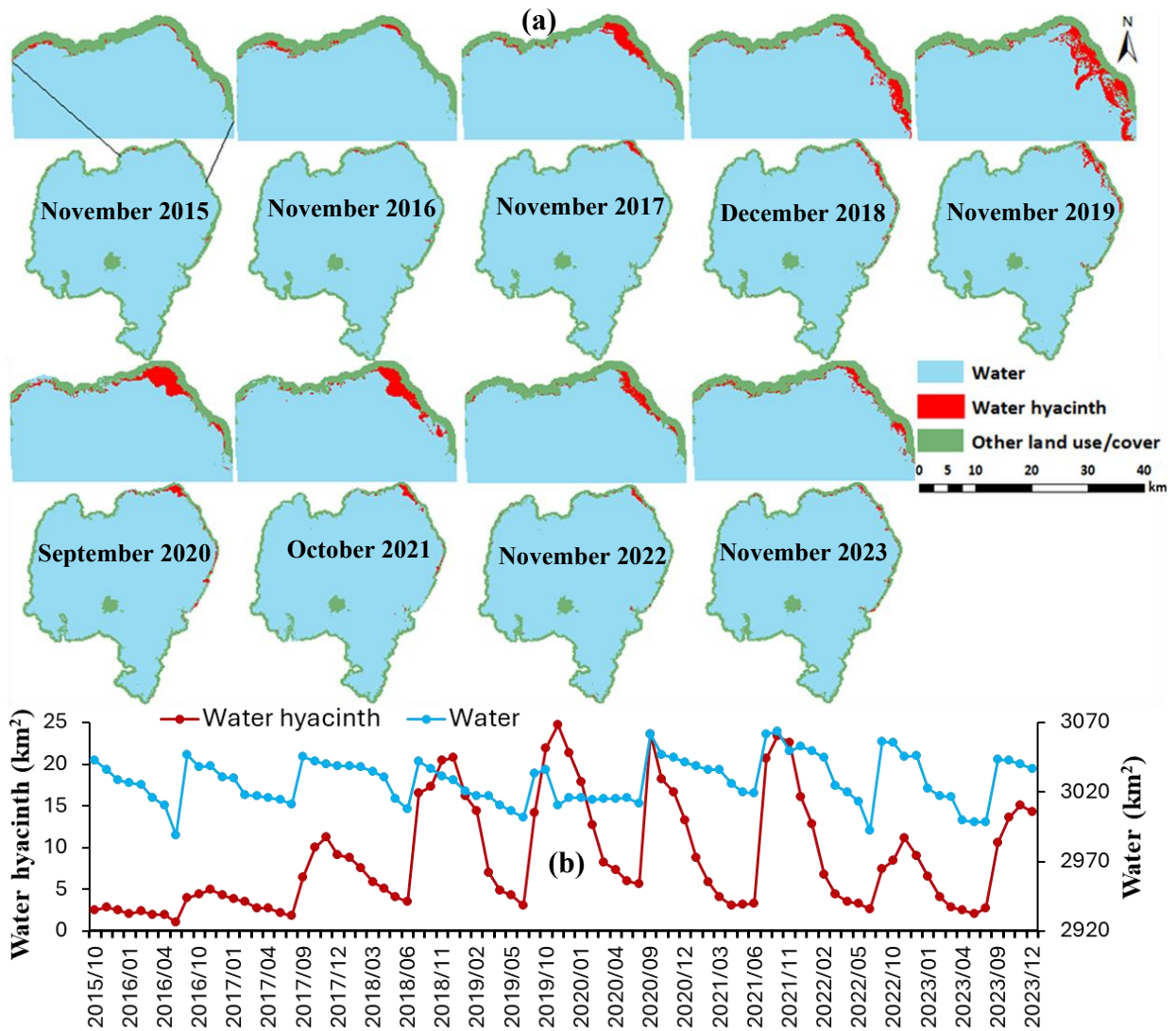


Figure III-2. (a) Spatiotemporal distribution of water hyacinth in the northeastern section and across Lake Tana, showing its maximum spatial coverage from 2015 to 2023; (b) time series of water hyacinth spatial coverage and water surface area from October 2015 to December 2023. Note: Sentinel-2 images for May 2016, and July–August of all study years, were excluded due to extensive cloud cover.

The annual maximum water surface area of Lake Tana varied over time, ranging from 3,036 km² in October 2019 to 3,063.6 km² in October 2021 (Table III-1, Figure III-2). The lake's water surface area was highest between 2020 and 2022 and lowest between 2017 and 2020 (Figure III-2). Overall, the water surface area showed an insignificant increase from 2015 to 2023. The annual maximum water surface area expansion rates increased by 0.14%

(2015 to 2016), 0.84% (2019 to 2020), and 0.07% (2020 to 2021) (Table III-1). Conversely, decreases in expansion rates were observed during the intervals 2016 to 2017 (-0.05%), 2017 to 2018 (-0.12%), 2018 to 2019 (-0.19%), 2021 to 2022 (-0.23%), and 2022 to 2023 (-0.42%) (Table III-1). In general, the annual maximum spatial coverage expansion rate increased slightly by 0.03% from 2015 to 2023 (Table III-1).

Table II-1. Annual maximum (Max.) water hyacinth spatial coverage, lake surface area, and expansion rates (2015–2023).

Year	Annual Max. WH Area (km ²)	Expansion Rate (%)	Annual Max. Water Surface Area (km ²)	Expansion Rate (%)
2015	2.81	-	3042.79	-
2016	4.98	77	3047.04	0.14
2017	11.26	126	3045.59	-0.05
2018	20.86	85	3041.83	-0.12
2019	24.69	18	3035.97	-0.19
2020	23.58	-4	3061.54	0.84
2021	23.35	-1	3063.63	0.07
2022	11.10	-52	3056.47	-0.23
2023	15.13	36	3043.60	-0.42

3.3.2. Water hyacinth evapotranspiration and its associated water loss

In Lake Tana, water hyacinths exhibited varying evapotranspiration rates from October 2015 to December 2023 (Figure III-3). The highest monthly water hyacinth evapotranspiration rate was recorded in May 2022 at 332.56 mm, while the lowest was observed in September 2019 at 181.48 mm. The average monthly evapotranspiration rate during the study period was 239.3 mm. A general decreasing trend in evapotranspiration was observed across all months except May. Significant reductions occurred in April, June, September, and October, whereas May showed a significant increase (Table III-2). The overall trend of water hyacinth evapotranspiration decreased significantly during the study

period ($P < 0.05$). Seasonal variations revealed peaks during the pre-rainy season, with the lowest water hyacinth evapotranspiration rates recorded during the rainy season (Figure III-3).

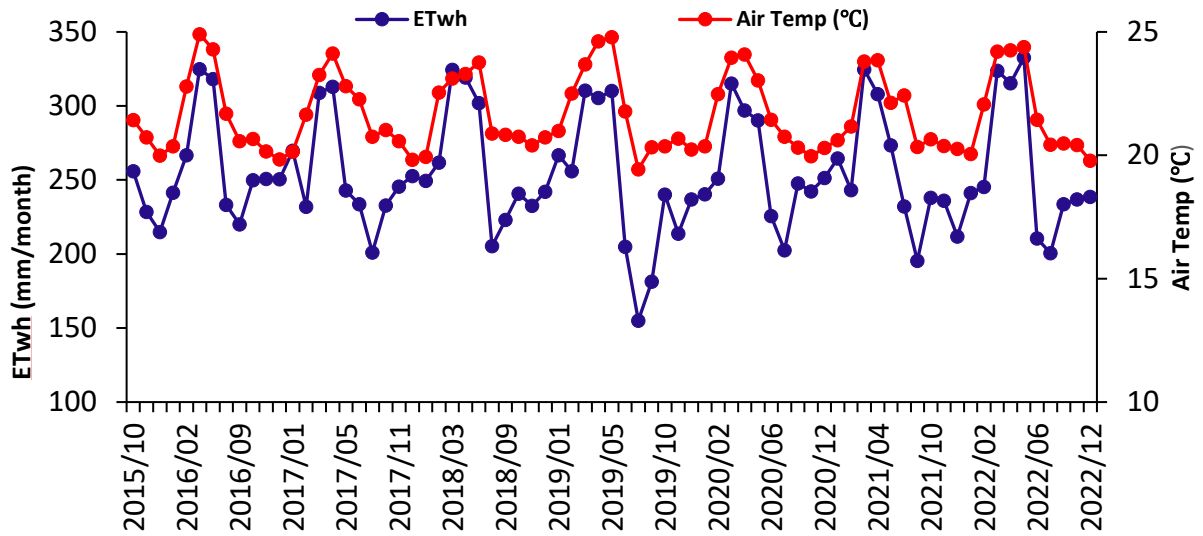


Figure III-3. Time series of water hyacinth evapotranspiration and air temperature from October 2015 to December 2023

Table III-2. The Modified Mann–Kendall trend test analysis of water hyacinth evapotranspiration (2016–2023)

Month	Tau	New P-value	Trend	Sen's Slope (mm/year)
January	-0.11	0.42	Downward	-0.30
February	-0.28	0.11	Downward	-2.60
March	-0.17	0.13	Downward	-0.18
April	-0.56	0.00*	Downward	-3.47
May	0.39	0.00*	Upward	6.72
June	-0.39	0.01*	Downward	-2.92
July	-0.17	0.21	Downward	-4.24
August	-0.06	0.81	Downward	-0.74
September	-0.39	0.00*	Downward	-2.30
October	-0.33	0.01*	Downward	-1.70
November	-0.22	0.09	Downward	-2.04
December	-0.22	0.12	Downward	-2.41
Total (2015-2023)	-0.08	0.00*	Downward	-0.14

Monthly water loss caused by water hyacinth evapotranspiration ranged from 0.25 million m³ in June 2016 to 5.56 million m³ in October 2021, with an average loss of 2.12 million m³. Over the study period, the rate of water loss due to evapotranspiration increased significantly by 0.014 million m³/month ($P < 0.05$). While water loss generally increased from 2016 to 2023 in all months except May, significant increases were observed only in October and November, with annual rates of 0.47 million m³ and 0.38 million m³, respectively (Table III-3). Seasonally, water loss trends increased during the post-rainy, dry, and pre-rainy seasons but were statistically significant only in the post-rainy season, at 0.78 million m³/year. Between October 2015 and December 2023, Lake Tana lost approximately 176 million m³ of water due to water hyacinth evapotranspiration. The highest water loss occurred during the post-rainy season, while the lowest was recorded in the pre-rainy season.

Table III-3. The Modified Mann–Kendall trend test analysis of water loss due to water hyacinth evapotranspiration (2016–2023)

Month/Season	Tau	P-value	Trend	Sen's Slope (m ³ /year)
January	0.29	0.15	Upward	272437.54
February	0.14	0.55	Upward	109277.28
March	0.21	0.35	Upward	100435.74
April	0.07	0.83	Upward	19200.91
May	-0.05	1.00	Downward	-36358.69
June	0.29	0.12	Upward	48732.03
September	0.29	0.12	Upward	158239.12
October	0.44	0.02*	Upward	470027.70
November	0.39	0.03*	Upward	382212.05
December	0.28	0.13	Upward	255689.99
Dry season	0.07	0.84	Upward	403165.26
Pre-rainy season	0.07	0.83	Upward	87598.78
Post-rainy season	0.44	0.01*	Upward	783572.07

3.4. DISCUSSION

3.4.1. Spatiotemporal distribution of water hyacinth

Water hyacinth infestations are predominantly concentrated in the northeastern and eastern parts of Lake Tana, with the most severe occurrences in the northeastern section (Figure III-2). These high populations in these areas are likely driven by favorable environmental factors, including optimal levels of total nitrogen, total phosphorus, pH, salinity, temperature, and depth (Dersseh et al., 2020; Dersseh et al., 2019). Additionally, prevailing westerly winds, which blow eastward for much of the year, transport fragmented water hyacinth mats toward the northeastern region, limiting their spread to other parts of the lake (Cai et al., 2023). The lake's topography further supports this concentration, as the shallow depths in the northeastern coastal area function as floodplains during the dry season and become submerged during the rainy and post-rainy seasons, creating ideal conditions for water hyacinth growth and proliferation.

The spatial coverage of water hyacinth in Lake Tana peaked in 2019 at 24.69 km² and was at its lowest in 2015, with 2.81 km² (Table III-1). From 2015 to 2023, the weed's spatial coverage expanded significantly, at a rate of 0.06 km²/month. However, the annual maximum spatial coverage showed declining expansion rates after 2019, with reductions of 4%, 1%, and 52% between 2019–2020, 2020–2021, and 2021–2022, respectively. These reductions could be attributed to extensive removal efforts by the government and local communities. For instance, reports from December 2020 indicate that approximately 80% of the weed's coverage was successfully removed from the lake (Muchye et al., 2022).

The spatial coverage of water hyacinth in Lake Tana typically peaks during the post-rainy season and reaches its minimum at the end of the pre-rainy season (Figure III-2). The peak coverage in the post-rainy season could be attributed to nutrient influx from fertilizer runoff, driven by the expansion of cultivated land in the Tana Basin (Getachew & Manjunatha, 2022; Minale & Belete, 2017; Tewabe & Fentahun, 2020). During the rainy season, fertilizers and nutrients are washed into the lake, providing conditions that promote water hyacinth growth in the subsequent post-rainy season, as the weed requires time to respond to enhanced nutrient availability. This seasonal pattern aligns with findings by Worqlul et al. (2020) and Cai et al. (2023), who also observed high water hyacinth coverage during the post-rainy season. Conversely, the minimum spatial coverage during the pre-rainy and early rainy seasons could be attributed to stakeholder removal efforts, the weed's life cycle, and increased dryness. Changes in leaf color and dryness during the pre-rainy season, as noted by Dersseh et al. (2020), also influence spatial coverage estimates. Similar seasonal patterns have been reported in Lake Tana (Abebe et al., 2023; Dersseh et al., 2020) and other tropical water bodies (Dube et al., 2017; Thamaga & Dube, 2019). However, contrasting findings by Damtie et al. (2021) indicated the highest coverage during the dry season and the lowest during the pre-rainy season in 2019, likely due to differences in management practices, removal efforts, and detection methods. Seasonal patterns revealed a significant decrease in spatial coverage from the post-rainy to the early rainy season, followed by notable growth from the early rainy season to the post-rainy season (Figure III-2). This rapid growth during the post-rainy season highlights the importance of seasonal monitoring for effective

management. Water hyacinth spatial coverage estimates in Lake Tana vary among studies (Anteneh et al., 2015; Asmare et al., 2020; Worqlul et al., 2020; Damtie et al., 2021; Abebe et al., 2023; Dersseh et al., 2020), likely due to differences in satellite resolution, detection criteria, and algorithms used. Nonetheless, this study's findings were mostly consistent with those reported by Dersseh et al. (2020).

The water surface area of Lake Tana was highest between 2020 and 2022 and lowest between 2017 and 2019 (Figure III-2). This variation aligns with the highest recorded rainfall in the lake's surrounding area during 2020–2022 and the lowest rainfall during 2017–2019 (Figure III-4). According to the Mann–Kendall trend test analysis, the spatial coverage of water hyacinth has been increasing significantly, while the lake surface area has shown a non-significant increase. Moreover, a statistically significant positive correlation ($r = 0.49$, $P < 0.05$) was observed between water hyacinth coverage and the lake surface area, indicating that lake expansion promotes water hyacinth growth. When the lake's surface area extends into the surrounding floodplain, it provides ideal conditions for water hyacinth proliferation, particularly in shallow, sedimented, and nutrient-rich waters (Cai et al., 2023; Dersseh et al., 2020).

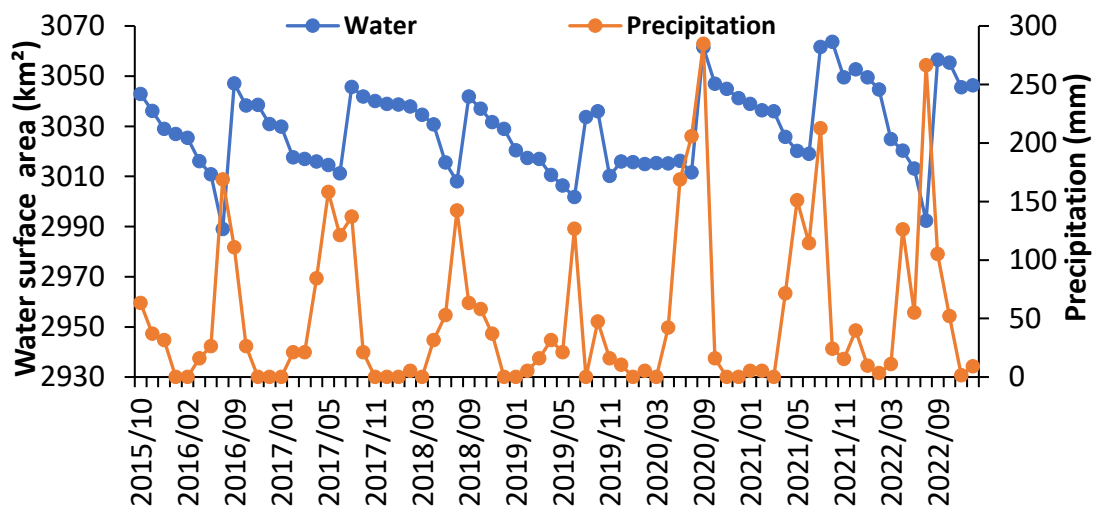


Figure III-4. Time series of water surface area and Precipitation (2015–2022). The rainfall data were downloaded from the NASA/POWER website, available at <https://power.larc.nasa.gov/>

3.4.2. Water hyacinth evapotranspiration and its associated water loss

The water hyacinth evapotranspiration rate showed a significant decreasing trend from October 2015 to December 2023, declining at a rate of 0.114 mm/month ($P < 0.05$). This reduction could be attributed to a concurrent decrease in lake surface water temperature, land surface temperature, and surrounding air temperature (Bayable et al., 2024; Bayable & Alemu, 2022; Figure III-3). Despite this overall decline, evapotranspiration consistently peaks during the pre-rainy season, likely driven by seasonal increases in lake surface water temperature, land surface temperature, and air temperature (Figure III-3).

Interestingly, the decreasing trend in water hyacinth evapotranspiration contradicts the observed increase in total water loss due to water hyacinth from October 2015 to December 2023 (Figure III-5). This apparent contradiction could be attributed to the significant expansion of water hyacinth spatial coverage during the same period (Figure III-2). As spatial coverage increases, the surface area available for evapotranspiration grows, resulting in higher overall water loss. While the evapotranspiration rate per unit area is declining, the extensive coverage provides a larger leaf surface area for transpiration, with dense mats trapping water and enhancing overall evapotranspiration. During the pre-rainy season, high temperatures drive evapotranspiration due to increased energy availability. However, reduced spatial coverage limits total water loss. In contrast, the post-rainy season experiences the highest water loss from water hyacinths, driven by their extensive spatial coverage despite lower temperatures. This larger coverage offers a greater leaf surface area for transpiration, significantly increasing overall evapotranspiration (Abebe et al., 2023; Figure III-2). Moreover, water loss due to water hyacinth exhibits a weak, non-significant positive correlation with lake surface area. This could be because additional water loss is insufficient to affect the lake surface area, meaningfully or the relationship may be diluted by external factors such as hydrological inflows and outflows.

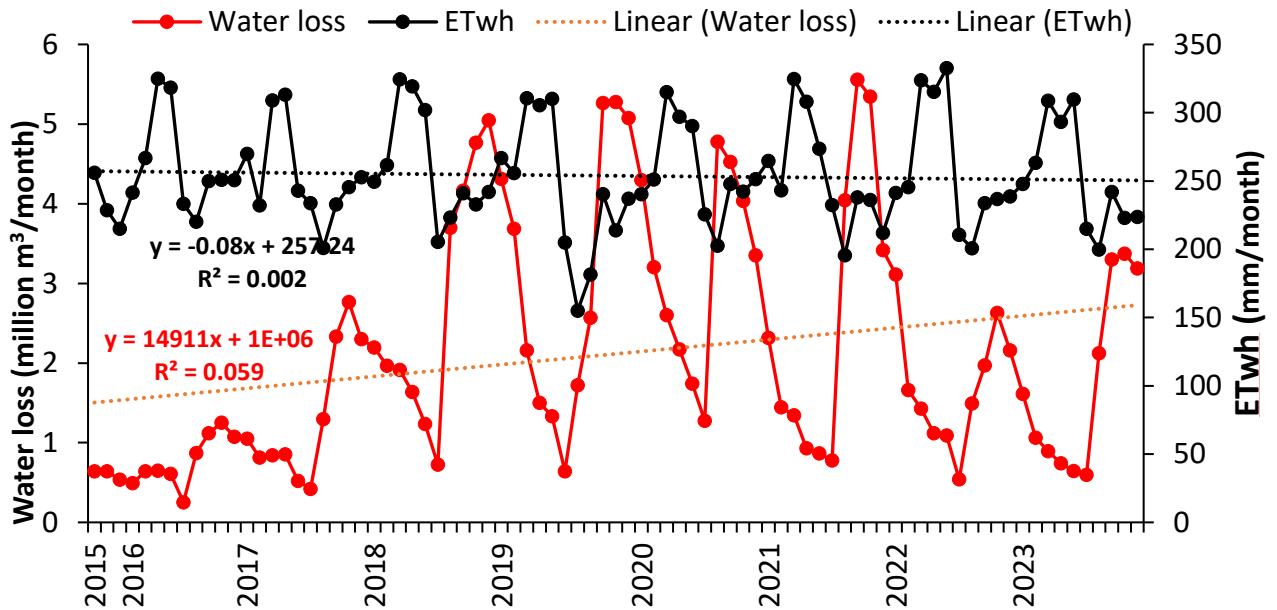


Figure III-5. Time series of water hyacinth evapotranspiration and associated water loss from October 2015 to December 2023.

Currently, water hyacinth covers 0.29% of Lake Tana, resulting in the loss of 176 million m³ of water due to evapotranspiration from October 2015 to December 2023, which represents about 0.61% of the lake's total volume (28.4 billion m³) (Abebe et al., 2023). This water loss accounts for approximately 44.87% of Ethiopia's annual hydropower water consumption (0.4 billion m³/year) (Nurhusein, 2020), 1.96% of irrigation water withdrawal (9 billion m³/year), 25.59% of livestock water use (0.7 billion m³/year), and 21.73% of municipal water use (0.8 billion m³/year) in 2016 (FAO, 2016). If water hyacinth coverage were to increase to 20% of the lake over the same period, water loss could rise to approximately 12.24 billion m³, representing 43.1% of the lake's total volume. Immediate and effective interventions are therefore crucial to prevent the further spread of water hyacinths and to mitigate their severe impacts on the lake's water availability, economic stability, and environmental sustainability.

3.5. CONCLUSION

High water hyacinth populations were concentrated in the northeastern sector of Lake Tana, with significant spatial coverage increases observed between 2015 and 2023. The

annual maximum spatial coverage varied over time, ranging from 2.81 km² in November 2015 to a peak of 24.69 km² in November 2019. Water hyacinth distribution was most extensive during the post-rainy season and minimal during the pre-rainy season. Concurrently, water loss due to water hyacinth evapotranspiration increased significantly, totaling approximately 176 million m³ from October 2015 to December 2023—equivalent to about 0.61% of the lake's total volume. This water loss was most pronounced in the post-rainy season, when the extensive spatial coverage offers a greater leaf surface area for water hyacinth evapotranspiration, and lowest during the pre-rainy season due to reduced coverage. These findings underscore the substantial impact of water hyacinths on Lake Tana's hydrology, including significant water loss and spatial expansion over time. Immediate and targeted management interventions are essential to control water hyacinth proliferation, mitigate water loss, and safeguard the lake's ecological and economic sustainability.

CHAPTER FOUR

4. SPATIOTEMPORAL VARIABILITY OF LAKE SURFACE WATER TEMPERATURE AND WATER QUALITY PARAMETERS AND ITS INTERRELATIONSHIP WITH WATER HYACINTH BIOMASS IN LAKE TANA, ETHIOPIA

4.1. INTRODUCTION

Inland lakes provide critical economic, social, and environmental benefits. However, human activities such as industrialization, urbanization, agriculture, and climate change contribute sediment, nutrients, industrial effluents, and domestic waste into lakes (Danbara, 2014; Das, 2021; Lymburner et al., 2016; Mucheye et al., 2022; Tauchnitz et al., 2020; Tibebe et al., 2019), negatively impacting water quality (Facco et al., 2021). In the Tana sub-basin, increased population growth, climate instability, and lack of integrated watershed management have exacerbated sediment and nutrient loads in Lake Tana (Cai et al., 2023; Mekonnen, 2021). These factors have resulted in higher turbidity and nutrient concentrations, promoting harmful algal blooms and water hyacinth growth (Dersseh et al., 2022; Goshu et al., 2020; Lemma et al., 2018). Water pollution and water hyacinth invasion are currently the most pressing environmental challenges facing Lake Tana (Cai et al., 2023; Dejen et al., 2003; Anteneh et al., 2014; Wondie et al., 2007).

Physical and biological water quality parameters, such as lake surface water temperature (LSWT), turbidity, and chlorophyll-*a* (Chl-*a*), are essential for evaluating the overall health of lakes and their ecosystems. LSWT, an important physical parameter, plays a crucial role in regulating various physical, chemical, and biological processes in aquatic environments (Aguilar-Lome et al., 2021; Crosman & Horel, 2009; Reinart & Reinhold, 2008; Trumpickas et al., 2009; Xiao et al., 2013). It influences lake ecology, biogeochemical processes, water quality, and the metabolism of aquatic organisms (Yang et al., 2022; Yang et al., 2018). Even minor temperature changes can significantly affect aquatic organisms (Alshaikh, 2016). Factors such as global warming, suspended particles, and water hyacinth infestation contribute to LSWT changes in various inland water bodies (Paaijmans et al.,

2008). In addition to LSWT, turbidity and Chl-*a* are critical water quality indicators, particularly in turbid water bodies like Lake Tana (Mucheye et al., 2022). Turbidity serves as an indicator of sedimentation processes (Kayalik & Çorumluoğlu, 2022), while Chl-*a* reflects the lake's nutritional status (Patra et al., 2017). Turbidity measures water transparency and the degree of light obstruction caused by suspended solids, with higher levels, indicating greater particulate matter (Facco et al., 2021; Hossain et al., 2021). It also provides insights into geomorphological and hydrological processes, such as sediment transport, deposition, and re-suspension (Kaba et al., 2014). Chl-*a*, as a biological indicator, is frequently monitored to evaluate the water body's trophic status, which is linked to poor water quality, decreased biodiversity, and ecological instability (Andrade et al., 2019; Masocha et al., 2018; Mazhar et al., 2022). Therefore, assessing and monitoring the spatiotemporal variability of LSWT, turbidity, and Chl-*a*, along with their association with water hyacinth biomass, is critical for effective lake ecosystem management, the development of targeted management strategies, and a comprehensive understanding of the lake's current state.

Conventional water quality measurement techniques at fixed stations are labor-intensive, expensive, time-consuming, and provide limited spatial and temporal coverage (Alcântara et al., 2010; Gholizadeh et al., 2016; Trumpickas et al., 2009). To overcome these challenges, remote sensing satellite imagery is increasingly combined with *in-situ* measurements. Evaluating satellite-derived water quality parameters against on-site measurements is essential to ensure their accuracy and reliability (Gholizadeh et al., 2016). Satellite imagery offers broad area coverage, frequent overpasses, and long-term monitoring capabilities for LSWT and water quality data (Bid & Siddique, 2019; Duan & Bastiaanssen, 2013; Makwinja et al., 2023). Remote sensing data can reliably monitor LSWT, turbidity, and Chl-*a* in large lakes like Lake Tana (Das et al., 2022; Elhag et al., 2019, 2021; Gholizadeh et al., 2016; Mazhar et al., 2022; Xiao et al., 2013). While numerous studies have derived LSWT from various satellite datasets (Chavula et al., 2009; Mushtaq et al., 2021; Wloczyk et al., 2006; Xiao et al., 2013), MODIS stands out as the most suitable option for LSWT estimation in large lakes due to its extensive temporal coverage, high accuracy, and reliability

(Crosman & Horel, 2009; Reinart & Reinhold, 2008; Schneider et al., 2009; Xiao et al., 2013; Xie et al., 2022).

The Sentinel-2 Multi-Spectral Instrument (MSI) provides enhanced accuracy for turbidity and Chl-*a* retrieval in Lake Tana due to its high spatial resolution and wide spectral range in red-edge and NIR wavelengths (Kislik et al., 2022). It is recognized as a leader in algal bloom remote sensing. Turbidity evaluation employs various algorithms, including single-band methods focused on red or NIR bands (Dogliotti et al., 2015; Nechad et al., 2010) and combination methods like the Normalized Difference Turbidity Index (NDTI), which utilizes red-green bands (Garg et al., 2020; Lacaux et al., 2007). Band combinations generally yield more accurate turbidity estimates (Sebastiá-Frasquet et al., 2019).

Similarly, multiple algorithms have been developed to estimate Chl-*a* in turbid waters using red and NIR bands. These are primarily categorized into two-band empirical (Moses et al., 2009; Tzortziou et al., 2007), three-band empirical (Dall’Olmo & Gitelson, 2006), four-band empirical (Le et al., 2009), and three-band semi-analytical (Gons et al., 2002) algorithms. Mishra and Mishra (2012) introduced the Normalized Difference Chlorophyll Index (NDCI), a novel algorithm designed to accurately map Chl-*a* concentrations in turbid, productive waters across diverse geographic regions. Subsequent evaluation of NDCI against other algorithms in various turbid water types and geographic regions demonstrated its superior performance (Mishra & Mishra, 2012). Given their proven effectiveness, NDTI and NDCI derived from Sentinel-2 imagery were used to analyze the spatiotemporal variability of turbidity and Chl-*a* in Lake Tana. However, evaluating NDTI and NDCI using *in-situ* measurements is crucial for different regional applications due to dependencies on local characteristics and variations in spectral reflectance.

In Ethiopia, particularly in Lake Tana, scientific information about physical and biological water quality parameters is spatially limited and temporally fragmented (Cai et al., 2023). Few studies have utilized remote sensing technology to investigate the spatiotemporal variability of LSWT, turbidity, and Chl-*a*. For example, Duan & Bastiaanssen (2013) analyzed monthly LSWT variations from January to December 2006 using MODIS Terra data, while Worqlul et al. (2020) assessed the spatial variability of LSWT and turbidity from

2010 to 2018 using the same satellite imagery. However, neither study validated MODIS-derived results with on-site measurements of water temperature and turbidity. Additionally, these studies were conducted over relatively short temporal scales and did not examine long-term climatological trends in LSWT. Similarly, Moges et al. (2017) estimated and predicted the temporal variability of turbidity, focusing exclusively on the area near the Gumera River's entry from 1999 to 2014 using Landsat-7 imagery. Likewise, Mucheye et al. (2022) analyzed monthly variability in total suspended matter and Chl-*a* concentration using Sentinel-2 imagery and the Case-2 Regional Coast Colour processor (C2RCC) for the year 2020. However, this study also focused on short-term variability and did not validate C2RCC-derived water quality parameters with *in-situ* measurements. Furthermore, the interrelationship between water hyacinth biomass and LSWT, turbidity, and Chl-*a* has not been comprehensively explored in Lake Tana.

Examining spatiotemporal variability of physical and biological water quality parameters across different seasons is essential for effective lake resource management and targeted interventions aimed at improving water quality and lake ecology, particularly in vulnerable regions and during critical seasons. Long-term trend analysis of LSWT provides valuable insights into the lake's thermal behavior, offering significant implications for climate studies and ecosystem modeling. To the best of our knowledge, neither NDTI nor NDCI has previously been applied or validated in Lake Tana for exploring the spatiotemporal variability of turbidity and Chl-*a*. The research questions guiding this investigation were: (1) How did Lake Tana's LSWT vary across different seasons and regions over the long term? (2) What were the spatiotemporal patterns of turbidity and Chl-*a* in Lake Tana across different seasons? (3) How did water hyacinth biomass influence LSWT, turbidity, and Chl-*a*? Accordingly, the objectives of this study were: (1) to analyze the spatiotemporal variability and long-term trends of LSWT, (2) to examine the spatiotemporal dynamics of turbidity and Chl-*a*, and (3) to investigate the interrelationship between water hyacinth biomass and LSWT, turbidity, and Chl-*a* in Lake Tana.

4.2. MATERIALS AND METHODS

4.2.1 Data collection and processing

In-situ water quality data were collected randomly from various parts of the lake, including nearshore areas and the lake center, during two periods: December 6–10, 2022, and May 29–June 9, 2023 (Figure II-1). Water temperature, turbidity, and chlorophyll-*a* (Chl-*a*) concentrations were measured using a portable temperature logger, a Turbidimeter (*LaMotte 2020t/i*), and a Chlorophyll sensor (*KRK Kasahara Chemical Instruments Corp CHL-30N*), respectively. All instruments were calibrated according to the manufacturer's manual instructions before data collection to ensure accurate measurements.

In addition to *in-situ* data, the study utilized MODIS Terra LSWT (2001–2022) and Sentinel-2 Multispectral Instrument (MSI) images (Table IV-1). MODIS Terra LSWT (MOD11A2.061) data, with a 10:30 a.m. overpass time, were selected due to their extended temporal coverage and lower cloud interference compared to the MODIS Aqua (MYD11A2.061) satellite. The MOD11A2.061 product provides global LSWT and emissivity data at a 1 km spatial resolution. Pixels with errors less than one Kelvin (K) were analyzed, as identified by quality control flags (LST Error flag). A mean composite was applied to mitigate the effect of missing values, as recommended by Siddiqui et al. (2021). The MODIS LSWT digital numbers were converted from Kelvin to degrees Celsius by multiplying the input values by a scale factor of 0.02 and subtracting 273.15. Monthly, seasonal, and annual LSWT data within a 500-meter buffer zone of the lake shoreline were analyzed to minimize pixel mixing with other land-use/land-cover (LULC) types and to account for seasonal variations in the lake surface area.

Sentinel-2 MSI imagery was used to estimate turbidity, Chl-*a*, and water hyacinth biomass. With a high spatial resolution of 10–20 m, 5-day revisit intervals, and 13 spectral bands, Sentinel-2 MSI provides valuable data for monitoring environmental parameters (Caballero & Stumpf, 2020). This study utilized Harmonized Sentinel-2 MSI Level-1C data due to its enhanced radiometric and geometric accuracy (Silva & Baptista, 2023). The Harmonized Sentinel-2 MSI Level-1C dataset, available in Google Earth Engine (GEE) under the identifier COPENICUS/S2_HARMONIZED, represents top-of-atmosphere

reflectance from Sentinel-2A (since June 2015) and Sentinel-2B (since March 2017). Since January 25, 2022, Sentinel-2 scenes with a `PROCESSING_BASELINE` of '04.00' or higher have had their digital number (DN) values shifted by 1000. The harmonization process adjusts DN values in newer scenes to match those in older scenes, ensuring temporal consistency for time series analysis (Silva & Baptista, 2023).

Atmospheric correction was conducted using the Satellite Invariant Atmospheric Correction (SIAC) package in GEE, converting top-of-atmosphere reflectance to surface reflectance values. SIAC employs linear transformations and Bayesian statistics to account for aerosol optical thickness and total columnar water vapor, integrating data from the Copernicus Atmospheric Monitoring Service (Yin et al., 2019). The SIAC algorithm's effectiveness has been demonstrated in similar studies, such as Lobo et al. (2021), who reported a strong correlation ($r = 0.96$) between SIAC-derived NDCI from Sentinel-2 Level-1C MSI and the European Space Agency's Surface Reflectance product. Other studies (Carella et al., 2022; Kislik et al., 2022; Silva & Baptista, 2023) have also validated its reliability. Due to the limited temporal coverage of Sentinel-2A surface reflectance data, Harmonized Sentinel-2 Level-1C data (2016–2022) was used after atmospheric correction with SIAC. Cloud masking was applied using the QA60 band in GEE to remove cloud-contaminated pixels. Given the challenges of obtaining completely cloud-free data (0% cloud cover) for most months over Lake Tana, a <5% cloud cover threshold was applied for the dry, pre-rainy, and post-rainy seasons. For the rainy season, characterized by high cloud cover, a more lenient <20% threshold was used. To address data gaps caused by cloud masking, median compositing was employed, filling masked pixels with cloud-free data from nearby dates. This approach ensured a consistent representation of surface conditions and minimized the impact of outliers or erroneous values, allowing for robust time series analysis of physical and biological water quality parameters.

Table IV-1. Summary of satellite data used in the present study

Data Type	Spatial resolution	Time	Data source	Dataset provider in GEE
MOD11A2.061	1km	(2001-2022)	https://lpdaac.usgs.gov/products/mod11a2v061/	NASA LP DAAC at the USGS EROS Center
Harmonized Sentinel-2 MSI	10m, 20m	(2016-2023)	https://earth.esa.int/web/sentinel/user-guides/sentinel-2-msi/product-types/level-1c	European Union/ESA/Copernicus

4.2.2 Water hyacinth biomass and water quality parameter estimation

Water hyacinth biomass: The normalized difference vegetation index (NDVI) from Sentinel-2 imagery was used to estimate water hyacinth biomass (Gerardo & de Lima, 2022; Mucheye et al., 2022). An NDVI threshold of 0.6 (Mucheye et al., 2022) was applied to assess water hyacinth biomass in Lake Tana. NDVI values ranging from 0.6 to 1 were used to determine the distribution of water hyacinth biomass. The areal average NDVI, representing the spatial average of biomass, was calculated to monitor changes in water hyacinth biomass from 2016 to 2022. NDVI was computed using the following equation:

$$\text{NDVI} = (r(835)) - (r(665)) / (r(835) + r(665)) \quad \text{Eq.1}$$

where $r(835)$ (Band 8) and $r(665)$ (Band 4) represent reflectance at near-infrared and red wavelengths, respectively.

Chlorophyll *a* (Chl-*a*): A review of previous studies was conducted to identify the best algorithm for estimating Chl-*a* concentration, considering spatiotemporal conditions and *in-situ* field data (Dall’Olmo & Gitelson, 2006; Gons et al., 2002; Mishra & Mishra, 2012; Moses et al., 2009; Tzortziou et al., 2007). Based on this review, the Normalized Difference Chlorophyll Index (NDCI) was selected for its accuracy and applicability in inland water bodies, especially in regions with limited ground data (Mishra & Mishra, 2011). NDCI, developed by Mishra and Mishra (2011), uses the spectral band difference at 708 nm and 665 nm, normalized by their sum, to minimize uncertainties in remote sensing reflectance and atmospheric contributions. Mishra and Mishra (2011) demonstrated its superior performance in estimating Chl-*a* concentration, with lower RMSE and higher r^2 values compared to other models, including Moses et al. (2009) two-band empirical model, Tzortziou et al. (2007) two-

band empirical model, and Dall'Olmo and Gitelson (2006) three-band empirical model. In this study, the performance of NDCI and other Chl-*a* estimation algorithms (Table IV-2) was evaluated using Sentinel-2-derived raster values and *in-situ* Chl-*a* data from 27 stations in Lake Tana collected between May 29 and June 10, 2023, with a ± 2 -day window. Among the evaluated algorithms, NDCI showed the highest accuracy, achieving an r^2 value of 0.71 (Table IV-2).

Table IIII-2. Evaluation of chlorophyll-*a* estimation algorithms. All correlations between the models and *in-situ* Chl-*a* data (N=27) were significant at $P < 0.05$.

Algorithm	Equation	r	r^2
Moses et al. (2009) two-band empirical model	$M09 = r(704) / r(665)$	0.82	0.67
Tzortziou et al. (2007) two-band empirical model	$T07 = r(665) / r(559)$	0.64	0.41
Dall'Olmo and Gitelson (2006) three-band empirical model	$DO5 = [\frac{1}{r(665)} - \frac{1}{r(704)}] \times r(740)$	0.73	0.53
Normalized Difference Chlorophyll Index (NDCI)	$NDCI = (r(704) - r(665)) / (r(704) + r(665))$	0.84	0.71

Where $r(559)$ (Band 3), $r(665)$ (Band 4), $r(704)$ (Band 5), and $r(740)$ (Band 6) represent reflectance at green, red, red edge 1, and red edge 2 wavelengths of Sentinel-2, respectively. The data in bold indicates the algorithm that performed the best with the highest R^2 value and was used in this study (Table 2). The study modified the algorithm equations (Table IV-2) based on the Sentinel-2 band configuration.

This study used a modified Normalized Difference Chlorophyll Index (NDCI) derived from Sentinel-2 imagery, calculated using the normalized spectral band differences at red edge 1 (704 nm) and red (665 nm) bands (Table IV-2). Several studies have validated the performance of NDCI against *in-situ* Chl-*a* measurements, reporting strong agreement with measured Chl-*a* and demonstrating its applicability across diverse water types (Kislik et al., 2022; Makwinja et al., 2023; Page et al., 2018; Rajendran et al., 2022). NDCI serves as a critical tool for quantifying and monitoring aquatic algae concentrations, with its calculation shown in Table IV-2 (Page et al., 2018; Rajendran et al., 2022).

Turbidity: Literature suggests that single-band algorithms relying on red or NIR bands (Dogliotti et al., 2015; Nechad et al., 2010) often result in overestimation or

underestimation of turbidity (Kuhn et al., 2019; Pahlevan et al., 2019). Moreover, temporal remote sensing data from the same sensor may exhibit radiometric inconsistencies, further diminishing the reliability of single-band approaches (Garg et al., 2020; Pahlevan et al., 2019). Combining spectral bands has been suggested as a more accurate approach than relying solely on single-band algorithms, which are prone to inaccuracies in turbidity estimation (Kuhn et al., 2019; Sebasti  -Frasquet et al., 2019). For example, Worqlul et al. (2020) applied MODIS NIR bands with calibrated coefficients developed by Nechad et al. (2010) to estimate turbidity in Lake Tana, reporting an annual average turbidity of 348 nephelometric turbidity units (NTU), ranging from 193 to 487 NTU. However, these estimates were higher (overestimated) compared to findings from other *in-situ* studies. Womber et al. (2022) reported that Lake Tana's average turbidity remained at 90.8 NTU, even during the turbid season.

The Normalized Difference Turbidity Index (NDTI), derived from red and green bands, has been shown to effectively estimate turbidity levels through statistical analysis (Bid & Siddique, 2019). Numerous studies have consistently reported strong positive correlations between NDTI and measured turbidity across various inland water bodies, confirming its applicability (Bid & Siddique, 2019; Das et al., 2022; Facco et al., 2021; Garg et al., 2017, 2020; Pompapathi et al., 2022). Consequently, this study employed NDTI, derived from Sentinel-2 imagery, for time-series turbidity analysis. NDTI is calculated using the following equation (Lacaux et al., 2007):

$$\text{NDTI} = (r(665)) - (r(560)) / (r(665) + r(560)) \quad \text{Eq.2}$$

where $r(665)$ (Band 4) and $r(560)$ (Band 3) represent the red and green wavelength surface reflectance, respectively.

4.2.3 Validation of MODIS LSWT and Sentinel-2 water quality indices

To evaluate the accuracy of the MODIS LSWT product, daily MODIS Terra LSWT (MOD11A1.061) data were compared with *in-situ* water temperature measurements collected between 8 a.m. and 2 p.m. Although the *in-situ* measurements did not perfectly

align with the MODIS overpass time (~10:30 a.m.), they were used due to limited validation data availability. MODIS LSWT data corresponding to the exact dates of the *in-situ* measurements were utilized. Water temperature data were collected from 38 sampling points in Lake Tana, including 20 points from December 6–10, 2022, and 18 points from May 29–June 9, 2023. Using the 'Extract Values to Points' tool in ArcGIS, MODIS LSWT raster values were first extracted for each sampling location and date. These extracted raster values were then paired with the corresponding *in-situ* measurements for analysis. This dataset was used to evaluate MODIS LSWT accuracy across different times and spatial locations. The evaluation employed metrics such as mean absolute error (MAE), mean absolute percentage error (MAPE), root mean square error (RMSE), mean bias error (MBE), and correlation coefficients (r). Lower error values and higher r values indicate better accuracy. A comparison between MODIS LSWT and *in-situ* measurements revealed a significant positive correlation ($r = 0.90$), with $RMSE = 1.60^{\circ}C$, $MAE = 1.48^{\circ}C$, $MBE = -1.48^{\circ}C$, and $MAPE = 6.25\%$. The negative MBE indicates that MODIS LSWT underestimates lake surface temperature by $1.48^{\circ}C$. Compared to previous studies, the statistical results of this study demonstrate good agreement between MODIS LSWT and *in-situ* measurements. For instance, Xiao et al. (2013) reported $RMSE = 1.46^{\circ}C$ and $r^2 = 0.53$, Song et al. (2016) found $RMSE = 2.80^{\circ}C$, $bias = 1.74^{\circ}C$, and $r^2 = 0.86$, while Zhang et al. (2014) reported $r = 0.89$, $bias = -1.4^{\circ}C$, $MAE = 3.99^{\circ}C$, and $RMSE = 4.53^{\circ}C$. The results of this study ($r = 0.90$) indicate a strong positive correlation, demonstrating the reliability of MODIS LSWT data for Lake Tana (Figure IV-1).

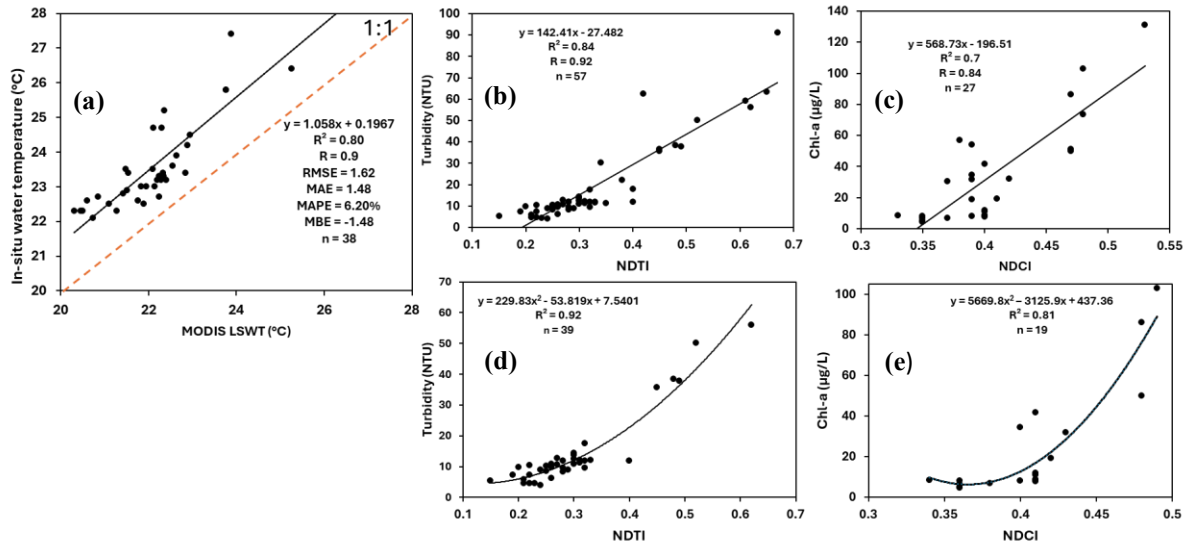


Figure IV-1. Regression analyses include (a) linear regression comparing MODIS Terra LSWT with measured water temperature, (b) linear regression comparing Sentinel-2 NDTI with *in-situ* turbidity, (c) linear regression comparing Sentinel-2 NDCI with *in-situ* Chl-*a*, (d) quadratic polynomial regression comparing Sentinel-2 NDTI with *in-situ* turbidity, and (e) quadratic polynomial regression comparing Sentinel-2 NDCI with *in-situ* Chl-*a*

The study also evaluated Sentinel-2-derived NDTI and NDCI using *in-situ* turbidity and Chl-*a* data, respectively. *In-situ* turbidity data were collected from 57 sampling locations, with 30 samples gathered between December 6–10, 2022, and 27 samples between May 29–June 9, 2023. Similarly, Chl-*a* data were collected from 27 locations from May 29–June 9, 2023, to evaluate Sentinel-2 NDCI. However, due to the five-day temporal resolution of Sentinel-2 images and cloud cover over some stations, some pixels lacked good-quality data, leading to the exclusion of station points within cloud-covered pixels. Consequently, only *in-situ* data collected within a ± 2 -day window of satellite overpasses were used. NDTI and NDCI raster values corresponding to the *in-situ* data were extracted using ArcGIS and evaluated for spatial and temporal consistency. Linear and quadratic polynomial regression models were employed to examine the relationships between spectral indices (NDTI and NDCI) and *in-situ* turbidity and Chl-*a* data, respectively. Significant positive correlations were observed between *in-situ* turbidity and NDTI ($r = 0.92$, $P < 0.05$; Figure IV-1b) and between *in-situ* Chl-*a* and NDCI ($r = 0.84$, $P < 0.05$; Figure IV-1c), confirming the applicability of Sentinel-2 indices for estimating water quality parameters in Lake Tana.

Previous studies also explored the relationship between Chl-*a* and NDCI using a quadratic function, as shown in Eq. 3, which requires calibration for each studied lake by comparing satellite-derived NDCI values with measured Chl-*a* concentrations (Mishra & Mishra, 2012; Makwinja et al., 2023).

$$y = ax^2 + bx + c \quad \text{Eq.3}$$

where the coefficients a, b, and c are determined through data fitting. This study also calibrated and used Eq. 3 to estimate Chl-*a* concentrations in micrograms per liter (µg/L). *In-situ* Chl-*a* concentration data from 19 samples, collected on June 8 and 9, 2023, on the lake using a boat, were compared with corresponding NDCI values derived from Sentinel-2 MSI on June 10, 2023, to establish the quadratic equation (Figure IV-1e). Similarly, *in-situ* turbidity data from 20 sample points collected between December 9 and 11, 2022, and 19 samples collected on June 8 and 9, 2023, also using a boat, were compared with corresponding NDTI values derived from Sentinel-2 MSI imagery on December 7, 2022; December 12, 2022; and June 10, 2023, respectively, to establish the quadratic equation (Figure IV-1d, Eq. 4). Sentinel-2 imagery from June 10, 2023, was subsequently used to estimate per-pixel turbidity and Chl-*a* values using the corresponding quadratic equations (Figure IV-1d; Figure IV-1e; Eq. 4; Eq. 5).

$$\text{Turbidity (NTU)} = 229.83(\text{NDTI})^2 - 53.82 (\text{NDTI}) + 7.54 \quad \text{Eq.4}$$

$$\text{Chl} - a \text{ (}\mu\text{g/L)} = 5669.8(\text{NDCI})^2 - 3125.9 (\text{NDCI}) + 437.36 \quad \text{Eq.5}$$

The accuracy of the quadratic polynomial regression model developed for NDCI was validated using eight sample points obtained by car between May 29 and June 5, 2023. Similarly, the NDTI model was validated using eight sample points obtained by car during the same period, as well as 10 sample points collected on December 6, 2022, using a boat. Validation results revealed significant positive correlations between predicted and measured values, with $r = 0.73$ ($P < 0.05$) for Chl-*a* and $r = 0.78$ ($P < 0.05$) for turbidity. However, due to limitations in acquiring comprehensive *in-situ* data across all months and seasons, the

developed polynomial regression models (Figure IV-1d; Figure IV-1e; Eq. 4; Eq. 5) could only represent one season for Chl-*a* and two seasons for turbidity. As a result, these models may not accurately predict values in other seasons due to variations in environmental conditions. To address this limitation, NDTI and NDCI were employed for time series and trend analyses of turbidity and Chl-*a*, respectively, spanning the period from 2016 to 2022. These indices were selected based on Mishra and Mishra's (2012) recommendation to use NDCI for qualitative Chl-*a* detection in the absence of ground-truth data and the demonstrated effectiveness of NDTI for estimating qualitative turbidity levels under similar constraints (Bid & Siddique, 2019).

4.2.4. Data analysis

In the present study, a pixel-level linear regression model, Modified Mann-Kendall test (MMK), Sen's slope estimator, and Innovative Trend Analysis (ITA) were employed to detect temporal trends in LSWT and water quality time series data. The use of multiple statistical methods aimed to minimize potential errors associated with a single approach and to enhance confidence in trend detection (Lebeza et al., 2023).

The pixel-level linear regression model was applied to examine spatiotemporal changes in LSWT, turbidity, and Chl-*a* trends on a pixel-wise basis. A positive slope indicated upward trends, while a negative slope signified downward trends (Bayable & Alemu, 2022; Bayable & Gashaw, 2021; NourEldeen et al., 2020; Qian et al., 2016). LSWT, Chl-*a*, and turbidity trends were computed using Eq. 6 (NourEldeen et al., 2020):

$$\text{Slope} = \frac{n \times \sum_{i=1}^n y_i \times t_i - (\sum_{i=1}^n y_i)(\sum_{i=1}^n t_i)}{n \times \sum_{i=1}^n t_i^2 - (\sum_{i=1}^n t_i)^2} \quad \text{Eq.6}$$

where y_i refers to LSWT and water quality index in the year i , n refers to the length of time ($n=22$ for LSWT, $n=7$ for water quality index) and t_i refers to an index number 1-22 (2001-2022) for LSWT and 1-7 (2016-2022) for water quality index.

The Modified Mann-Kendall test (MMK) was used to analyze trends in spatially averaged LSWT and water quality indices. MMK is a nonparametric method that adjusts for autocorrelation, making it reliable for environmental variable analysis (Yue & Wang, 2004). It is robust against outliers and is widely used in environmental studies (Lebeza et al., 2023; Yagbasan et al., 2020). The adjusted variance of the Mann-Kendall statistic (s), $v^*(s)$, is calculated using Eq. 7 (Yue & Wang, 2004):

$$v^*(s) = v(s) \cdot \frac{n}{n^*} \quad \text{Eq.7}$$

where, $\frac{n}{n^*}$ is the correlation factor, and $v(s)$ is the variance computed using the original Mann-Kendall method (Mann, 1945; Yue & Wang, 2004). The Sen's slope estimator, a nonparametric approach, was also applied to determine the magnitude of trends (Sen, 1968).

The Innovative Trend Analysis (ITA) method, developed by Şen (2012), was also used to detect trends in LSWT and water quality indices. Researchers widely use it to detect trends in various environmental parameters worldwide (Bouklikha et al., 2020; Danandeh Mehr et al., 2021; Lebeza et al., 2023; Pastagia & Mehta, 2022; Wang et al., 2020). ITA divides historical time-series data into two halves (2001–2011 and 2012–2022), sorts them in ascending order, and plots them against each other on a Cartesian coordinate system. Data points align along a 1:1 (45°) line, with $\pm 5\%$ error lines. Trends are determined by the position of data points relative to the line: points above indicate increasing trends, points below show decreasing trends, and points along the line suggest no trend. Additionally, the trend is categorized into low, medium, or high values by dividing the 1:1 (45°) line. The trend indicator (O) is calculated using Eq. 8:

$$O = \frac{1}{n} \times \sum_{i=1}^n \frac{10(y_i - x_i)}{\bar{x}} \quad \text{Eq.8}$$

where O is the trend indicator, n is the number of observations in each subseries, \bar{x} is the average of the first half subseries data (2001-2011), x_i and y_i are the values of the first and the second subseries (2012-2022) at the i^{th} scatter point, respectively and 10 is the scaling coefficient (Şen 2012).

The inter-annual variability of LSWT for each pixel (2001–2022) was assessed using the coefficient of variation (CV) (Bayable & Alemu, 2022; Gidey et al., 2018), calculated using Eq. 9:

$$CV(\%) = \left(\frac{\mu}{\bar{x}} \right) \times 100 \quad \text{Eq.9}$$

where CV represents the coefficient of variation value for LSWT, μ is the standard deviation of LSWT, and \bar{x} represents the mean of LSWT. Furthermore, to explore the relationships between water hyacinth biomass and LSWT, Chl-*a*, and turbidity, the Pearson correlation coefficient (*r*) was calculated at a significance level of $P < 0.05$. Random sampling points were generated across the study area, and the "extract value to point" tool in ArcGIS was used to extract raster values for mean water quality indices and LSWT (2016–2022) at these locations. These values were then analyzed to assess their interrelationships.

4.3. RESULTS

4.3.1 Spatial distribution of lake surface water temperature

The mean seasonal lake surface water temperature (LSWT) (2001-2022) exhibited spatial variability across all seasons. LSWT ranged from 20.2 to 32°C during the dry season, 21.42 to 38°C in the pre-rainy season, 19.4 to 26°C in the rainy season, and 21.72 to 27.4°C in the post-rainy season. Similarly, the mean annual LSWT for the same period ranged from 20.74 to 31.1°C (Figure IV-2). Among the seasons, the pre-rainy season recorded the highest spatial average LSWT of 22.34°C, while the rainy season had the lowest spatial average of 20.07°C. Spatially, higher LSWT was observed along the shoreline and in the southwestern, southern, and eastern parts of the lake, whereas the central and northern regions consistently experienced lower LSWT across all seasons (Figure IV-2). Overall, shallow areas of the lake tended to have higher LSWT, while deeper regions exhibited lower temperatures (Figure IV-2).

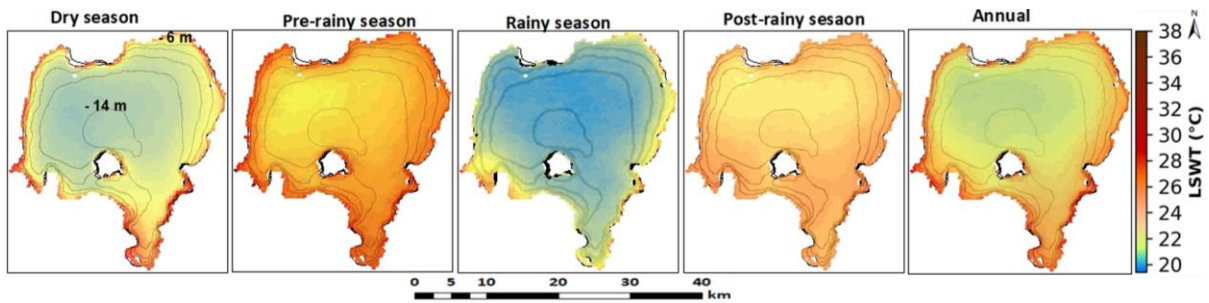


Figure IV-2. Mean seasonal and annual spatial distribution of LSWT derived from MODIS Terra (2001–2022) along depth contours at two-meter (2 m) intervals across the dry season (December–February), pre-rainy season (March–May), rainy season (June–August), and post-rainy season (September–November)

4.3.2 Trend and inter-annual variability analysis of lake surface water temperature

The seasonal spatial LSWT slopes, calculated using a pixel-level linear regression model from 2001 to 2022, varied across the lake. The slopes ranged from -0.08 to 0.07 in the dry season, -0.17 to 0.13 in the pre-rainy season, -0.08 to 0.04 in the rainy season, and -0.06 to 0.04 in the post-rainy season (Figure IV-3). During the dry season, most lake regions showed positive slope values, indicating an increasing trend, except for the western and central areas, which exhibited a decreasing trend. In the pre-rainy and rainy seasons, the eastern, northwestern, and southwestern regions demonstrated positive slopes, suggesting warming trends, while the western, southern, and central parts displayed negative slopes, indicating cooling trends. Similarly, in the post-rainy season, the northeastern, northwestern, and southwestern regions exhibited increasing trends, while the southern, central, and western areas showed decreasing trends. The mean annual spatial LSWT slopes also varied across the lake, ranging from -0.08 to 0.057. Positive trends were observed in the eastern, northwestern, and southwestern regions, whereas the western, southern, and central areas exhibited negative trends (Figure IV-3).

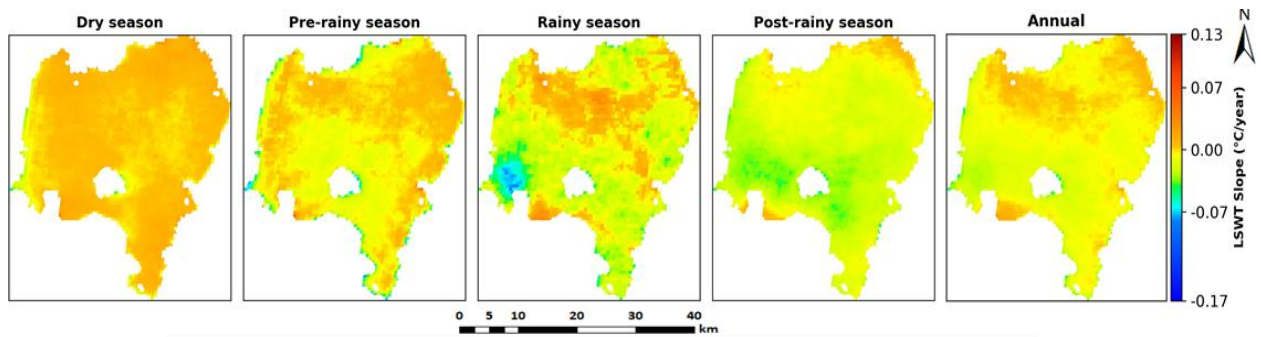


Figure IV-3. Mean seasonal and annual spatial slope of LSWT for Lake Tana (2001-2022) based on a pixel-based linear regression model

Based on the Modified Mann-Kendall trend test analysis, the climatological time series of Lake Tana's spatial average monthly LSWT showed a significant decreasing trend in September, October, February, April, and May. A declining trend was also observed in July, but it was not statistically significant ($P < 0.05$). Conversely, the spatial average LSWT exhibited a significant increasing trend at a rate of $0.014^{\circ}\text{C}/\text{year}$ in December and $0.008^{\circ}\text{C}/\text{year}$ in January over the period (2001–2022). Non-significant increasing trends were observed in November, March, June, and August (Table IV-3). Similarly, the spatial average seasonal LSWT decreased significantly at rates of $0.012^{\circ}\text{C}/\text{year}$, $0.016^{\circ}\text{C}/\text{year}$, and $0.013^{\circ}\text{C}/\text{year}$ during the pre-rainy, rainy, and post-rainy seasons, respectively ($P < 0.05$). In contrast, the spatial average LSWT for the dry season increased at a non-significant rate of $0.001^{\circ}\text{C}/\text{year}$ (Table IV-3 and Figure IV-4). Furthermore, the spatial average annual LSWT for the lake showed a significant decreasing trend at a rate of $0.012^{\circ}\text{C}/\text{year}$ over the same period (Table IV-3 and Figure IV-4).

Table IV-3. The Modified Mann-Kendall trend test analysis of spatial average LSWT (°C) (2001-2022)

Month/Season	Tau	P-value	Trend	Sen's slope (°C/year)
January	0.117	0.023*	Upward	0.008
February	-0.186	0.002*	Downward	-0.015
March	0.048	0.450	Upward	0.009
April	-0.108	0.035*	Downward	-0.010
May	-0.238	0.001*	Downward	-0.022
June	0.022	0.753	Upward	0.003
July	-0.082	0.217	Downward	-0.008
August	0.013	0.906	Upward	0.001
September	-0.238	-0.143	Downward	-0.022
October	-0.273	0.002*	Downward	-0.019
November	0.004	1.000	Upward	0.000
December	0.273	0.000*	Upward	0.014
Dry season	0.030	0.560	Upward	0.001
Pre-rainy season	-0.160	0.004*	Downward	-0.012
Rainy season	-0.143	0.011*	Downward	-0.016
Post-rainy season	-0.307	0.000*	Downward	-0.013
Annual	-0.273	0.000*	Downward	-0.012

*Significant at $P < 0.05$

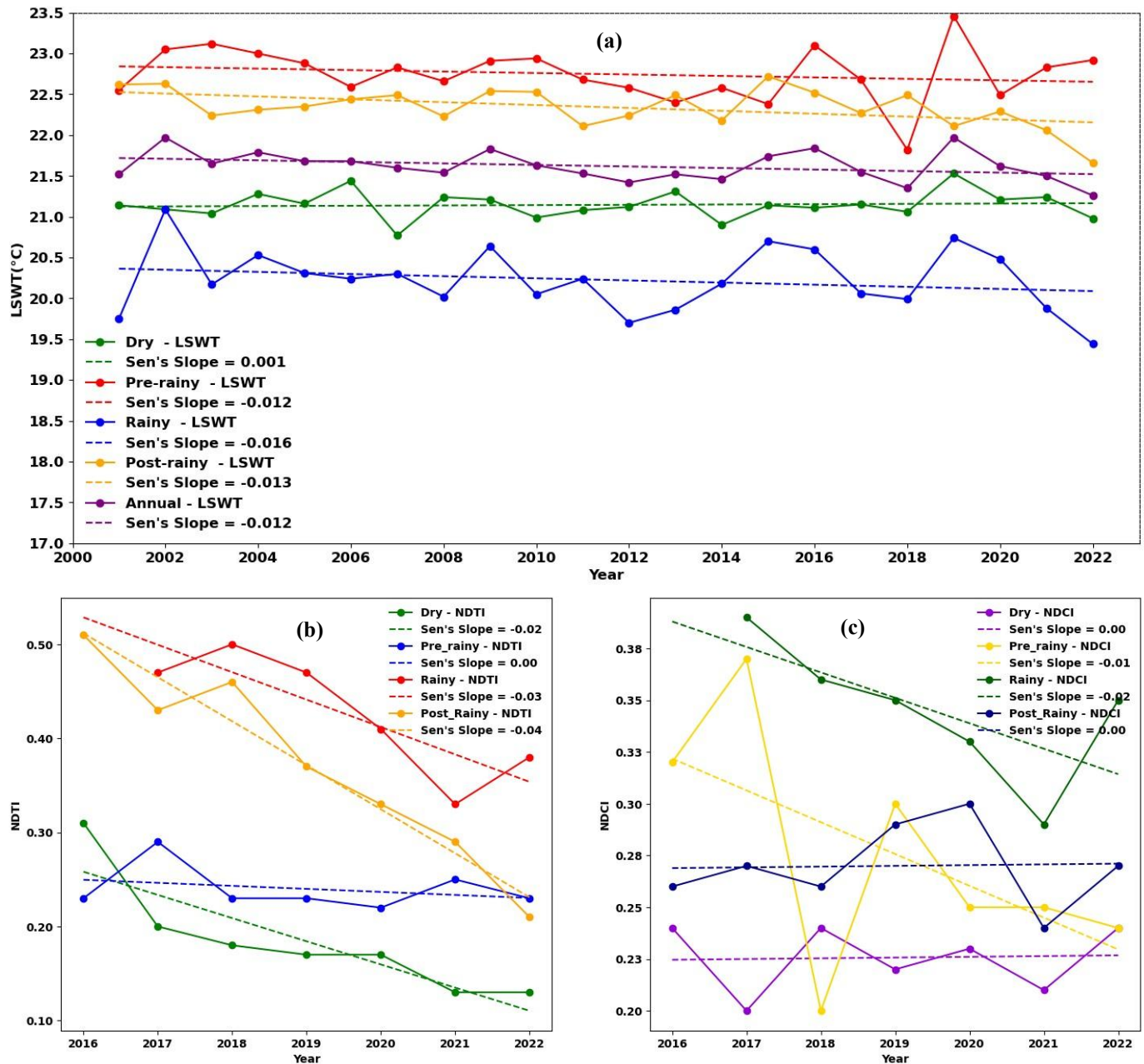


Figure IV-4. Seasonal and annual time series and trends of spatial average (a) LSWT (°C) over two decades (2001-2022), (b) Normalized Difference Turbidity Index (NDTI)-represent turbidity (2016-2022), and (c) Normalized Difference Chlorophyll Index (NDCI)-represent Chl-*a* (2016-2022)

In addition, the mean seasonal and annual spatial average LSWT trends were analyzed using the Innovative Trend Analysis (ITA) method (Figure IV-5). During the pre-rainy, rainy, and post-rainy seasons, most data points fell below the no-trend line (Figure IV-

5), indicating a non-monotonic decreasing trend. The rate of decline was notably higher for lower LSWT values compared to medium and high values during these seasons. Similarly, the annual LSWT data points predominantly fell below the 1:1 line (Figure IV-5), further confirming a non-monotonic decreasing trend. In contrast, during the dry season, nearly all data points aligned with the no-trend line, suggesting no detectable trend.

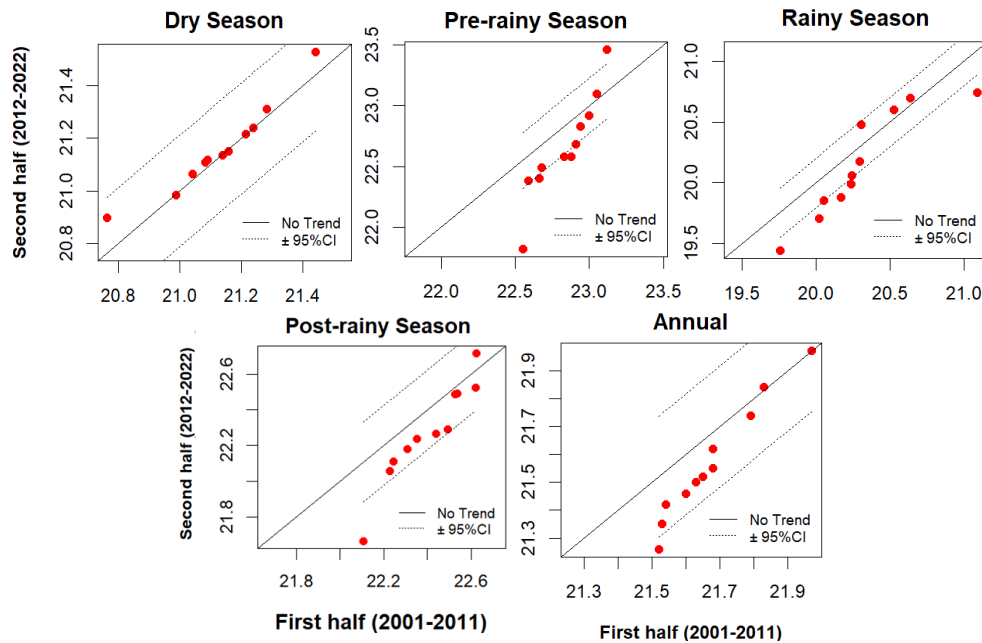


Figure IV-5. Innovative trend analysis of seasonal and annual spatial average LSWT (°C) time series, with the X-axis representing the first half (2001-2011) and the Y-axis representing the second half (2012-2022)

Spatial average seasonal LSWT showed a declining trend during the pre-rainy ($0.009^{\circ}\text{C}/\text{year}$), rainy ($0.013^{\circ}\text{C}/\text{year}$), and post-rainy ($0.018^{\circ}\text{C}/\text{year}$) seasons, while it increased slightly during the dry season ($0.002^{\circ}\text{C}/\text{year}$), as determined by the linear regression model (2001–2022). Similarly, the annual spatial average LSWT decreased at a rate of $0.009^{\circ}\text{C}/\text{year}$ over the same period. Consistently, across all statistical detection methods—pixel-level linear regression model, Modified Mann-Kendall (MMK) trend test, and Innovative Trend Analysis (ITA)—LSWT trends decreased during the pre-rainy, rainy, and post-rainy seasons, and increased during the dry season (Table IV-3; Figures IV-3, IV-4, and IV-5). Overall, the findings of this study revealed a significant downward trend in Lake Tana’s LSWT from January 2001 to December 2022.

Seasonal LSWT exhibited interannual variability across different regions of the lake (Figure IV-6a). During the dry season, the northwestern and western regions showed the highest interannual variability ($CV\% = 1\text{--}2.7\%$), while the southern, southwestern, and southeastern parts exhibited relatively lower variability ($CV\% = 0.5\text{--}1\%$). Similarly, during the pre-rainy season, the western and eastern regions demonstrated high interannual variability ($CV\% = 1.6\text{--}6.4\%$), whereas the southern and northern areas had lower variability ($CV\% = 1\text{--}1.6\%$). In the rainy season, high interannual variability ($CV\% = 2.7\text{--}6.4\%$) was observed in the eastern (near the Gumara and Rib rivers), southwestern (near the Gilgel Abay river), northern (near the Megech river), and northwestern (near Delgi town) parts of the lake, while the western, central, and southern regions exhibited the lowest variability ($CV\% = 1.6\text{--}2\%$). During the post-rainy season, the western and southwestern regions, particularly near the Gilgel Abay river mouth, Tana Belles hydroelectric power plant, and Dek Island, experienced the highest interannual variability in LSWT ($CV\% = 1.3\text{--}2.4\%$), while the northern, northeastern, and eastern regions displayed the lowest variability ($CV\% = 0.5\text{--}1\%$). Among the seasons, the rainy season exhibited the highest overall interannual variability (spatial average $CV\% = 2.47$), whereas the dry season had the lowest variability (spatial average $CV\% = 0.92$) (Figure IV-6a). Furthermore, the seasonal interannual variability of LSWT decreased significantly in all seasons from 2001 to 2022 ($P < 0.05$) (Table IV-4).

Table IV-4. The Modified Mann-Kendall trend test analysis of interannual variability of LSWT (2001-2022)

Month/Season	Tau	P-value	Trend	Sen's Slope (CV%/year)
January	-0.472	0.000*	Downward	-0.045
February	-0.429	0.001*	Downward	-0.057
March	-0.342	0.000*	Downward	-0.044
April	-0.385	0.000*	Downward	-0.071
May	-0.437	0.000*	Downward	-0.130
June	-0.420	0.000*	Downward	-0.089
July	-0.048	0.440	Downward	-0.009
August	0.013	0.879	Upward	0.002
September	-0.082	0.220	Downward	-0.010
October	0.004	1.000	Upward	0.001
November	-0.394	0.000*	Downward	-0.032
December	-0.481	0.000*	Downward	-0.051
Post-rainy season	-0.186	0.035*	Downward	-0.011
Dry season	-0.455	0.000*	Downward	-0.051
Pre-rainy season	-0.515	0.000*	Downward	-0.074
Rainy season	-0.290	0.000*	Downward	-0.039

*Significant at $P < 0.05$

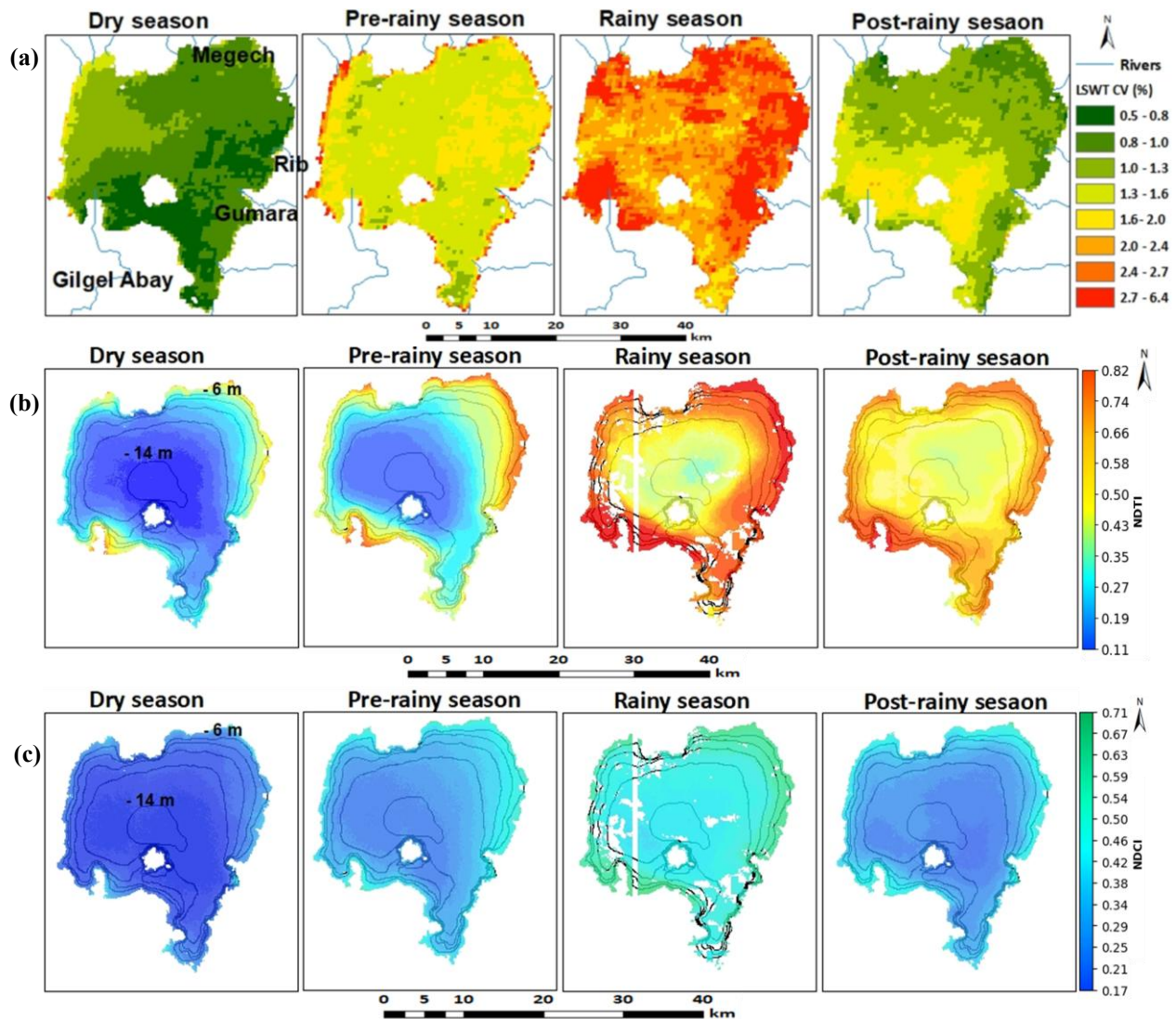


Figure IV-6. (a) Interannual variability of LSWT based on the coefficient of variation (CV%) (2001–2022); (b) mean seasonal spatial distribution of the Normalized Difference Turbidity Index (NDTI, representing turbidity levels) with two-meter (2 m) interval depth contours; and (c) mean seasonal spatial distribution of the Normalized Difference Chlorophyll Index (NDCI, representing Chl-*a* concentration) with two-meter (2 m) interval depth contours (2016–2022)

4.3.3 Spatial distribution of turbidity and chlorophyll *a* (Chl-*a*) indices

The spatial distribution of the normalized difference turbidity index (NDTI) from 2016 to 2022 (Figure IV-6b) indicated that the northern, eastern, and southwestern regions of the lake exhibited the highest turbidity levels (reflected by the highest NDTI values), while

the central parts consistently showed the lowest turbidity levels across all seasons. Similarly, the northeastern, eastern, and southwestern regions exhibited the highest Chl-*a* concentrations, as indicated by the highest normalized difference chlorophyll index (NDCI) values, whereas the central areas displayed the lowest concentrations (Figure IV-6c). Shallow regions of the lake generally had elevated turbidity and Chl-*a* concentrations, while deeper areas exhibited lower values. The highest turbidity levels and Chl-*a* concentrations occurred during the rainy season, while the lowest levels were observed during the dry season (Figures IV-6b and IV-6c). Predicted turbidity levels for June 2023 also displayed high spatial variability, ranging from 4.35 to 81.60 NTU, with the northeastern, eastern, and southwestern regions showing the highest levels, while the central, western, and southern parts had lower turbidity values (Figure IV-7a). Similarly, predicted Chl-*a* concentrations for June 2023 ranged from 6.50 to 150.20 $\mu\text{g/L}$, with the northwestern, northeastern, eastern, and southwestern regions exhibiting the highest concentrations, and the central, western, and southern areas showing lower concentrations (Figure IV-7b).

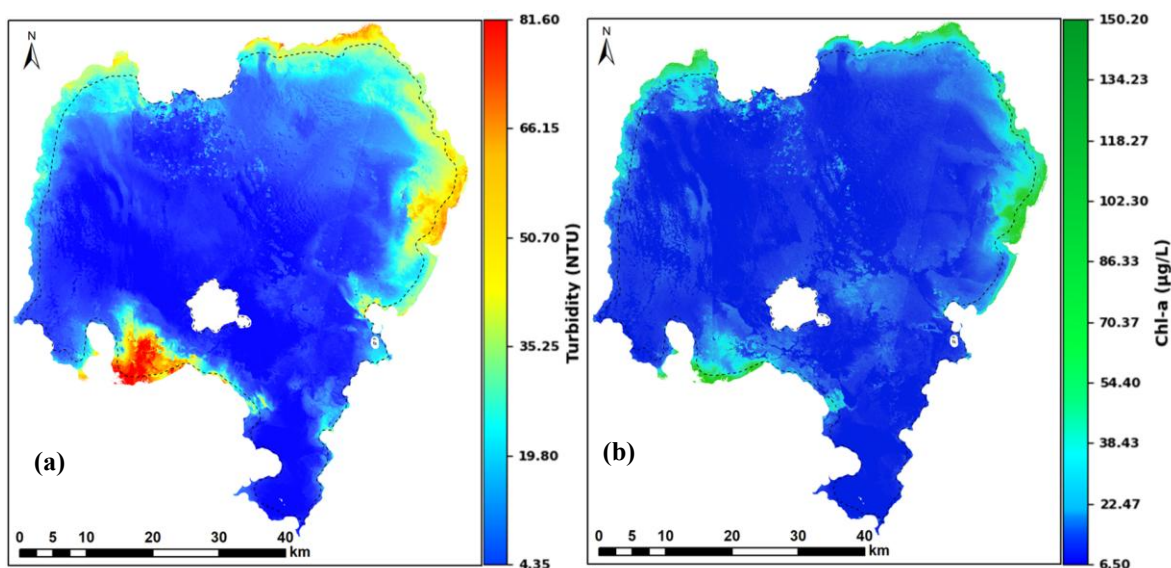


Figure IV-7. Predicted (a) turbidity and (b) Chl-*a* concentrations of Lake Tana (June 2023). The overlaid black dotted lines on the maps indicate depth contours at 5 meters.

4.3.4 Temporal variability analysis of turbidity and Chl-*a* indices

Trends in turbidity and Chl-*a* concentrations were analyzed using the spatial slopes of the normalized difference turbidity index (NDTI) and normalized difference chlorophyll

index (NDCI) from 2016 to 2022, derived from a pixel-based linear regression model (Figure IV-8). The NDTI slopes varied across seasons and regions. During the dry and post-rainy seasons, negative NDTI slopes indicated a declining trend in turbidity in the central, western, and northern areas. In contrast, the shore areas, as well as the southern and eastern regions, exhibited positive NDTI slopes, reflecting an increasing trend in turbidity during the dry season. In the pre-rainy season, turbidity decreased in the western and northern areas, as shown by negative NDTI slopes, while positive slopes in the southwestern, southern, eastern, and northwestern regions indicated an increasing trend, particularly near major river mouths and towns (Figure IV-8). Overall, the spatial slope of NDTI was highest in the pre-rainy season and lowest in the post-rainy season (Figure IV-8). Similarly, the spatial slopes of NDCI varied across seasons and regions (Figure IV-8). During the dry season, negative NDCI slopes along the shorelines indicated a declining trend in Chl-*a* concentrations, while positive slopes in the central regions reflected an increasing trend. In the pre-rainy season, negative slopes indicated a decrease in Chl-*a* concentrations in the northwestern, northern, and northeastern areas, whereas positive slopes reflected an increase in the southern and central regions. During the post-rainy season, Chl-*a* concentrations declined in the western and central areas, particularly near the Tana Belles hydroelectric power plant, while increasing in the northern, eastern, and southern parts of the lake.

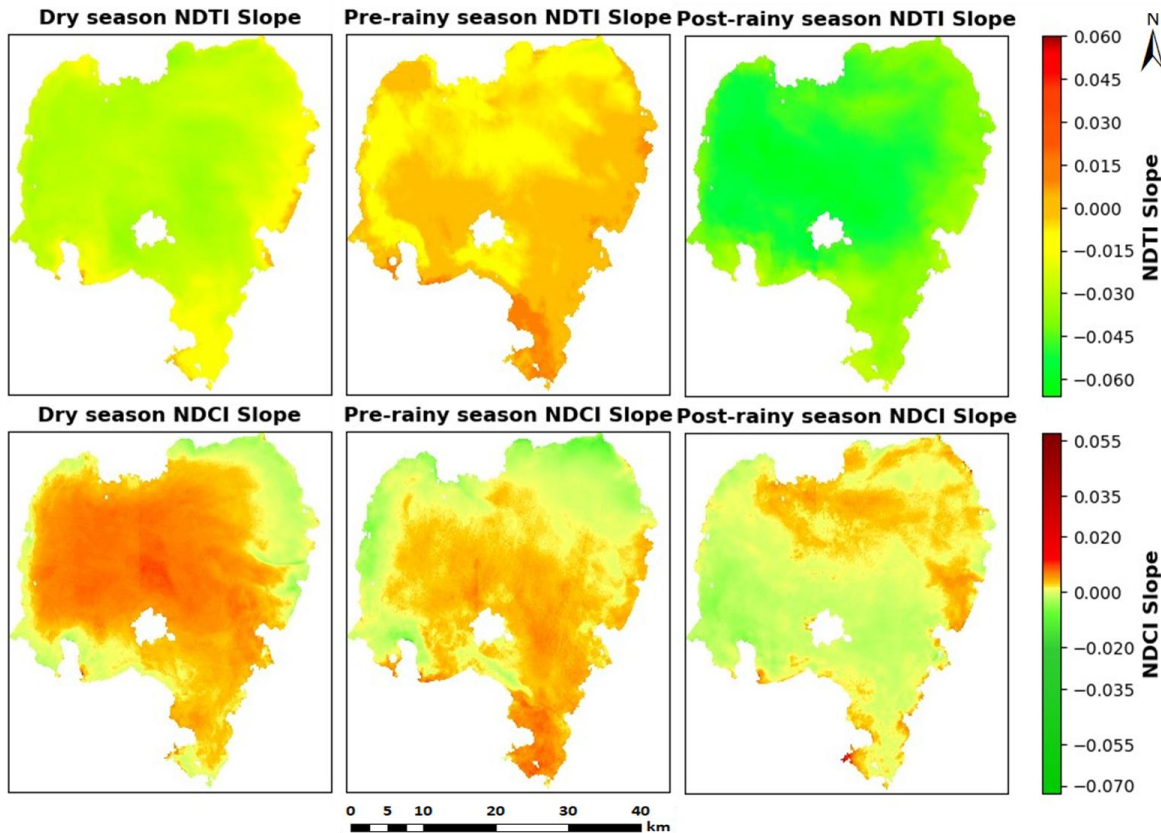


Figure IV-8. Seasonal spatial slopes of NDTI and NDCI based on a pixel-based linear regression model (2016-2022). Note: The spatial slopes of turbidity and Chl-*a* in the rainy season were not estimated due to extensive cloud coverage and missing spatial data. However, temporal variability during the rainy season was analyzed using the spatial average of available pixel values.

The time series and trends of spatial average turbidity and Chl-*a* index (2016–2022) across different seasons are presented in Figure IV-4. According to the Modified Mann-Kendall trend test analysis, the seasonal spatial average NDTI, representing turbidity levels, showed significant decreasing trends during the dry, rainy, and post-rainy seasons. In contrast, the pre-rainy season exhibited a non-significant decreasing trend (2016–2022, $P < 0.05$) (Figure IV-4b). Similarly, the spatial average NDCI, representing Chl-*a* concentrations, demonstrated a significant decreasing trend during the pre-rainy and rainy seasons. Conversely, non-significant increasing trends were observed during the dry and post-rainy seasons (Figure IV-4c). Overall, trends in the spatial average turbidity and Chl-*a* index varied by season but exhibited an overall decline from January 2016 to February 2023.

4.3.5 Interrelationship between water hyacinth biomass and LSWT, turbidity, and Chl-*a*

The correlation between the spatial average NDVI, representing water hyacinth biomass, and mean LSWT in the northeastern region (near water hyacinth-infested areas) was positive ($r = 0.18$) but statistically non-significant. In contrast, the correlation between spatial average water hyacinth biomass and both the mean NDTI (representing turbidity levels) and NDCI (representing Chl-*a* concentration) in the northeastern parts of the lake (2016–2022) was negative, with statistically significant r values of -0.33 and -0.35, respectively (Table IV-5).

This study also revealed a positive correlation between LSWT and both the turbidity index and the Chl-*a* index across all seasons, with varying strengths. The correlation (r) between LSWT and the turbidity index was statistically significant, with r values of 0.53, 0.51, 0.78, and 0.74 during the dry, pre-rainy, rainy, and post-rainy seasons, respectively. Similarly, the correlation between LSWT and the Chl-*a* index was significant and varied by season, with r values of 0.54, 0.53, 0.74, and 0.58 in the dry, pre-rainy, rainy, and post-rainy seasons, respectively. Additionally, the correlation between NDTI and NDCI was strongly positive, with r values of 0.93, 0.97, 0.91, and 0.75 during the dry, pre-rainy, rainy, and post-rainy seasons, respectively.

Table IV-5. Correlation between spatially averaged water hyacinth biomass and mean LSWT, turbidity, and Chl-*a* index in the northeastern region of Lake Tana near water hyacinth-infested areas (January 2016 – December 2022)

Correlation	r	P	r^2
Water hyacinth biomass vs LSWT	0.18	0.12	0.03
Water hyacinth biomass vs Turbidity index	-0.33	0.00*	0.11
Water hyacinth biomass vs Chl- <i>a</i> index	-0.35	0.00*	0.12

*Significant at $P < 0.05$

4.4. DISCUSSION

4.4.1 Spatiotemporal variability analysis of lake surface water temperature

The lake surface water temperature (LSWT) of Lake Tana varies spatially and seasonally and is negatively correlated with depth (Figure IV-2). Under certain weather and climatic conditions, lake depth becomes the dominant factor influencing LSWT variation (Balsamo et al., 2010). Similarly, Xiao et al. (2013) reported a significant correlation between LSWT and lake depth in Qinghai Lake, where shallow areas exhibited faster warming during periods of temperature increases. The spatial variability of LSWT in Lake Tana could also be associated with the spatial distribution of turbidity. The present study reported a significant positive correlation between LSWT and turbidity across all seasons. A similar relationship was reported by Mushtaq et al. (2021) in a Himalayan Lake, which revealed a strong correlation between LSWT and turbidity. Paaijmans et al. (2008) also reported that higher turbidity could increase surface water temperature due to suspended particles absorbing and retaining heat. In Lake Tana, LSWT was highest in nearshore areas and in the northeastern, eastern, southern, and southwestern parts of the lake across all seasons. This could be attributed to the shallow depth and elevated turbidity in these regions. Conversely, LSWT was lowest in the central parts of the lake, which could be due to greater depths resulting in slower warming rates caused by higher thermal inertia (Iestyn Woolway & Merchant, 2017) and lower turbidity levels (Figure IV-6b).

The LSWT demonstrated a consistent warming trend in the northeastern parts of Lake Tana across all seasons (Figure IV-3). This trend could be linked to the spread and dense surface mats of water hyacinth in this region (Figure IV-9). Over the past 10 years, the spatial coverage of water hyacinths has increased from almost none to 25 km² in the lake (Dersseh et al., 2020, 2022; Figure III-2). Water hyacinth surface mats can influence water temperature by reducing water movement, thereby increasing lake water residence time, which leads to higher water temperatures (Tobias et al., 2019). The positive correlation ($r = 0.18$) between spatially averaged water hyacinth biomass and mean LSWT (Table IV-5), along with the observed increasing LSWT trend in water hyacinth-infested areas (Figure IV-3), suggests

that water hyacinth could contribute to localized LSWT increases by extending water residence time. Water hyacinth's dense surface mats can cause stagnant water, leading to prolonged residence time and elevated temperatures. Additionally, organic matter decomposition within these mats generates heat, further contributing to temperature increases (IvyPanda, 2019). The presence of dense water hyacinth mats in the northeastern regions (Mucheye et al., 2022; Bayable et al., 2023) could suggest localized surface water warming. This warming effect could also be exacerbated by the transport of warm water from water hyacinth-covered areas to surrounding regions via water currents or wind. Conversely, LSWT showed a decreasing trend (2001–2022) in the western region near the Tana Belles hydroelectric power plant (Figure IV-3), which was completed in 2010 and became fully operational in 2012 (Nurhusein, 2020). This decreasing temperature trend could be attributed to cold-water mixing caused by the outflow from Lake Tana to the hydroelectric power plant. The increased mixing of cold water likely lowers the temperature in this region. Nevertheless, further investigations are required to fully understand these trends and the specific underlying mechanisms driving LSWT variability in Lake Tana.

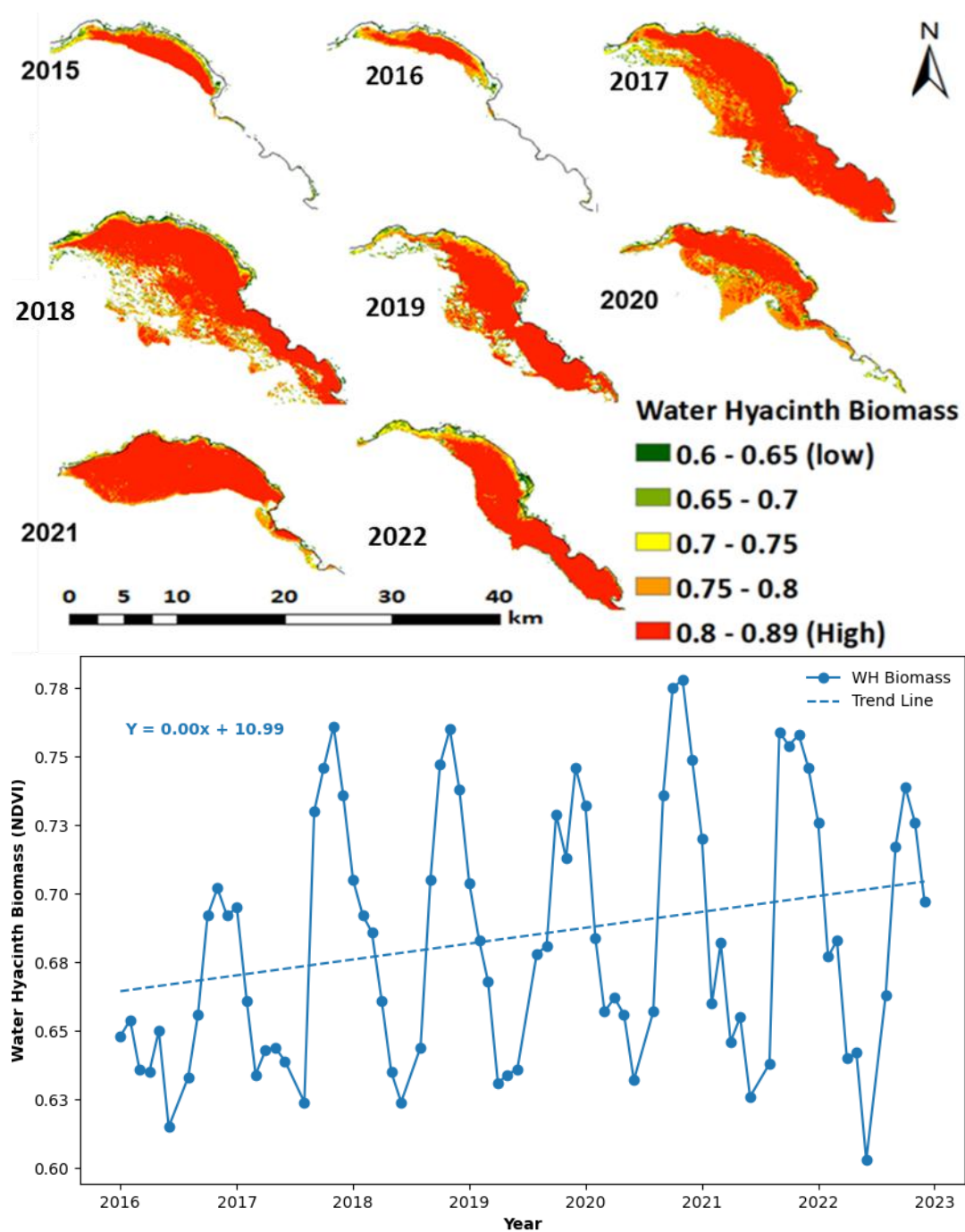


Figure IV-9. Spatial distribution of water hyacinth biomass (WH) in the post-rainy season (2015–2022) in the northeastern part of Lake Tana, along with a time series graph showing WH biomass trends from 2016 to 2022. Biomass was estimated using Sentinel-2 satellite imagery with an NDVI threshold range of 0.6–1.

The spatial average LSWT for the entire lake exhibited significant decreasing trends at rates of 0.012°C/year, 0.016°C/year, 0.013°C/year, and 0.012°C/year during the pre-rainy, rainy, post-rainy seasons, and annually, respectively, from 2001 to 2022, as determined by the Modified Mann-Kendall trend test (Figure IV-4a and Table IV-3). Notably, no significant trend was observed during the dry season. This decreasing trend could be associated with regional climatic conditions. Previous studies have reported moderate to strong positive correlations between air temperature and LSWT in inland lakes (Kaushal et al., 2010; Wang et al., 2023; Yang et al., 2019, 2020). Similarly, the present study also reported a positive correlation between mean LSWT and mean air temperature across all seasons, though with varying strengths (Bayable et al., 2024). The mean annual air temperature in the lake area exhibited a decreasing trend from 2001 to 2021 (Figure IV-10a), which could be attributed to Ethiopia's green development initiatives and the resulting increase in vegetation cover (Jallela, 2021). Supporting this, Bayable and Alemu (2022) reported a downward trend in land surface temperature (LST) in the surrounding area from 2001 to 2020, linking it to forest and vegetation cover expansion (Jallela, 2021; Getachew & Manjunatha, 2022). At a larger scale, this study investigated the potential influence of global climatic drivers, such as sea surface temperature anomalies (SSTA), on LSWT variability in Lake Tana. Correlation analysis revealed no significant relationships ($P < 0.05$) between Lake Surface Water Temperature Anomaly (LSWTA) and SSTA in the Indian Ocean Dipole Mode Index (DMI), Eastern Indian Ocean Index (EIN), Western Indian Ocean Index (WIN), North Atlantic Ocean (NATL), and South Atlantic Ocean (SATL) (Bayable et al., 2024). Conversely, significant positive correlations were observed between the LSWTA of Lake Tana and the Global Tropics Sea Surface Temperature Anomalies (GTSSTA) ($r = 0.43$), as well as the Pacific Ocean Niño 3.4 SSTA ($r = 0.52$) (Figure IV-10b). These findings suggest that the Pacific Ocean SSTA in the Niño 3.4 region and GTSSTA are potential drivers influencing LSWT variability in Lake Tana. In contrast, the lack of significant correlations with Indian and Atlantic Ocean SSTAs led to their exclusion as influential factors. Additionally, the Pacific Ocean Niño 3.4 SSTA exhibited a decreasing trend from 2001 to 2022 (Figure IV-10b). Therefore, the observed decreasing trends in the LSWT of Lake Tana could be

associated with a combination of declining air temperature, land surface temperature, and Pacific Ocean SST.

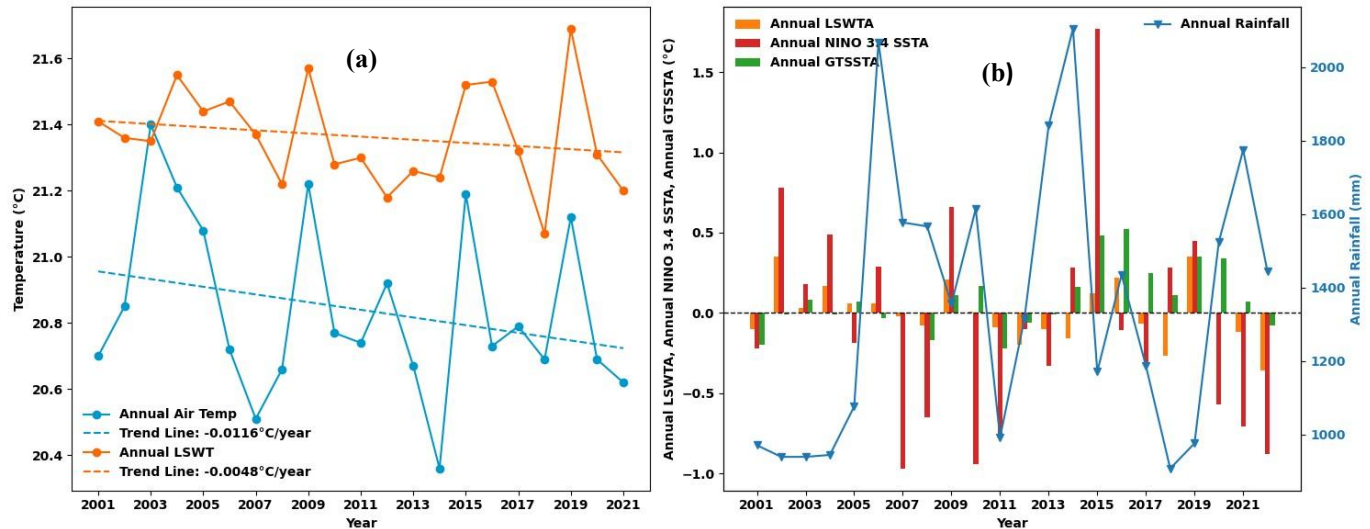


Figure IV-10. (a) Time series of LSWT and air temperature (2001–2021), showing a positive and statistically significant correlation ($r = 0.56$, $P < 0.05$) between mean annual LSWT and air temperature. Air temperature (at 2 m above the surface) and rainfall data were sourced from NASA's MERRA-2 and downloaded via NASA/POWER (<https://power.larc.nasa.gov/>) and (b) Time series of Lake Surface Water Temperature Anomaly (LSWTA), Pacific Ocean Sea Surface Temperature Anomaly (SSTA) in the Niño 3.4 region, and Global Tropics SSTA (GTSSTA) (2001–2022). A positive and statistically significant correlation was found between LSWTA and Niño 3.4 SSTA ($r = 0.52$) and between LSWTA and GTSSTA ($r = 0.43$, $P < 0.05$). Pacific Ocean SSTA and GTSSTA data were obtained from NOAA's Climate Prediction Center (<https://www.cpc.ncep.noaa.gov/data/indices/>)

4.4.2 Spatiotemporal variability analysis of turbidity and Chl-*a*

The turbidity index of Lake Tana varies spatially, with the highest values in the northeastern, eastern, and southwestern regions, and the lowest values in the central areas across all seasons. Predicted turbidity in June 2023 also showed high spatial variability, with elevated levels in the northeastern, eastern, and southwestern regions, while the central, western, and southern areas exhibited relatively lower turbidity (Figure IV-7a). This spatial variability could be associated with the phytoplankton community, as turbidity shows a strong positive correlation with the Chl-*a* index ($r = 0.75$ – 0.97). A similar relationship was reported by Fadel et al. (2016) in the Karaoun Reservoir, highlighting the role of phytoplankton in turbidity. Higher turbidity in the lake's shallow areas (Figure IV-6b) could

also result from sediment resuspension caused by current flow (Facco et al., 2021; Yu et al., 2014). The highest turbidity levels were observed near the Gilgel Abay River mouth in the southwestern region, likely due to significant sediment accumulation in this area (Kebedew et al., 2021). Sediment accumulation increases suspended particles and fine materials in the water, thereby raising turbidity levels. Seasonally, turbidity is highest during the rainy season and lowest during the dry season (Figure IV-6b). This pattern could be attributed to increased rainfall and sediment runoff during the rainy season, as tributaries like the Gilgel Abay, Gumara, Rib, and Megech rivers transport sediment from the catchment area into the lake. In contrast, minimal rainfall and sediment runoff during the dry season result in reduced turbidity (Kaba et al., 2014; Mucheye et al., 2022). These seasonal patterns align with findings in other water bodies, such as the Panchet Hill Dam in India (Bid and Siddique, 2019) and the Itaipu Reservoir in Brazil (Facco et al., 2021), where turbidity increases during the rainy season due to sediment inflow and decreases in the dry season with reduced precipitation. Predicted turbidity in Lake Tana in June 2023 ranged from 4.35 to 81.60 NTU, with a spatial mean of 12.24 NTU. However, these values significantly exceed WHO guidelines, which recommend turbidity levels below 1 NTU before disinfection and up to 5 NTU in developing countries (Matos et al., 2024). This highlights concerns about water quality in Lake Tana and underscores the urgent need for effective management strategies.

Chl-*a* concentrations in Lake Tana exhibit significant spatial and seasonal variability (Figure IV-6c). Higher concentrations were observed in the northwestern, northeastern, eastern, and southwestern regions, while the central and western regions consistently showed lower concentrations across all seasons. Similarly, estimated Chl-*a* levels for June 2023 revealed high variability, with elevated concentrations in the northwestern, northeastern, eastern, and southwestern areas and lower values in the central, western, and southern regions (Figure IV-7b). This spatial variability could be attributed to elevated nutrient concentrations in the northwestern, northeastern, eastern, and southwestern regions, particularly near the Gilgel Abay River mouth (Dersseh et al., 2019, 2020; Cai et al., 2023). *In-situ* measurements of total nitrogen and total phosphorus collected in December 2022 and June 2023 confirmed elevated nutrient levels in these regions, likely facilitating phytoplankton growth and

contributing to higher Chl-*a* concentrations. High turbidity and Chl-*a* values in the northern and eastern sections could also result from lake bottom reflectance in optically shallow areas (Figure IV-7), which influences water quality estimation using remote sensing data (Zhang et al., 2018). However, further investigation is needed to distinguish the individual contributions of lake bottom reflectance, elevated nutrient concentrations (Dersseh et al., 2019, 2020; Cai et al., 2023), and sediment resuspension caused by water currents (Facco et al., 2021; Yu et al., 2014), particularly given their concurrent presence in these regions.

Spatial variability in Chl-*a* concentrations could further be influenced by local climatic characteristics. This study demonstrated a positive correlation between LSWT and the Chl-*a* index, with *r* values ranging from 0.53 to 0.74 across seasons. Areas with higher LSWT corresponded to elevated NDCI values, indicating increased Chl-*a* concentrations, while cooler regions showed lower Chl-*a* values (Figure IV-2 and Figure IV-6c). Warmer LSWT reduces water mixing, enabling algae to grow thicker and float to the surface more quickly (EPA, 2023). Additionally, warmer water enhances the light-harvesting capacity of phytoplankton, promoting biomass production (Fernández-González et al., 2022). These findings align with previous studies, such as Mucheye et al. (2022), which reported the highest Chl-*a* concentrations in the northeastern and eastern regions of Lake Tana. Similar positive correlations between LSWT and Chl-*a* have been reported in other lakes, where surface water warming extends the thermal stratification period, reducing light constraints and enhancing phytoplankton growth (Aitelghazi et al., 2019; Kayalik & Çorumluoğlu, 2022; Makwinja et al., 2023).

Lake Tana is nutrient-limited during the dry season but receives substantial nutrient and sediment influx during the rainy season (Wondie et al., 2007). This nutrient input promotes phytoplankton growth during the rainy season, whereas nutrient limitations reduce growth in the subsequent dry season. The findings of this study align with Mucheye et al. (2022), who reported the highest Chl-*a* concentrations during the rainy season and the lowest during the dry season. During the dry and pre-rainy seasons, Chl-*a* concentrations showed a declining trend along the lake's shoreline (Figure IV-8). This could be attributed to the expansion of water hyacinth (Dersseh et al., 2022) and submerged macrophytes like Illinois

Pondweed. Water hyacinth blocks light and absorbs nutrients, reducing phytoplankton abundance (Villamagna & Murphy, 2010; Oliveira-Junior et al., 2018; Ting et al., 2018). Submerged macrophytes further inhibit phytoplankton productivity through competition for resources (Takamura et al., 2003). The combined effects of nutrient uptake by water hyacinth and the inhibitory actions of macrophytes likely explain the declining Chl-*a* trend along the shoreline. Similar findings were reported by Mirona et al. (2011), who revealed low Chl-*a* concentrations in water hyacinth-infested areas of Lake Naivasha, Kenya. In contrast, Chl-*a* concentrations increased in the central lake during the dry season (Figure IV-8), possibly due to the decomposition of water hyacinth and other aquatic vegetation, which releases nitrogen and phosphorus (Xie et al., 2004), along with the expansion of water hyacinth (Dersseh et al., 2020; 2022). Lake circulation patterns, driven by wind-induced surface currents and temperature/density gradients, could transport these nutrients from the shoreline to the lake center, enhancing conditions for phytoplankton growth (Kebedew et al., 2023).

In the post-rainy season, Chl-*a* concentrations increased in the northern, northeastern, eastern, and southern regions (2016–2022; Figure IV-8), likely due to nutrient runoff from expanding cultivated lands in the surrounding areas (Minale & Belete, 2017; Tewabe & Fentahun, 2020; Getachew & Manjunatha, 2022). Nutrients introduced during the rainy season, mainly through fertilizer runoff, could promote phytoplankton growth in the post-rainy season, as it takes time for algae to respond to the enhanced nutrient availability. Conversely, the Chl-*a* trend decreased in the western region near the Tana Belles hydroelectric power plant during the post-rainy season. This decline could be linked to water discharge from Lake Tana, which reduces water residence time and limits phytoplankton growth. Extended residence time facilitates phytoplankton-nutrient interactions, enhancing Chl-*a* concentrations (Lee et al., 2012; Gomes & Miranda, 2001). Therefore, the observed decline in Chl-*a* in the western region could be attributed to higher discharge rates associated with the Tana Belles hydroelectric power plant.

Studies have established Chl-*a* thresholds that indicate water quality degradation and health risks. Concentrations above 30 µg/L increase the risk of algal-related health issues (Heath et al., 1998), while taste and odor problems occur at 9–10 µg/L, worsening at 15–20

µg/L (Carney, 1998). Chorus and Bartram (1999) reported moderate health risks at 50 µg/L, particularly with cyanobacteria, while Smith et al. (2002) recommended maintaining Chl-*a* below 15 µg/L to avoid such issues. In Lake Tana, predicted Chl-*a* levels range from 6.50 to 150.20 µg/L, with a spatial mean of 19.04 µg/L, suggesting potential health risks, especially in the northeastern and eastern regions. This also highlights concerns about water quality in Lake Tana and underscores the urgent need for effective management strategies.

The overall trend of spatial average turbidity and Chl-*a* concentrations in Lake Tana declined between January 2016 and February 2023. This decline could be linked to the expansion of water hyacinth and other aquatic vegetation along the shoreline, as indicated by the negative correlation between water hyacinth biomass and turbidity ($r = -0.33$) and Chl-*a* concentrations ($r = -0.35$) (Table IV-5). Despite its detrimental effects on the lake's ecology and biodiversity (Datta et al., 2021), water hyacinth plays a significant role in improving water quality (Villamagna & Murphy, 2010; Nguyen et al., 2015; Yan et al., 2017; Elizabeth et al., 2020; Kleinschroth et al., 2021; Mucheye et al., 2022). Water hyacinths act as nutrient filters, helping to control eutrophication (Cornwell et al., 1977; Villamagna & Murphy, 2010; Yan et al., 2017; Kleinschroth et al., 2021). For instance, Saraswati (2022) demonstrated their efficiency in absorbing phosphorus and nitrogen in an Indonesian reservoir. Similarly, Lu et al. (2018) reported water hyacinth's capacity to absorb 45.05% nitrogen and 58% total phosphorus in polluted rivers, with removal efficiencies of 36% for nitrogen (through nitrification/denitrification) and 40% for phosphorus via other mechanisms. Additionally, water hyacinths have been shown to effectively filter suspended solids and reduce turbidity in various water bodies (Elizabeth et al., 2020; Park & Richard, 2020; Thi Nguyen et al., 2015). However, the complex interaction between water hyacinth biomass and water quality underscores the need for further research to fully understand Lake Tana's ecological dynamics.

In this study, *in-situ* water temperature measurements (collected between 8 a.m. and 2 p.m.) were used to evaluate MODIS LSWT. However, the MODIS overpass time (~10:30 a.m. local time) did not always align with the *in-situ* measurement times. In tropical regions like Ethiopia, high air temperatures and solar radiation between 12 p.m. and 3 p.m. can

increase LSWT, particularly for measurements taken after the MODIS overpass. Consequently, MODIS LSWT underestimated LSWT by 1.48°C, which could largely be attributed to this timing mismatch. Similar findings have been reported in other studies, where errors stemmed from mismatches between *in-situ* data collection and MODIS overpass times, alongside other potential sources of error such as instrumental noise, sunlit effects, cloud contamination, and surface emissivity variations (Wan et al., 2002; Coll et al., 2005; Song et al., 2016). The temporal resolution mismatch between *in-situ* data and Sentinel-2 imagery posed another limitation. *In-situ* data, collected only in December and June, often did not align with Sentinel-2 acquisition dates, requiring the use of a gap of up to two days in this analysis. This temporal offset may introduce uncertainty, as rapid changes in algal blooms (Lee et al., 2005; Kislik et al., 2022) and sediment distribution (Garg et al., 2020) can occur due to weather and human activities. Similarly, Cillero Castro et al. (2020) reported errors caused by a three-day gap between *in-situ* Chl-*a* measurements and Sentinel-2 data. Despite these limitations, the results demonstrated a significant positive correlation between Sentinel-2 predicted and measured turbidity and Chl-*a*, suggesting Sentinel-2 imagery can effectively fill temporal gaps and capture variability in the system. Additional challenges include the movement of aquatic vegetation such as water hyacinth (northeastern and eastern shores) and Illinois pondweed (northwestern shore), which may lead to pixel mixing as these weeds drift from the shoreline toward the lake center due to water currents and wind. This movement can affect the accuracy of Sentinel-2 water quality estimates. Extensive cloud cover during the rainy season further limits the evaluation of physical and biological water quality parameters, underscoring the need for robust approaches to mitigate these challenges. Addressing these challenges through improved temporal synchronization, integration of multi-sensor data, and advanced processing techniques will enhance the accuracy and reliability of satellite-based water quality assessments in dynamic systems like Lake Tana.

4.5. CONCLUSION

This study evaluated the spatiotemporal variability of LSWT, turbidity, and Chl-*a* concentrations, and their interrelationships with water hyacinth biomass in Lake Tana,

Ethiopia. The results demonstrated strong positive correlations between MODIS LSWT and *in-situ* water temperature, as well as between *in-situ* turbidity and NDTI, and *in-situ* Chl-*a* and NDCI, confirming the reliability of remote sensing data for water quality assessment. High spatial and temporal variability was observed in LSWT, turbidity, and Chl-*a*. The spatial average LSWT exhibited decreasing trends in all seasons except the dry season, with localized warming in water hyacinth-infested areas and cooling near the Tana Belles hydroelectric power plant. Spatial averages of turbidity and Chl-*a* concentrations declined between January 2016 and December 2022. Water hyacinth biomass showed a non-significant positive correlation with LSWT but a significant negative correlation with turbidity and Chl-*a*, indicating that water hyacinths may slightly elevate LSWT while reducing turbidity and phytoplankton biomass. Overall, the water quality purification of Lake Tana improved from 2016 to 2022, possibly due to the expansion of water hyacinths and Illinois pondweed along the lake's shoreline, which contributed to nutrient absorption and sediment filtration. However, the findings highlight the need for integrated management strategies to balance the water purification role of water hyacinths with their broader ecological and hydrological impacts. These results provide critical insights for decision support systems and the development of strategic plans aimed at sustainable water resource management, environmental protection, and pollution prevention.

CHAPTER FIVE

5. GENERAL DISCUSSION

5.1. Introduction

Water hyacinth (*Eichhornia crassipes*), an invasive aquatic plant, poses significant ecological, economic, and social challenges worldwide (Datta et al., 2021), including in Lake Tana, Ethiopia. As Ethiopia's largest lake, Lake Tana is heavily infested with water hyacinth, threatening its biodiversity and habitat (Dersseh et al., 2019b; Dersseh et al., 2020; Damtie et al., 2022). Its rapid spread has raised concerns among water resource managers, agricultural industries, environmentalists, and local communities. The dense mats formed by water hyacinths not only affect water quality but also significantly alter the lake's hydrology by increasing evapotranspiration rates. These changes negatively impact aquatic biodiversity, fisheries, and water availability, exacerbating existing pressures on Lake Tana's ecosystem and the livelihoods that depend on it. Using appropriate remote sensing detection methods and determining the spatiotemporal distribution of the weed is important for decision-making, water resource management, and environmental protection (Thamaga & Dube, 2018). This doctoral research provides detailed insights into the spatiotemporal dynamics of water hyacinth in Lake Tana, its significant impacts on hydrology and water quality, and the efficacy of machine learning algorithms for detecting and monitoring water hyacinth infestations.

As the demand for reliable estimation of water hyacinth mapping from satellite data grows, comparing the performance of different machine learning algorithms can help identify the most effective method for detecting this invasive weed in the lake. This study demonstrated the utility of advanced satellite data analysis and robust detection models in capturing the spatiotemporal dynamics of water hyacinth and its associated effects on LSWT, turbidity, and Chl-*a* in Lake Tana. This doctoral research makes significant contributions to sustainable water resource management, environmental protection, pollution prevention, and policy development. By empowering stakeholders to design strategic interventions for lake

conservation and ecological restoration, the study facilitates the creation of targeted aquatic weed management strategies. These initiatives are crucial for mitigating the detrimental impacts of water hyacinths on Lake Tana's ecosystem, hydrology, and local livelihoods. Additionally, the findings offer valuable insights for broader water resource management and environmental protection efforts.

5.2. Findings and potential applications

This doctoral research offers a comprehensive analysis of water hyacinth dynamics, highlighting its significant impacts on the hydrology and water quality of Lake Tana. To address these challenges, the study evaluates advanced remote sensing technologies and machine learning techniques for the effective detection, monitoring, and assessment of water hyacinth infestations and their subsequent effects. By integrating these innovative approaches, the research provides valuable insights and tools for managing and mitigating the adverse consequences of water hyacinth proliferation in Lake Tana's ecosystem.

5.2. 1. Performances of machine learning algorithms for water hyacinth detection

Three machine learning algorithms—Random Forest (RF), Support Vector Machine (SVM), and Classification and Regression Tree (CART)—were evaluated for their ability to detect water hyacinth infestations in Lake Tana using remote sensing data. Among these, RF consistently outperformed the other algorithms, achieving an average overall accuracy of 97.8% for Sentinel-2 imagery and 95.5% for Landsat-8 imagery. This superior performance demonstrates the robustness of RF in handling complex datasets and extracting meaningful patterns for water hyacinth detection. The highest F1 scores were observed during the post-rainy season, attributable to the elevated spectral reflectance of water hyacinth in the near-infrared and red band regions during this period compared to other land use and land cover types. This makes the post-rainy season the optimal time for monitoring water hyacinth dynamics. These findings underscore the effectiveness of RF for near-real-time monitoring of the spatiotemporal distribution of water hyacinths, enabling precise and timely interventions. Regular geospatial assessments utilizing RF and remote sensing technologies

are essential for prompt detection and effective response to new infestations, particularly in the post-rainy season. This proactive approach supports the development of targeted management strategies and empowers decision-makers to mitigate the adverse impacts of water hyacinths.

5.2.2. Spatiotemporal dynamics of water hyacinth and associated water loss due to water hyacinth evapotranspiration

This doctoral research highlights the spatial and temporal distribution of water hyacinths in Lake Tana, with the most severe infestations occurring in the northeastern and eastern parts of the lake. Factors such as nutrient-rich waters, shallow depths, and prevailing winds could contribute to concentrated growth in these regions (Dersseh et al., 2020; Dersseh et al., 2019; Cai et al., 2023). Water hyacinth coverage peaked in 2019 but has fluctuated since, potentially influencing management interventions and removal efforts by local stakeholders (Muchye et al., 2022). Seasonal variations were evident, with peak coverage during the post-rainy season, possibly linked to increased nutrient runoff from agricultural activities during the rainy season, facilitating water hyacinth growth in the subsequent post-rainy season (Abebe et al., 2023; Dersseh et al., 2020). In contrast, minimum coverage during the pre-rainy season could reflect effective management interventions and environmental factors, such as the weed's dryness and color changes (Dersseh et al. 2020). This seasonal variability underscores the need for interventions during the post-rainy season to control peak growth.

Moreover, the significant positive correlation between water hyacinth coverage and lake surface area suggests that lake expansion into floodplains could provide favorable conditions for weed proliferation, particularly in shallow, nutrient-enriched zones (Cai et al., 2023). These findings emphasize the importance of policies focused on nutrient management, pollutant reduction, and sustainable lake conservation to mitigate the impacts of water hyacinth and safeguard Lake Tana's ecological and hydrological health.

From October 2015 to December 2023, water hyacinth evapotranspiration resulted in an estimated water loss of approximately 176 million m³, equivalent to 0.61% of Lake Tana's total volume, despite the weed covering only 0.29% of the lake's surface area. Projections

indicate that if water hyacinth coverage were to increase to 20%, water loss could rise dramatically to 12.24 billion m³ or 43.1% of the lake's total volume. This alarming scenario underscores the urgent need for effective, season-specific management strategies, particularly during the post-rainy season when water hyacinth growth accelerates. While the evapotranspiration rate declined slightly by 0.114 mm/month over the study period, total water loss continued to grow. This could be attributed to the weed's expanding spatial coverage, which increases the surface area available for evapotranspiration (Abebe et al., 2023). Integrating evapotranspiration data into water resource management plans could be essential for mitigating water loss and ensuring the sustainability of Ethiopia's vital water resources. These findings also highlight the critical importance of season-specific management strategies during the post-rainy season to control peak growth and associated water loss.

5.2.3. Spatiotemporal distribution of physical and biological water quality parameters and their relationship with water hyacinth biomass

This doctoral research revealed high spatial and temporal variability in Lake Tana's LSWT, turbidity, and Chl-*a* concentrations. Additionally, the research elucidated the complex relationship between various water quality parameters—such as LSWT, turbidity, and Chl-*a* concentrations—and the biomass of water hyacinth. Higher LSWT values were consistently observed in shallow, turbid areas and regions around dense water hyacinth coverage, while deeper parts of the lake exhibited lower LST, likely due to thermal inertia (Iestyn Woolway & Merchant, 2017) and reduced turbidity (Paaajmans et al., 2008). Consistent warming trends in the northeastern part of the lake across seasons could be attributed to water hyacinth infestation, which increases water residence time and elevates surface temperatures around the infested areas (Tobias et al., 2019). In contrast, LSWT was lower near the Tana Belles hydroelectric power plant, potentially due to cold-water mixing from outflows. A decreasing trend in LSWT was observed from 2001 to 2022, accompanied by a significant positive correlation with air temperature trends, both of which declined from 2001 to 2021. This pattern could reflect the influence of regional green development

initiatives and increased vegetation cover (Jalleta, 2021). Additionally, LSWT anomalies showed a significant positive correlation with Pacific Ocean SST in the Niño 3.4 region (Figure IV-10), while no significant correlations were observed with Indian or Atlantic Ocean SST anomalies. These findings underscore the complex interactions between local factors, such as vegetation cover and regional climate trends, and global influences, such as Pacific Ocean SST variability. Together, they could have broader implications for Lake Tana's hydrology, ecological health, and role in regional climate systems.

Spatial and temporal variability was also evident in turbidity and Chl-*a* concentrations. Higher turbidity and Chl-*a* values were consistently observed in the northeastern, eastern, and southwestern regions, likely driven by sediment resuspension and high nutrient concentrations in these areas (Facco et al., 2021; Yu et al., 2014; Dersseh et al., 2019, 2020; Cai et al., 2023). In contrast, lower turbidity and Chl-*a* levels were observed in the central and deeper parts of the lake, where sedimentation and nutrient concentrations are minimal. Seasonal patterns revealed that turbidity and Chl-*a* concentrations were higher during the rainy season, likely due to increased sediment runoff and nutrient loading from tributaries (Mucheye et al., 2022). In the dry season, minimal sediment runoff and nutrient loads were observed. The expansion of water hyacinth along the shoreline was negatively correlated with turbidity and Chl-*a* concentrations, highlighting the weed's potential role in filtering suspended solids and nutrients (Villamagna & Murphy, 2010; Nguyen et al., 2015; Yan et al., 2017; Elizabeth et al., 2020; Kleinschroth et al., 2021; Mucheye et al., 2022). While this filtering effect could improve water clarity, it also reduces light availability, which diminishes phytoplankton productivity and alters nutrient dynamics. From 2016 to 2023, an overall decline in turbidity and Chl-*a* concentrations was observed, likely linked to the expanding coverage of water hyacinth, which limits light penetration and affects nutrient availability in the lake.

This dual role highlights water hyacinth as both a potential contributor to improved water clarity and a disruptor of ecological balance by blocking light and reducing phytoplankton productivity. While the water hyacinth's filtering role could enhance water clarity, specific areas of the lake, particularly near cities and major river tributaries (Figure

IV-8), experienced water quality deterioration. To safeguard Lake Tana's water quality, it is essential to implement policies addressing agricultural runoff, urban waste management, and nutrient reduction. Establishing buffer zones and implementing proper fertilizer application practices around Lake Tana and its tributaries could effectively mitigate sediment and nutrient inflow. The findings of this study provide valuable insights for environmental and climate change experts in developing adaptation and mitigation strategies. Policymakers and water resource managers could leverage these results to create targeted water quality improvement policies and sustainable water resource management strategies. Effective management approaches should aim to balance water hyacinth control with nutrient monitoring to maintain Lake Tana's ecological balance, safeguard water quality, and ensure the sustainability of its ecosystem and resources.

5.3 Integration of NDVI-based spatial distribution of water hyacinth into a portal system

The spatial distribution of water hyacinth, estimated using NDVI threshold values (0.6 to 1), has been integrated into a portal system for monitoring its expansion over time (Figure V-1). The portal enables users to filter and visualize the spatial distribution and coverage of water hyacinth for specific dates and months from 2015 onward, utilizing the Sentinel-2 dataset. This decision-support tool provides stakeholders with near real-time data to monitor water hyacinth infestation trends, assess ecological and hydrological impacts, and implement timely management interventions. Integrating the NDVI-based spatial distribution of water hyacinth into decision-support portal systems enhances precise management and facilitates data-driven policymaking, contributing to the long-term sustainability of Lake Tana's resources.

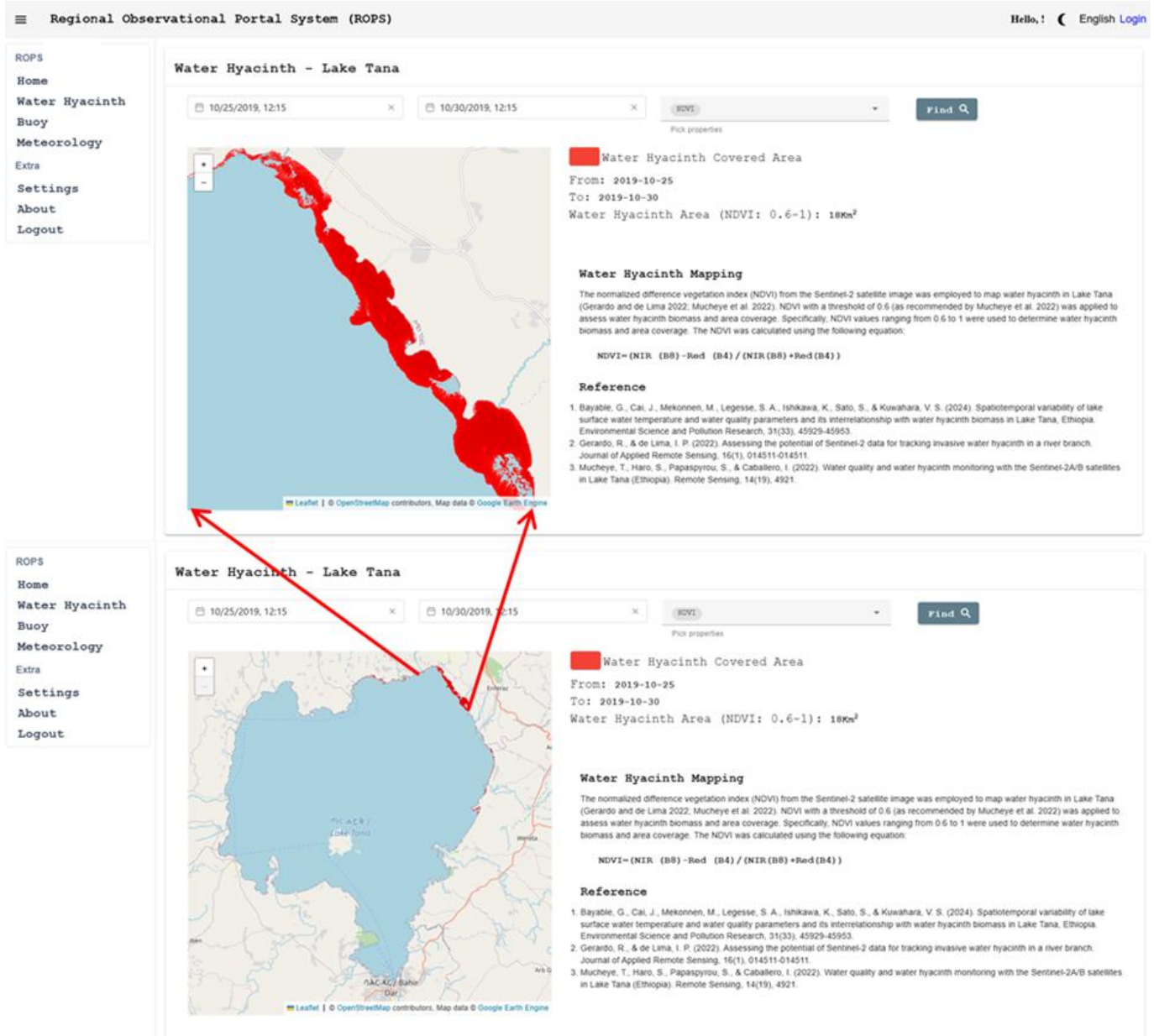


Figure V-1: Portal-based visualization of water hyacinth spatial distribution (shown in red) and coverage in Lake Tana, Ethiopia, derived using October 2019 Sentinel-2 NDVI threshold values (0.6 to 1)

5.4 Future research directions

This research comprehensively analyzed the spatiotemporal dynamics of water hyacinth and its impacts on water volume loss and water quality parameters, including LST, turbidity, and Chl-*a*, in Lake Tana. Medium-resolution multispectral remote sensing imagery,

such as Landsat-8 and Sentinel-2, was employed to compare the performance of three commonly used machine learning algorithms—CART, RF, and SVM—and to estimate water hyacinth distribution. The analysis leveraged cloud-based geospatial platforms, including Google Earth Engine (GEE), enabling large-scale, efficient processing and analysis of remote sensing data. However, these methods based on medium-resolution imagery may have limitations in detecting small and fragmented water hyacinth infestations. Future research should prioritize the use of high-resolution satellite imagery with spatial resolutions below 10 m, such as Maxar, SkySat, PlanetScope, and WorldView, to enhance detection capabilities, particularly for smaller water hyacinth infestations. Additionally, integrating diverse datasets, including Sentinel-2 optical data, Sentinel-1 SAR parameters, and topographical and climatic variables, could significantly improve the accuracy of water hyacinth distribution estimation. Future research should also explore advanced fusion techniques that integrate optical and radar data to address challenges posed by cloud cover and vegetation density. Furthermore, leveraging deep learning models trained with adequate ground-truth data from the study area could significantly enhance the accuracy and reliability of water hyacinth detection and spatial coverage estimation. Moreover, future research should focus on conducting on-site measurements of lake water evaporation and water hyacinth evapotranspiration to accurately quantify the specific impact of water hyacinth on water loss. Developing a localized plant coefficient for water hyacinth, tailored to Lake Tana's unique environmental conditions and combined with remote sensing-based evapotranspiration models, could significantly improve regional water loss estimates and inform hydrological planning.

Inflow and outflow data are expected to significantly impact LSWT and various water quality parameters. Future studies should further investigate the influence of hydrological inflow and outflow on key water quality indicators, including LSWT, turbidity, Chl-*a*, total phosphorus, and total nitrogen. Additionally, water quality estimation accuracy could be enhanced by harmonizing data from Sentinel-2, Sentinel-3, and high-resolution satellites such as Planet, which offer 3–5 m spatial resolution with daily coverage, thereby leveraging the unique spatial, temporal, and spectral strengths of each mission. By addressing these

future research directions, stakeholders will be better equipped to mitigate the impacts of water hyacinths, adapt to evolving climatic conditions, and ensure the sustainable management of Lake Tana's critical ecological and hydrological resources.

REFERENCES

- Abbas, Z., Arooj, F., Ali, S., Zaheer, I. E., Rizwan, M., & Riaz, M. A. (2019). Phytoremediation of landfill leachate waste contaminants through floating bed technique using water hyacinth and water lettuce. *International Journal of Phytoremediation*, 21(13), 1356–1367.
<https://doi.org/10.1080/15226514.2019.1633259>
- Abdel-Rahman, E. M., Mutanga, O., Adam, E., & Ismail, R. (2014). Detecting Sirex noctilio grey-attacked and lightning-struck pine trees using airborne hyperspectral data, random forest and support vector machines classifiers. *ISPRS Journal of Photogrammetry and Remote Sensing*, 88, 48–59.
<https://doi.org/10.1016/j.isprsjprs.2013.11.013>
- Abebe, T., Awoke, B. G., & Nega, W. (2023). Spatiotemporal patterns of water hyacinth dynamics as a response to seasonal climate variability in Lake Tana, Ethiopia. *Applied Water Science*, 13(9), 1–16. <https://doi.org/10.1007/s13201-023-01975-6>
- Ade, C., Khanna, S., Lay, M., Ustin, S. L., & Hestir, E. L. (2022). Genus-Level Mapping of Invasive Floating Aquatic Vegetation Using Sentinel-2 Satellite Remote Sensing. *Remote Sensing*, 14(13), 1–20. <https://doi.org/10.3390/rs14133013>
- Agjee, N., Mutanga, O., & Ismail, R. (2015). Remote sensing bio-control damage on aquatic invasive alien plant species. *South African Journal of Geomatics*, 4(4), 464.
<https://doi.org/10.4314/sajg.v4i4.8>
- Aguilar-Lome, J., Soca-Flores, R., & Gómez, D. (2021). Evaluation of the Lake Titicaca's surface water temperature using LST MODIS time series (2000–2020). *Journal of South American Earth Sciences*, 112(August).
<https://doi.org/10.1016/j.jsames.2021.103609>
- Aitelghazi, A., Rhinane, H., Bensalmia, A., & Giuliani, G. (2019). Using the Landsat-7 data to study the correlation between the surface temperature and phytoplankton turbidity Case study: Al Massira Lake (Settat - Morocco). *Materials Today: Proceedings*, 13, 496–504. <https://doi.org/10.1016/j.matpr.2019.04.006>
- Albright, T. P., Moorhouse, T. G., & McNabb, T. J. (2004). The rise and fall of water

- hyacinth in Lake Victoria and the Kagera River basin, 1989-2001. *Journal of Aquatic Plant Management*, 42(JUL.), 73–84.
- Alcântara, E. H., Stech, J. L., Lorenzetti, J. A., Bonnet, M. P., Casamitjana, X., Assireu, A. T., & Novo, E. M. L. de M. (2010). Remote sensing of water surface temperature and heat flux over a tropical hydroelectric reservoir. *Remote Sensing of Environment*, 114(11), 2651–2665. <https://doi.org/10.1016/j.rse.2010.06.002>
- Al-lami, A. K., Abbood, R. A., Al Maliki, A. A., & Al-Ansari, N. (2021). Using vegetation indices for monitoring the spread of Nile Rose plant in the Tigris River within Wasit province, Iraq. *Remote Sensing Applications: Society and Environment*, 22, 100471. <https://doi.org/10.1016/j.rsase.2021.100471>
- Alemu, M. L., Worqlul, A. W., Zimale, F. A., Tilahun, S. A., & Steenhuis, T. S. (2020). Water balance for a tropical lake in the volcanic highlands: Lake Tana, Ethiopia. *Water (Switzerland)*, 12(10). <https://doi.org/10.3390/w12102737>
- Alemu, M. M., & Bawoke, G. T. (2020). Analysis of spatial variability and temporal trends of rainfall in Amhara Region, Ethiopia. *Journal of Water and Climate Change*, 11(4), 1505–1520. <https://doi.org/10.2166/wcc.2019.084>
- Alshaikh, A. Y. (2016). *Detection of Sea Surface Temperature and Thermal Pollution of Agricultural Coastal Areas using Thermal Infrared , Jeddah City , West KSA*. 5(1), 51–60.
- Andrade, C., Alcântara, E., Bernardo, N., & Kampel, M. (2019). An assessment of semi-analytical models based on the absorption coefficient in retrieving the chlorophyll-a concentration from a reservoir. *Advances in Space Research*, 63(7), 2175–2188. <https://doi.org/10.1016/j.asr.2018.12.023>
- Andrzej Urbanski, J., Wochna, A., Bubak, I., Grzybowski, W., Lukawska-Matuszewska, K., Łacka, M., Śliwińska, S., Wojtasiewicz, B., & Zajęzkowski, M. (2016). Application of Landsat 8 imagery to regional-scale assessment of lake water quality. *International Journal of Applied Earth Observation and Geoinformation*, 51, 28–36. <https://doi.org/10.1016/j.jag.2016.04.004>
- Aplin, P. (2005). Remote sensing: Ecology. *Progress in Physical Geography*, 29(1), 104–

113. <https://doi.org/10.1191/030913305pp437pr>
- Arp, R. S., Fraser, G. C. G., & Hill, M. P. (2017). Quantifying the economic water savings benefit of water hyacinth (*Eichhornia crassipes*) control in the vaalharts irrigation scheme. *Water SA*, 43(1), 58–66. <https://doi.org/10.4314/wsa.v43i1.09>
- Arunpandi, N., Jyothibabu, R., Dhanya, P., Jagadeesan, L., Rashid, C. P., & Sarath, S. (2022). Alarming waterweeds proliferation in the Vembanad Lake System might significantly increase water loss through transpiration. *Environmental Monitoring and Assessment*, 194(4). <https://doi.org/10.1007/s10661-022-09938-1>
- Asmare, T., Demissie, B., Nigusse, A. G., & GebreKidan, A. (2020). Detecting Spatiotemporal Expansion of Water Hyacinth (*Eichhornia crassipes*) in Lake Tana, Northern Ethiopia. *Journal of the Indian Society of Remote Sensing*, 48(5), 751–764. <https://doi.org/10.1007/s12524-020-01107-6>
- Avendaño-Valencia, L. D., & Fassois, S. D. (2015). Natural vibration response based damage detection for an operating wind turbine via Random Coefficient Linear Parameter Varying AR modelling. *Journal of Physics: Conference Series*, 628(1), 273–297. <https://doi.org/10.1088/1742-6596/628/1/012073>
- Balsamo, G., Dutra, E., Stepanenko, V. M., Viterbo, P., Miranda, P. M. A., & Mironov, D. (2010). Deriving an effective lake depth from satellite lake surface temperature data: A feasibility study with MODIS data. *Boreal Environment Research*, 15(2), 178–190.
- Barclay S. W., & Sumner, D. M. (2006). Alternate corrections for estimating actual wetland evapotranspiration from potential evapotranspiration. *Wetlands*, 26(2), 528–543. [https://doi.org/10.1672/0277-5212\(2006\)26\[528:ACFEAW\]2.0.CO;2](https://doi.org/10.1672/0277-5212(2006)26[528:ACFEAW]2.0.CO;2)
- Bareuther, M., Klinge, M., & Buerkert, A. (2020). Spatio-temporal dynamics of algae and macrophyte cover in urban lakes: A remote sensing analysis of bellandur and varthur wetlands in Bengaluru, India. *Remote Sensing*, 12(22), 1–25. <https://doi.org/10.3390/rs12223843>
- Bayable, G., & Alemu, G. (2022). Spatiotemporal variability of land surface temperature in north-western Ethiopia. *Environmental Science and Pollution Research*, 29(2), 2629–2641. <https://doi.org/10.1007/s11356-021-15763-9>

- Bayable, G., Cai, J., Mekonnen, M., Legesse, S. A., Ishikawa, K., Imamura, H., & Kuwahara, V. S. (2023). Detection of Water Hyacinth (*Eichhornia crassipes*) in Lake Tana, Ethiopia, Using Machine Learning Algorithms. *Water (Switzerland)*, 15(5). <https://doi.org/10.3390/w15050880>
- Bayable, G., Cai, J., Mekonnen, M., Legesse, S. A., Ishikawa, K., Sato, S., & Kuwahara, V. S. (2024). Spatiotemporal variability of lake surface water temperature and water quality parameters and its interrelationship with water hyacinth biomass in Lake Tana, Ethiopia. *Environmental Science and Pollution Research*, 31(33), 45929–45953. <https://doi.org/10.1007/s11356-024-34212-x>
- Bayable, G., & Gashaw, T. (2021). Spatiotemporal variability of agricultural drought and its association with climatic variables in the Upper Awash Basin, Ethiopia. *SN Applied Sciences*, 3(4), 1–20. <https://doi.org/10.1007/s42452-021-04471-1>
- Belayhun, M., & Mekuriaw, A. (2024). Modeling water hyacinth (*Eichhornia crassipes*) distribution in Lake Tana, Ethiopia, using machine learning. *Remote Sensing Applications: Society and Environment*, 101273.
- Belgiu, M., & Drăgu, L. (2016). Random forest in remote sensing: A review of applications and future directions. *ISPRS Journal of Photogrammetry and Remote Sensing*, 114, 24–31. <https://doi.org/10.1016/j.isprsjprs.2016.01.011>
- Bessell-Browne, P., Negri, A. P., Fisher, R., Clode, P. L., Duckworth, A., & Jones, R. (2017). Impacts of turbidity on corals: The relative importance of light limitation and suspended sediments. *Marine Pollution Bulletin*, 117(1–2), 161–170. <https://doi.org/10.1016/j.marpolbul.2017.01.050>
- Bick, E., de Lange, E. S., Kron, C. R., da Silva Soler, L., Liu, J., & Nguyen, H. D. (2020). Effects of salinity and nutrients on water hyacinth and its biological control agent, *Neochetina bruchi*. *Hydrobiologia*, 847(15), 3213–3224. <https://doi.org/10.1007/s10750-020-04314-x>
- Bid, S., & Siddique, G. (2019). Identification of seasonal variation of water turbidity using NDTI method in Panchet Hill Dam, India. *Modeling Earth Systems and Environment*, 5(4), 1179–1200. <https://doi.org/10.1007/s40808-019-00609-8>

- Birara, H., Pandey, R. P., & Mishra, S. K. (2018). Trend and variability analysis of rainfall and temperature in the tana basin region, Ethiopia. *Journal of Water and Climate Change*, 9(3), 555–569. <https://doi.org/10.2166/wcc.2018.080>
- Bouklikha, A., Habi, M., Elouissi, A., Benzater, B., & Hamoudi, S. (2020). The innovative trend analysis applied to annual and seasonal rainfall in the tafna watershed (Algeria). *Revista Brasileira de Meteorologia*, 35(4), 631–647. <https://doi.org/10.1590/0102-77863540068>
- Brendonck, L., Maes, J., Rommens, W., Dekeza, N., Nhiwatiwa, T., Barson, M., Callebaut, V., Phiri, C., Moreau, K., Gratwicke, B., Stevens, M., Alyn, N., Holsters, E., Ollevier, F., & Marshall, B. (2003). The impact of water hyacinth (*Eichhornia crassipes*) in a eutrophic subtropical impoundment (Lake Chivero, Zimbabwe). II. Species diversity. *Archiv Fur Hydrobiologie*, 158(3), 389–405. <https://doi.org/10.1127/0003-9136/2003/0158-0389>
- Brieman, L.; Friedman, J.H.; Olshen, R.A.; Stone, C.J.(1984). *Classification and Regression Trees*, 1st ed.; Routledge: London, UK, Vol.45, pp. 5–32.
- Breiman, L. (2001). Random Forests. *Mach. Learn*, 45, 5–32
- Caballero, I., & Stumpf, R. P. (2020). Towards routine mapping of shallow bathymetry in environments with variable turbidity: Contribution of sentinel-2A/B satellites mission. *Remote Sensing*, 12(3). <https://doi.org/10.3390/rs12030451>
- Caballero, I., Fernández, R., Escalante, O. M., Mamán, L., & Navarro, G. (2020). New capabilities of Sentinel-2A/B satellites combined with in situ data for monitoring small harmful algal blooms in complex coastal waters. *Scientific Reports*, 10(1), 1–14. <https://doi.org/10.1038/s41598-020-65600-1>
- Cai, J., Jiao, C., Mekonnen, M., Legesse, S. A., Ishikawa, K., Wondie, A., & Sato, S. (2023). Water hyacinth infestation in Lake Tana, Ethiopia: a review of population dynamics. *Limnology*, 24(1), 51–60. <https://doi.org/10.1007/s10201-022-00706-1>
- Carella, E., Orusa, T., Viani, A., Meloni, D., Borgogno-mondino, E., & Orusa, R. (2022). An Integrated, Tentative Remote-Sensing Approach Based on NDVI Entropy to Model Canine Distemper Virus in Wildlife and to Prompt Science-Based Management

- Policies. *Animals*, 12(8). <https://doi.org/10.3390/ani12081049>
- Carney, C.E. (1998). A primer on lake eutrophication and related pollution problems: Kansas Department of Health and Environment. Bureau of Environmental Field Services
- Cavalli, R. M., Laneve, G., Fusilli, L., Pignatti, S., & Santini, F. (2009). Remote sensing water observation for supporting Lake Victoria weed management. *Journal of Environmental Management*, 90(7), 2199–2211. <https://doi.org/10.1016/j.jenvman.2007.07.036>
- Chang, K. T., Merghadi, A., Yunus, A. P., Pham, B. T., & Dou, J. (2019). Evaluating scale effects of topographic variables in landslide susceptibility models using GIS-based machine learning techniques. *Scientific Reports*, 9(1), 1–22. <https://doi.org/10.1038/s41598-019-48773-2>
- Chavula, G., Brezonik, P., Thenkabail, P., Johnson, T., & Bauer, M. (2009). Estimating the surface temperature of Lake Malawi using AVHRR and MODIS satellite imagery. *Physics and Chemistry of the Earth*, 34(13–16), 749–754. <https://doi.org/10.1016/j.pce.2009.08.001>
- Chih-Wei Hsu, Chih-Chung Chang, and C.-J. L. (2008). A Practical Guide to Support Vector Classification. *BJU International*, 101(1), 1396–1400. <http://www.csie.ntu.edu.tw/~cjlin/papers/guide/guide.pdf>
- Chorus, I., Bartram, J. (1999). Toxic Cyanobacteria in Water: A Guide to Their Public Health Consequences, Monitoring and Management. London, United Kingdom. E. and F.N. Spon/Chapman and Hall.
- Churko, E. E., Nhamo, L., & Chitakira, M. (2024). Multispectral remote sensing approach of predicting the potential distribution and evaluating the current spread of water hyacinth (*Eichhornia crassipes*). *Sustainable Water Resources Management*, 10(1), 1–14. <https://doi.org/10.1007/s40899-023-01019-6>
- Cillero Castro, C., Domínguez Gómez, J. A., Delgado Martín, J., Hinojo Sánchez, B. A., Cereijo Arango, J. L., Cheda Tuya, F. A., & Diaz-Varela, R. A. (2020). An UAV and Satellite Multispectral Data Approach to Monitor Water Quality in Small Reservoirs.

Remote Sensing, 12(9), 1–33.

- Coetzee, J. A., Jones, R. W., & Hill, M. P. (2014). Water hyacinth, *Eichhornia crassipes* (Pontederiaceae), reduces benthic macroinvertebrate diversity in a protected subtropical lake in South Africa. *Biodiversity and Conservation*, 23(5), 1319–1330. <https://doi.org/10.1007/s10531-014-0667-9>
- Coll, C., Caselles, V., Galve, J. M., Valor, E., Niclòs, R., Sánchez, J. M., & Rivas, R. (2005). Ground measurements for the validation of land surface temperatures derived from AATSR and MODIS data. *Remote Sensing of Environment*, 97(3), 288–300. <https://doi.org/10.1016/j.rse.2005.05.007>
- Congalton, R. G. (1991). A review of assessing the accuracy of classifications of remotely sensed data. *Remote Sensing of Environment*, 37(1), 35–46. [https://doi.org/10.1016/0034-4257\(91\)90048-B](https://doi.org/10.1016/0034-4257(91)90048-B)
- Cooper, M. (2010). Advanced Bash-Scripting Guide An in-depth exploration of the art of shell scripting Table of Contents. *Okt 2005 Abrufbar Uber Httpwww Tldp OrgLDPabsabsguide Pdf Zugriff 1112 2005, 2274*(November 2008), 2267–2274. <https://doi.org/10.1002/hyp>
- Cornwell DA, Zoltek J, Patrinely CD (1977) Nutrient removal by water hyacinths. *J Water Pollut Control Fed* 49:57–65.
- Cortes, C.; Vapnik, V. (1995). Support-vector networks. *Mach. Learn*, 20, 273–297.
- Crosman, E. T., & Horel, J. D. (2009). MODIS-derived surface temperature of the Great Salt Lake. *Remote Sensing of Environment*, 113(1), 73–81. <https://doi.org/10.1016/j.rse.2008.08.013>
- Dall’Olmo, G., & Gitelson, A. A. (2006). Effect of bio-optical parameter variability and uncertainties in reflectance measurements on the remote estimation of chlorophyll-a concentration in turbid productive waters: Modeling results. *Applied Optics*, 45(15), 3577–3592. <https://doi.org/10.1364/AO.45.003577>
- Damtie, Y. A., Berlie, A. B., Gessese, G. M., & Ayalew, T. K. (2022). Characterization of water hyacinth (*Eichhornia crassipes* (Mart.) Solms) biomass in Lake Tana, Ethiopia. *All Life*, 15(1), 1126–1140. <https://doi.org/10.1080/26895293.2022.2134933>

- Damtie, Y. A., Mengistu, D. A., & Meshesha, D. T. (2021). Spatial coverage of water hyacinth (*Eichhornia crassipes* (Mart.) Solms) on Lake Tana and associated water loss. *Heliyon*, 7(10), e08196. <https://doi.org/10.1016/j.heliyon.2021.e08196>
- Danandeh Mehr, A., Hrnjica, B., Bonacci, O., & Torabi Haghighi, A. (2021). Innovative and successive average trend analysis of temperature and precipitation in Osijek, Croatia. *Theoretical and Applied Climatology*, 145(3–4), 875–890. <https://doi.org/10.1007/s00704-021-03672-3>
- Danbara, T. T. (2014). Deriving water quality indicators of Lake Tana, Ethiopia, from Landsat-8. *University of Twente Faculty of Geo-Information and Earth Observation (ITC)*, 68. http://www.itc.nl/library/papers_2014/msc/wrem/danbara.pdf
- Das, N., Sagar, A., Bhattacharjee, R., Agnihotri, A. K., Ohri, A., & Gaur, S. (2022). Time series forecasting of temperature and turbidity due to global warming in river Ganga at and around Varanasi, India. *Environmental Monitoring and Assessment*, 194(9). <https://doi.org/10.1007/s10661-022-10274-7>
- Das, S. (2021). Dynamics of streamflow and sediment load in Peninsular Indian rivers (1965–2015). *Science of the Total Environment*, 799, 149372. <https://doi.org/10.1016/j.scitotenv.2021.149372>
- Datta, A., Maharaj, S., Prabhu, G. N., Bhowmik, D., Marino, A., Akbari, V., Rupavatharam, S., Sujeetha, J. A. R. P., Anantrao, G. G., Poduvattil, V. K., Kumar, S., & Kleczkowski, A. (2021). Monitoring the Spread of Water Hyacinth (*Pontederia crassipes*): Challenges and Future Developments. *Frontiers in Ecology and Evolution*, 9(January), 1–8. <https://doi.org/10.3389/fevo.2021.631338>
- De Carlo, E. H., Beltran, V. L., & Tomlinson, M. S. (2004). Composition of water and suspended sediment in streams of urbanized subtropical watersheds in Hawaii. *Applied Geochemistry*, 19(7), 1011–1037. <https://doi.org/10.1016/j.apgeochem.2004.01.004>
- de Raús Maúre, E., Terauchi, G., Ishizaka, J., Clinton, N., & DeWitt, M. (2021). Globally consistent assessment of coastal eutrophication. *Nature Communications*, 12(1), 1–9. <https://doi.org/10.1038/s41467-021-26391-9>
- De Roos, A. J., Gurian, P. L., Robinson, L. F., Rai, A., Zakeri, I., & Kondo, M. C. (2017).

- Review of epidemiological studies of drinking-water turbidity in relation to acute gastrointestinal illness. *Environmental Health Perspectives*, 125(8).
<https://doi.org/10.1289/EHP1090>
- Dejen, E., Sibbing, F. A., & Vijverberg, J. (2003). Reproductive strategies of two sympatric “small barbs” (*Barbus humilis* and *B. tanapelagius*, Cyprinidae) in Lake Tana, Ethiopia. *Netherlands Journal of Zoology*, 52(2–4), 281–299.
<https://doi.org/10.1163/156854203764817724>
- Dersseh, M. G., Kibret, A. A., Tilahun, S. A., Worqlul, A. W., Moges, M. A., Dagnew, D. C., Abebe, W. B., & Melesse, A. M. (2019a). Potential of water hyacinth infestation on Lake Tana, Ethiopia: A prediction using a GIS-based multi-criteria technique. *Water (Switzerland)*, 11(9), 1–17. <https://doi.org/10.3390/w11091921>
- Dersseh, M. G., Melesse, A. M., Tilahun, S. A., Abate, M., & Dagnew, D. C. (2019b). Water hyacinth: Review of its impacts on hydrology and ecosystem services-Lessons for management of Lake Tana. In *Extreme Hydrology and Climate Variability: Monitoring, Modelling, Adaptation and Mitigation* (Vol. 1824). Elsevier Inc.
<https://doi.org/10.1016/B978-0-12-815998-9.00019-1>
- Dersseh, M. G., Steenhuis, T. S., Kibret, A. A., Eneyew, B. M., Kebedew, M. G., Zimale, F. A., Worqlul, A. W., Moges, M. A., Abebe, W. B., Mhiret, D. A., Melesse, A. M., & Tilahun, S. A. (2022). Water Quality Characteristics of a Water Hyacinth Infested Tropical Highland Lake: Lake Tana, Ethiopia. *Frontiers in Water*, 4(March), 1–17.
<https://doi.org/10.3389/frwa.2022.774710>
- Dersseh, M. G., Tilahun, S. A., Worqlul, A. W., Moges, M. A., Abebe, W. B., Mhiret, D. A., & Melesse, A. M. (2020). Spatial and temporal dynamics of water hyacinth and its linkage with lake-level fluctuation: Lake tana, a sub-humid region of the Ethiopian Highlands. *Water (Switzerland)*, 12(5), 1–15. <https://doi.org/10.3390/w12051435>
- Dewantoro, M. D. R., Ulfa, M., & Supatmanto, B. D. (2024). Water Turbidity Mapping Using Sentinel-2A Imagery and Cloud Based Google Earth Engine in Saguling Reservoir. *IOP Conference Series: Earth and Environmental Science*, 1343(1).
<https://doi.org/10.1088/1755-1315/1343/1/012027>

- Djihouessi, M. B., Tigo, B. A., & Aina, M. P. (2021). The use of nutrient budget approach for informing eutrophication management in urbanised shallow coastal lakes: A case study from Lake Nokoué in Benin. *Ecohydrology and Hydrobiology*, 21(2), 341–353. <https://doi.org/10.1016/j.ecohyd.2020.11.003>
- Dogliotti, A. I., Ruddick, K. G., Nechad, B., Doxaran, D., & Knaeps, E. (2015). A single algorithm to retrieve turbidity from remotely-sensed data in all coastal and estuarine waters. *Remote Sensing of Environment*, 156, 157–168. <https://doi.org/10.1016/j.rse.2014.09.020>
- Doorenbos, J., & Pruitt, W. O. (1977). Guidelines for predicting crop water requirements. *FAO Irrigation and Drainage Paper*, 24, 144.
- Duan, Z., & Bastiaanssen, W. G. M. (2013a). Characterizing spatial and temporal variations of surface temperature of Lake Tana (Ethiopia) using MODIS data. *International Geoscience and Remote Sensing Symposium (IGARSS)*, 3781–3784. <https://doi.org/10.1109/IGARSS.2013.6723654>
- Duan, Z., & Bastiaanssen, W. G. M. (2013b). Estimating water volume variations in lakes and reservoirs from four operational satellite altimetry databases and satellite imagery data. *Remote Sensing of Environment*, 134(November), 403–416. <https://doi.org/10.1016/j.rse.2013.03.010>
- Dube, T., Gumindoga, W., & Chawira, M. (2014). Detection of land cover changes around Lake Mutirikwi, Zimbabwe, based on traditional remote sensing image classification techniques. *African Journal of Aquatic Science*, 39(1), 89–95. <https://doi.org/10.2989/16085914.2013.870068>
- Dube, T., Mutanga, O., Sibanda, M., Bangamwabo, V., & Shoko, C. (2017). Testing the detection and discrimination potential of the new Landsat 8 satellite data on the challenging water hyacinth (*Eichhornia crassipes*) in freshwater ecosystems. *Applied Geography*, 84, 11–22. <https://doi.org/10.1016/j.apgeog.2017.04.005>
- Dube, T., Sibanda, M., Bangamwabo, V., & Shoko, C. (2018). Establishing the link between urban land cover change and the proliferation of aquatic hyacinth (*Eichhornia crassipes*) in Harare Metropolitan, Zimbabwe. *Physics and Chemistry of the Earth*,

- 108(June), 19–27. <https://doi.org/10.1016/j.pce.2018.09.010>
- Elhag, M., Gitas, I., Othman, A., Bahrawi, J., & Gikas, P. (2019). Assessment of water quality parameters using temporal remote sensing spectral reflectance in arid environments, Saudi Arabia. *Water (Switzerland)*, 11(3). <https://doi.org/10.3390/w11030556>
- Elhag, M., Gitas, I., Othman, A., Bahrawi, J., Psilovikos, A., & Al-Amri, N. (2021). Time series analysis of remotely sensed water quality parameters in arid environments, Saudi Arabia. *Environment, Development and Sustainability*, 23(2), 1392–1410. <https://doi.org/10.1007/s10668-020-00626-z>
- Elizabeth, J., Yuniati, R., & Wardhana, W. (2020). The capacity of water hyacinth as biofilter and bioaccumulator based on its size. *IOP Conference Series: Materials Science and Engineering*, 902(1). <https://doi.org/10.1088/1757-899X/902/1/012067>
- Elmahdy, S., Mohamed, M., & Ali, T. (2020). Land use/land cover changes impact on groundwater level and quality in the northern part of the United Arab Emirates. *Remote Sensing*, 12(11). <https://doi.org/10.3390/rs12111715>
- EPA (U.S. Environmental Protection Agency)2023 Nutrient Pollution: Climate Change and Harmful Algal Blooms. <https://www.epa.gov/nutrientpollution/climate-change-and-harmful-algal-blooms>. Accessed 7 January 2023
- Facco, D. S., Guasselli, L. A., Ruiz, L. F. C., Simioni, J. P. D., & Dick, D. G. (2021). Spectral reflectance in the spatial-temporal dynamic of turbidity, itaipu reservoir, brazil. *Anuario Do Instituto de Geociencias*, 44, 1–17. https://doi.org/10.11137/1982-3908_2021_44_41228
- Fadel, A., Faour, G., & Slim, K. (2016). Assessment of The trophic state and Chlorophyll-a concentrations using Landsat OLI in Karaoun reservoir, Lebanon. *Lebanese Science Journal*, 17(2), 130–145. <https://doi.org/10.22453/ljsj-017.2.130145>
- Fernández-González, C., Tarran, G. A., Schuback, N., Woodward, E. M. S., Aristegui, J., & Marañón, E. (2022). Phytoplankton responses to changing temperature and nutrient availability are consistent across the tropical and subtropical Atlantic. *Communications Biology*, 5(1), 1–13. <https://doi.org/10.1038/s42003-022-03971-z>

- Fisher, J. R. B., Acosta, E. A., Dennedy-Frank, P. J., Kroeger, T., & Boucher, T. M. (2018). Impact of satellite imagery spatial resolution on land use classification accuracy and modeled water quality. *Remote Sensing in Ecology and Conservation*, 4(2), 137–149. <https://doi.org/10.1002/rse2.61>
- Garg, V., Aggarwal, S. P., & Chauhan, P. (2020). Changes in turbidity along Ganga River using Sentinel-2 satellite data during lockdown associated with COVID-19. *Geomatics, Natural Hazards and Risk*, 11(1), 1175–1195. <https://doi.org/10.1080/19475705.2020.1782482>
- Garg, V., Senthil Kumar, A., Aggarwal, S. P., Kumar, V., Dhote, P. R., Thakur, P. K., Nikam, B. R., Sambare, R. S., Siddiqui, A., Muduli, P. R., & Rastogi, G. (2017). Spectral similarity approach for mapping turbidity of an inland waterbody. *Journal of Hydrology*, 550, 527–537. <https://doi.org/10.1016/j.jhydrol.2017.05.039>
- Gerardo, R., & de Lima, I. P. (2022). Assessing the potential of Sentinel-2 data for tracking invasive water hyacinth in a river branch. *Journal of Applied Remote Sensing*, 16(01). <https://doi.org/10.1117/1.jrs.16.014511>
- Getachew, B., & Manjunatha, B. R. (2022). Impacts of Land-Use Change on the Hydrology of Lake Tana Basin, Upper Blue Nile River Basin, Ethiopia. *Global Challenges*, 2200041, 1–13. <https://doi.org/10.1002/gch2.202200041>
- Gezie, A., Assefa, W. W., Getnet, B., Anteneh, W., Dejen, E., & Mereta, S. T. (2018). Potential impacts of water hyacinth invasion and management on water quality and human health in Lake Tana watershed, Northwest Ethiopia. *Biological Invasions*, 20(9), 2517–2534. <https://doi.org/10.1007/s10530-018-1717-0>
- Gholizadeh, M. H., Melesse, A. M., & Reddi, L. (2016). A comprehensive review on water quality parameters estimation using remote sensing techniques. *Sensors (Switzerland)*, 16(8). <https://doi.org/10.3390/s16081298>
- Ghoussein, Y., Nicolas, H., Haury, J., Fadel, A., Pichelin, P., Hamdan, H. A., & Faour, G. (2019). Multitemporal remote sensing based on an FVC reference period using sentinel-2 for monitoring Eichhornia crassipes on a Mediterranean river. *Remote Sensing*, 11(16). <https://doi.org/10.3390/rs11161856>

- Gibson, R., Danaher, T., Hehir, W., & Collins, L. (2020). A remote sensing approach to mapping fire severity in south-eastern Australia using sentinel 2 and random forest. *Remote Sensing of Environment*, 240(December 2019), 111702. <https://doi.org/10.1016/j.rse.2020.111702>
- Gidey, E., Dikinya, O., Sebego, R., Segosebe, E., & Zenebe, A. (2018). Analysis of the long-term agricultural drought onset, cessation, duration, frequency, severity and spatial extent using Vegetation Health Index (VHI) in Raya and its environs, Northern Ethiopia. *Environmental Systems Research*, 7(1). <https://doi.org/10.1186/s40068-018-0115-z>
- Gomes, L. C., & Miranda, L. E. (2001). Hydrologic and climatic regimes limit phytoplankton biomass in reservoirs of the Upper Paraná River Basin, Brazil. *Hydrobiologia*, 457, 205–214. <https://doi.org/10.1023/A:1012295901870>
- Gons, H. J., Rijkeboer, M., & Ruddick, K. G. (2002). A chlorophyll-retrieval algorithm for satellite imagery (Medium Resolution Imaging Spectrometer) of inland and coastal waters. *Journal of Plankton Research*, 24(9), 947–951. <https://doi.org/10.1093/plankt/24.9.947>
- Gorelick, N., Hancher, M., Dixon, M., Ilyushchenko, S., Thau, D., & Moore, R. (2017). Google Earth Engine: Planetary-scale geospatial analysis for everyone. *Remote Sensing of Environment*, 202, 18–27. <https://doi.org/10.1016/j.rse.2017.06.031>
- Goshu, G., Strokal, M., Kroeze, C., Koelmans, A. A., & de Klein, J. J. M. (2020). Assessing seasonal nitrogen export to large tropical lakes. *Science of the Total Environment*, 731, 139199. <https://doi.org/10.1016/j.scitotenv.2020.139199>
- Goshu, G., Tewabe, D., & Adugna, B. T. (2010). Spatial and temporal distribution of commercially important fish species of lake Tana, Ethiopia. *Ecohydrology and Hydrobiology*, 10(2–4), 231–240. <https://doi.org/10.2478/v10104-011-0008-5>
- Harun, I., Pushiri, H., Amirul-Aiman, A. J., & Zulkeflee, Z. (2021). Invasive water hyacinth: Ecology, impacts and prospects for the rural economy. *Plants*, 10(8). <https://doi.org/10.3390/plants10081613>
- Heath, R.G., Steynberg, M.C., Guglielmi, R., Maritz, A.L. (1998). The implications of

- point source phosphorus management to potable water treatment. *Water Science and Technology* 37(2): 343–350.
- Hill, M. P., & Coetzee, J. A. (2008). Integrated control of water hyacinth in Africa. *EPPO Bulletin*, 38(3), 452–457. <https://doi.org/10.1111/j.1365-2338.2008.01263.x>
- Hoshino, B., Abdelaziz Karamalla, M., Abd Elbasit, A. M., Manayeva, K., Yoda, K., Suliman, M., Elgamri, M., Nawata, H., & Yasuda, H. (2012). Evaluating the invasion strategic of Mesquite (*Prosopis juliflora*) in eastern Sudan using remotely sensed technique. *Journal of Arid Land Studies*, 22(1), 1–4.
http://nodaiweb.university.jp/desert/pdf/JALS-A01_1-4.pdf
- Hossain, A. K. M. A., Chao, X., & Jia, Y. (2010). Development of Remote Sensing Based Index for Estimating / Mapping Suspended Sediment Concentration in River and Lake Environments. *8th International Symposium on Ecohydraulics (ISE)*, September.
- Hossain, A. K. M. A., Mathias, C., & Blanton, R. (2021). Remote sensing of turbidity in the tennessee river using landsat 8 satellite. *Remote Sensing*, 13(18), 1–24.
<https://doi.org/10.3390/rs13183785>
- Huang, C., Davis, L. S., & Townshend, J. R. G. (2002). International Journal of Remote Sensing An assessment of support vector machines for land cover classification An assessment of support vector machines for land cover classification. *International Journal of Remote Sensing*, 23(4), 725–749.
<http://www.tandfonline.com/loi/tres20%5Cnhttp://dx.doi.org/10.1080/01431160110040323%5Cnhttp://www.tandfonline.com/page/terms-and-conditions>
- Hurskainen, P., Adhikari, H., Siljander, M., Pellikka, P. K. E., & Hemp, A. (2019). Auxiliary datasets improve the accuracy of object-based land use/land cover classification in heterogeneous savanna landscapes. *Remote Sensing of Environment*, 233(June), 111354. <https://doi.org/10.1016/j.rse.2019.111354>
- Iestyn Woolway, R., & Merchant, C. J. (2017). Amplified surface temperature response of cold, deep lakes to inter-annual air temperature variability. *Scientific Reports*, 7(1), 1–8. <https://doi.org/10.1038/s41598-017-04058-0>
- IvyPanda. (2019, July 19). How Does Water Hyacinth Harm the Local Ecosystem?

- <https://ivypanda.com/essays/how-does-water-hyacinth-harm-the-local-ecosystem/>
- Jafari, N. (2010). Ecology and Socio- economic utilization of water hyacinth (*Eichhornia crassipes* Mart Solms). *Appl.Sci.Environ. Manage.June 2010, 14*(June 2018), 43–49.
- Jalleta, A. K. (2021). The Legal Protection of Forests: Ethiopian Green Legacy vs. International Environmental Regimes. *Beijing Law Review, 12*(03), 725–749.
<https://doi.org/10.4236/blr.2021.123038>
- Jiménez-Rodríguez, C. D., Esquivel-Vargas, C., Coenders-Gerrits, M., & Sasa-Marín, M. (2019). Quantification of the evaporation rates from six types of wetland cover in Palo Verde National Park, Costa Rica. *Water (Switzerland), 11*(4).
<https://doi.org/10.3390/w11040674>
- Jin, Y., Liu, X., Chen, Y., & Liang, X. (2018). Land-cover mapping using Random Forest classification and incorporating NDVI time-series and texture: a case study of central Shandong. *International Journal of Remote Sensing, 39*(23), 8703–8723.
<https://doi.org/10.1080/01431161.2018.1490976>
- Jordan, C.F.(1969). Derivation of Leaf-Area Index from Quality of Light on the Forest Floor. *Ecology, 50*, 663–666.
- Jung, A. V., Cann, P. Le, Roig, B., Thomas, O., Baurès, E., & Thomas, M. F. (2014). Microbial contamination detection in water resources: Interest of current optical methods, trends and needs in the context of climate change. *International Journal of Environmental Research and Public Health, 11*(4), 4292–4310.
<https://doi.org/10.3390/ijerph110404292>
- Kaba, E., Philpot, W., & Steenhuis, T. (2014). Evaluating suitability of MODIS-terra images for reproducing historic sediment concentrations in water bodies: Lake Tana, Ethiopia. *International Journal of Applied Earth Observation and Geoinformation, 26*(1), 286–297. <https://doi.org/10.1016/j.jag.2013.08.001>
- Kamal, M., Jamaluddin, I., Parella, A., & Farda, N. M. (2020). Comparison of Google Earth Engine (GEE)-based machine learning classifiers for mangrove mapping. *40th Asian Conference on Remote Sensing, ACRS 2019: Progress of Remote Sensing Technology for Smart Future, January 2022*.

- Karim, D., Rachid, L., Mamourou, D., & Haiuml ssam, M. J. (2011). Production and oil-emulsion formulation of *Cadophora malorum* and *Alternaria jacinthicola*, two biocontrol agents against Water Hyacinth (*Eichhornia crassipes*). *African Journal of Microbiology Research*, 5(8), 924–929. <https://doi.org/10.5897/ajmr10.882>
- Kaushal, S. S., Likens, G. E., Jaworski, N. A., Pace, M. L., Sides, A. M., Seekell, D., Belt, K. T., Secor, D. H., & Wingate, R. L. (2010). Rising stream and river temperatures in the United States. *Frontiers in Ecology and the Environment*, 8(9), 461–466. <https://doi.org/10.1890/090037>
- Kayalik, M., & Çorumluoğlu, Ö. (2022). SST Correlation Between Chlorophyll and Turbidity by Landsat MS Image Analysis for the Coast of Izmir Province. *International Journal of Environment and Geoinformatics*, 9(4), 35–45. <https://doi.org/10.30897/ijgeo.1065482>
- Kebedew, M. G., Tilahun, S. A., Belete, M. A., Zimale, F. A., & Steenhuis, T. S. (2021). Sediment deposition (1940–2017) in a historically pristine lake in a rapidly developing tropical highland region in Ethiopia. *Earth Surface Processes and Landforms*, 46(8), 1521–1535. <https://doi.org/10.1002/esp.5118>
- Kebedew, M. G., Tilahun, S. A., Zimale, F. A., Belete, M. A., Wosenie, M. D., & Steenhuis, T. S. (2023). Relating Lake Circulation Patterns to Sediment, Nutrient, and Water Hyacinth Distribution in a Shallow Tropical Highland Lake. *Hydrology*, 10(9). <https://doi.org/10.3390/hydrology10090181>
- Kiage, L. M., & Obuoyo, J. (2011). The Potential Link Between El Nino and Water Hyacinth Blooms in Winam Gulf of Lake Victoria, East Africa: Evidence from Satellite Imagery. *Water Resources Management*, 25(14), 3931–3945. <https://doi.org/10.1007/s11269-011-9895-x>
- Kislik, C., Dronova, I., Grantham, T. E., & Kelly, M. (2022). Mapping algal bloom dynamics in small reservoirs using Sentinel-2 imagery in Google Earth Engine. *Ecological Indicators*, 140(May), 109041. <https://doi.org/10.1016/j.ecolind.2022.109041>
- Kiyemba, H., Barasa, B., Asaba, J., Makoba Gudoyi, P., & Akello, G. (2023). Water

- Hyacinth's Extent and Its Implication on Water Quality in Lake Victoria, Uganda. *Scientific World Journal*, 2023. <https://doi.org/10.1155/2023/4947272>
- Kleinschroth, F., Winton, R. S., Calamita, E., Niggemann, F., Botter, M., Wehrli, B., & Ghazoul, J. (2021). Living with floating vegetation invasions. *Ambio*, 50(1), 125–137. <https://doi.org/10.1007/s13280-020-01360-6>
- Kuhn, C., de Matos Valerio, A., Ward, N., Loken, L., Sawakuchi, H. O., Kampel, M., Richey, J., Stadler, P., Crawford, J., Striegl, R., Vermote, E., Pahlevan, N., & Butman, D. (2019). Performance of Landsat-8 and Sentinel-2 surface reflectance products for river remote sensing retrievals of chlorophyll-a and turbidity. *Remote Sensing of Environment*, 224(January), 104–118. <https://doi.org/10.1016/j.rse.2019.01.023>
- Kumar, S., & Deswal, S. (2020). Phytoremediation capabilities of *Salvinia molesta*, water hyacinth, water lettuce, and duckweed to reduce phosphorus in rice mill wastewater. *International Journal of Phytoremediation*, 22(11), 1097–1109. <https://doi.org/10.1080/15226514.2020.1731729>
- Lacaux, J. P., Tourre, Y. M., Vignolles, C., Ndione, J. A., & Lafaye, M. (2007). Classification of ponds from high-spatial resolution remote sensing: Application to Rift Valley Fever epidemics in Senegal. *Remote Sensing of Environment*, 106(1), 66–74. <https://doi.org/10.1016/j.rse.2006.07.012>
- Le, C., Li, Y., Zha, Y., Sun, D., Huang, C., & Lu, H. (2009). A four-band semi-analytical model for estimating chlorophyll a in highly turbid lakes: The case of Taihu Lake, China. *Remote Sensing of Environment*, 113(6), 1175–1182. <https://doi.org/10.1016/j.rse.2009.02.005>
- Lebeza, T. M., Gashaw, T., Tefera, G. W., & Mohammed, J. A. (2023). Trend analysis of hydro-climate variables in the Jemma sub-basin of Upper Blue Nile (Abbay) Basin, Ethiopia. *SN Applied Sciences*, 5(5). <https://doi.org/10.1007/s42452-023-05345-4>
- Lee, J. H. W., Hodgkiss, I. J., Wong, K. T. M., & Lam, I. H. Y. (2005). Real time observations of coastal algal blooms by an early warning system. *Estuarine, Coastal and Shelf Science*, 65(1–2), 172–190. <https://doi.org/10.1016/j.ecss.2005.06.005>
- Lee, S., Lee, S., Kim, S. H., Park, H., Park, S., & Yum, K. (2012). Examination of critical

- factors related to summer chlorophyll a concentration in the Sueo dam reservoir, Republic of Korea. *Environmental Engineering Science*, 29(6), 502–510.
<https://doi.org/10.1089/ees.2011.0070>
- Lei, S., Xu, J., Li, Y., Lyu, H., Liu, G., Zheng, Z., Xu, Y., Du, C., Zeng, S., Wang, H., Dong, X., Cai, X., & Li, J. (2020). Temporal and spatial distribution of Kd(490) and its response to precipitation and wind in lake Hongze based on MODIS data. *Ecological Indicators*, 108(August 2019), 105684.
<https://doi.org/10.1016/j.ecolind.2019.105684>
- Lemma, H., Admasu, T., Dessie, M., Fentie, D., Deckers, J., Frankl, A., Poesen, J., Adgo, E., & Nyssen, J. (2018). Revisiting lake sediment budgets: How the calculation of lake lifetime is strongly data and method dependent. *Earth Surface Processes and Landforms*, 43(3), 593–607. <https://doi.org/10.1002/esp.4256>
- Li, Y., Wang, X., Fu, W., Xia, X., Liu, C., Min, J., Zhang, W., & Crittenden, J. C. (2019). Interactions between nano/micro plastics and suspended sediment in water: Implications on aggregation and settling. *Water Research*, 161, 486–495.
<https://doi.org/10.1016/j.watres.2019.06.018>
- Liu, L., Guo, Y., Li, Y., Zhang, Q., Li, Z., Chen, E., Yang, L., & Mu, X. (2022). Comparison of Machine Learning Methods Applied on Multi-Source Medium-Resolution Satellite Images for Chinese Pine (*Pinus tabulaeformis*) Extraction on Google Earth Engine. *Forests*, 13(5). <https://doi.org/10.3390/f13050677>
- Lobo, F. de L., Nagel, G. W., Maciel, D. A., de Carvalho, L. A. S., Martins, V. S., Barbosa, C. C. F., & de Moraes Novo, E. M. L. (2021). Algaemap: Algae bloom monitoring application for inland waters in Latin America. *Remote Sensing*, 13(15).
<https://doi.org/10.3390/rs13152874>
- Lobo, F. L., Costa, M. P. F., & Novo, E. M. L. M. (2015). Time-series analysis of Landsat-MSS/TM/OLI images over Amazonian waters impacted by gold mining activities. *Remote Sensing of Environment*, 157, 170–184.
<https://doi.org/10.1016/j.rse.2014.04.030>
- Loukika, K. N., Keesara, V. R., & Sridhar, V. (2021). Analysis of land use and land cover

- using machine learning algorithms on google earth engine for Munneru river basin, India. *Sustainability (Switzerland)*, 13(24). <https://doi.org/10.3390/su132413758>
- Lu, B., Xu, Z., Li, J., & Chai, X. (2018). Removal of water nutrients by different aquatic plant species: An alternative way to remediate polluted rural rivers. *Ecological Engineering*, 110(October 2017), 18–26. <https://doi.org/10.1016/j.ecoleng.2017.09.016>
- Lu, J., Wu, J., Fu, Z., & Zhu, L. (2007). Water hyacinth in China: A sustainability science-based management framework. *Environmental Management*, 40(6), 823–830. <https://doi.org/10.1007/s00267-007-9003-4>
- Lymburner, L., Botha, E., Hestir, E., Anstee, J., Sagar, S., Dekker, A., & Malthus, T. (2016). Landsat 8: Providing continuity and increased precision for measuring multi-decadal time series of total suspended matter. *Remote Sensing of Environment*, 185, 108–118. <https://doi.org/10.1016/j.rse.2016.04.011>
- Makwinja, R., Inagaki, Y., Sagawa, T., Obubu, J. P., Habineza, E., & Haaziye, W. (2023). Monitoring trophic status using in situ data and Sentinel-2 MSI algorithm: lesson from Lake Malombe, Malawi. *Environmental Science and Pollution Research*, 30(11), 29755–29772. <https://doi.org/10.1007/s11356-022-24288-8>
- Mann HB (1945) Nonparametric Tests Against Trend. *Econometrica* 13: 245. <https://doi.org/10.2307/1907187>
- Masocha, M., Dube, T., Nhwatiwa, T., & Choruma, D. (2018). Testing utility of Landsat 8 for remote assessment of water quality in two subtropical African reservoirs with contrasting trophic states. *Geocarto International*, 33(7), 667–680. <https://doi.org/10.1080/10106049.2017.1289561>
- Matos, T., Martins, M. S., Henriques, R., & Goncalves, L. M. (2024). A review of methods and instruments to monitor turbidity and suspended sediment concentration. *Journal of Water Process Engineering*, 64(June), 105624. <https://doi.org/10.1016/j.jwpe.2024.105624>
- Matthew Cock. (2001). Problems Caused by Water Hyacinth as an Invasive Alien Species. *Invasive Alien Species: A Toolkit of Best Prevention and Management Practices*, 171.

- Maylani, E. D., Yuniati, R., & Wardhana, W. (2020). The Effect of leaf surface character on the ability of water hyacinth, *Eichhornia crassipes* (Mart.) Solms. To transpire water. *IOP Conference Series: Materials Science and Engineering*, 902(1).
<https://doi.org/10.1088/1757-899X/902/1/012070>
- Mazhar, N., Javid, K., Nawaz Akram, M. A., Afzal, A., Hamayon, K., & Ahmad, A. (2022). Index-Based Spatiotemporal Assesment of Water Quality in Tarbela Reservoir, Pakistan (1990–2020). *Geography, Environment, Sustainability*, 15(4), 232–242. <https://doi.org/10.24057/2071-9388-2022-077>
- McCartney, M. P., Alemayehu, T., Awulachew, S. B., & Seleshi, Y. (2010). Evaluation of current and future water resource development in the Blue Nile. In *IWMI RR, forthcoming*.
- McFeeters, S. K. (1996). The use of the Normalized Difference Water Index (NDWI) in the delineation of open water features. *International Journal of Remote Sensing*, 17(7), 1425–1432. <https://doi.org/10.1080/01431169608948714>
- Meerhoff, M., Mazzeo, N., Moss, B., & Rodríguez-Gallego, L. (2003). The structuring role of free-floating versus submerged plants in a subtropical shallow lake. *Aquatic Ecology*, 37(4), 377–391. <https://doi.org/10.1023/B:AECO.00000007041.57843.0b>
- Mekonnen, M. (2021). Impacts of soil and water conservation practices after half of a generation age, northwest highlands of Ethiopia. *Soil and Tillage Research*, 205(August 2020), 104755. <https://doi.org/10.1016/j.still.2020.104755>
- Minale, A. S., & Belete, W. (2017). *Land Use Distribution and Change in Lake Tana Sub Basin*. 357–373. https://doi.org/10.1007/978-3-319-45755-0_22
- Mironga, J. M., Mathooko, J. M., & Onywere, S. M. (2011). The Effect of Water Hyacinth (*Eichhornia Crassipes*) Infestation on Phytoplankton Productivity in Lake Naivasha and the Status of Control. *Journal of Environmental Science and Engineering*, 5, 1252–1260.
- Mishra, S., & Mishra, D. R. (2012). Normalized difference chlorophyll index: A novel model for remote estimation of chlorophyll-a concentration in turbid productive waters. *Remote Sensing of Environment*, 117, 394–406.

<https://doi.org/10.1016/j.rse.2011.10.016>

Moges, M. A., Schmitter, P., Tilahun, S. A., Ayana, E. K., Ketema, A. A., Nigussie, T. E., & Steenhuis, T. S. (2017). Water Quality Assessment by Measuring and Using Landsat 7 ETM+ Images for the Current and Previous Trend Perspective: Lake Tana Ethiopia. *Journal of Water Resource and Protection*, 09(12), 1564–1585.

<https://doi.org/10.4236/jwarp.2017.912099>

Molinos, J. G., Viana, M., Brennan, M., & Donohue, I. (2015). Importance of long-term cycles for predicting water level dynamics in natural lakes. *PLoS ONE*, 10(3), 1–12.

<https://doi.org/10.1371/journal.pone.0119253>

Moses, W. J., Gitelson, A. A., Berdnikov, S., & Povazhnyy, V. (2009). Satellite estimation of chlorophyll-a concentration using the red and NIR bands of MERIS The azov sea case study. *IEEE Geoscience and Remote Sensing Letters*, 6(4), 845–849.

<https://doi.org/10.1109/LGRS.2009.2026657>

Mucheye, T., Haro, S., Papaspyrou, S., & Caballero, I. (2022). Water Quality and Water Hyacinth Monitoring with the Sentinel-2A/B Satellites in Lake Tana (Ethiopia). *Remote Sensing*, 14(19), 1–17. <https://doi.org/10.3390/rs14194921>

Mukarugwiro, J. A., Newete, S. W., Adam, E., Nsanganwimana, F., Abutaleb, K. A., & Byrne, M. J. (2019). Mapping distribution of water hyacinth (*Eichhornia crassipes*) in Rwanda using multispectral remote sensing imagery. *African Journal of Aquatic Science*, 44(4), 339–348. <https://doi.org/10.2989/16085914.2019.1650712>

Mukarugwiro, J. A., Newete, S. W., Adam, E., Nsanganwimana, F., Abutaleb, K., & Byrne, M. J. (2021). Mapping spatio-temporal variations in water hyacinth (*Eichhornia crassipes*) coverage on Rwandan water bodies using multispectral imageries. *International Journal of Environmental Science and Technology*, 18(2), 275–286.

<https://doi.org/10.1007/s13762-020-02824-8>

Mushtaq, F., Ahmed, P., & Nee Lala, M. G. (2021). Spatiotemporal change in the surface temperature of Himalayan lake and its inter-relation with water quality and growth in aquatic vegetation. *Geocarto International*, 36(3), 241–261.

<https://doi.org/10.1080/10106049.2019.1590467>

- Nash, D. A. H., Abdullah, S. R. S., Hasan, H. A., Idris, M., Muhammad, N. F., Al-Baldawi, I. A., & Ismail, N. I. (2019). Phytoremediation of nutrients and organic carbon from sago mill effluent using water hyacinth (*Eichhornia crassipes*). *Journal of Engineering and Technological Sciences*, 51(4), 573–584.
<https://doi.org/10.5614/j.eng.technol.sci.2019.51.4.8>
- Nasiri, V., Deljouei, A., Moradi, F., Sadeghi, S., & Borz, S. (2022). Land Use and Land Cover Mapping Using Sentinel-2 , Landsat-8 Two Composition Methods. *Remote Sensing*, 14(9), 1977.
- Nechad, B., Ruddick, K. G., & Park, Y. (2010). Calibration and validation of a generic multisensor algorithm for mapping of total suspended matter in turbid waters. *Remote Sensing of Environment*, 114(4), 854–866. <https://doi.org/10.1016/j.rse.2009.11.022>
- NourEldeen, N., Mao, K., Yuan, Z., Shen, X., Xu, T., & Qin, Z. (2020). Analysis of the spatiotemporal change in land surface temperature for a long-term sequence in Africa (2003-2017). *Remote Sensing*, 12(3). <https://doi.org/10.3390/rs12030488>
- Nurhusein, M. M. (2020). Water Consumption by Hydropower, Does It Worth Allocation under Ethiopian Context. *Journal of Water Resource and Protection*, 12(03), 183–202.
<https://doi.org/10.4236/jwarp.2020.123012>
- Odermatt, D., Danne, O., Philipson, P., & Brockmann, C. (2018). Diversity II water quality parameters from ENVISAT (2002-2012): A new global information source for lakes. *Earth System Science Data*, 10(3), 1527–1549. <https://doi.org/10.5194/essd-10-1527-2018>
- Oliveira-Junior, E. S., Tang, Y., van den Berg, S. J. P., Cardoso, S. J., Lamers, L. P. M., & Kosten, S. (2018). The impact of water hyacinth (*Eichhornia crassipes*) on greenhouse gas emission and nutrient mobilization depends on rooting and plant coverage. *Aquatic Botany*, 145(November 2017), 1–9. <https://doi.org/10.1016/j.aquabot.2017.11.005>
- Oommen, T., Misra, D., Twarakavi, N. K. C., Prakash, A., Sahoo, B., & Bandopadhyay, S. (2008). An objective analysis of support vector machine based classification for remote sensing. *Mathematical Geosciences*, 40(4), 409–424.
<https://doi.org/10.1007/s11004-008-9156-6>

- Ongore, C. O., Aura, C. M., Ogari, Z., Njiru, J. M., & Nyamweya, C. S. (2018). Spatial-temporal dynamics of water hyacinth, *Eichhornia crassipes* (Mart.) and other macrophytes and their impact on fisheries in Lake Victoria, Kenya. *Journal of Great Lakes Research*, 44(6), 1273–1280. <https://doi.org/10.1016/j.jglr.2018.10.001>
- Ouma, Y. O., Noor, K., & Herbert, K. (2020). Modelling Reservoir Chlorophyll- a, TSS, and Turbidity Using Sentinel-2A MSI and Landsat-8 OLI Satellite Sensors with Empirical Multivariate Regression. *Journal of Sensors*, 2020. <https://doi.org/10.1155/2020/8858408>
- Paaijmans, K. P., Takken, W., Githeko, A. K., & Jacobs, A. F. G. (2008). The effect of water turbidity on the near-surface water temperature of larval habitats of the malaria mosquito *Anopheles gambiae*. *International Journal of Biometeorology*, 52(8), 747–753. <https://doi.org/10.1007/s00484-008-0167-2>
- Pádua, L., Antão-Geraldes, A. M., Sousa, J. J., Rodrigues, M. Â., Oliveira, V., Santos, D., Miguens, M. F. P., & Castro, J. P. (2022). Water Hyacinth (*Eichhornia crassipes*) Detection Using Coarse and High Resolution Multispectral Data. *Drones*, 6(2), 1–14. <https://doi.org/10.3390/drones6020047>
- Page, B. P., Kumar, A., & Mishra, D. R. (2018). A novel cross-satellite based assessment of the spatio-temporal development of a cyanobacterial harmful algal bloom. *International Journal of Applied Earth Observation and Geoinformation*, 66(June 2017), 69–81. <https://doi.org/10.1016/j.jag.2017.11.003>
- Pahlevan, N., Chittimalli, S. K., Balasubramanian, S. V., & Vellucci, V. (2019). Sentinel-2/Landsat-8 product consistency and implications for monitoring aquatic systems. *Remote Sensing of Environment*, 220(October 2018), 19–29. <https://doi.org/10.1016/j.rse.2018.10.027>
- Pahlevan, N., Mangin, A., Balasubramanian, S. V., Smith, B., Alikas, K., Arai, K., Barbosa, C., Bélanger, S., Binding, C., Bresciani, M., Giardino, C., Gurlin, D., Fan, Y., Harmel, T., Hunter, P., Ishikawa, J., Kratzer, S., Lehmann, M. K., Ligi, M., ... Warren, M. (2021). ACIX-Aqua: A global assessment of atmospheric correction methods for Landsat-8 and Sentinel-2 over lakes, rivers, and coastal waters. *Remote*

- Sensing of Environment*, 258(August 2020). <https://doi.org/10.1016/j.rse.2021.112366>
- Pahlevan, N., Smith, B., Alikas, K., Anstee, J., Barbosa, C., Binding, C., Bresciani, M., Cremella, B., Giardino, C., Gurlin, D., Fernandez, V., Jamet, C., Kangro, K., Lehmann, M. K., Loisel, H., Matsushita, B., Hà, N., Olmanson, L., Potvin, G., ... Ruiz-Verdù, A. (2022). Simultaneous retrieval of selected optical water quality indicators from Landsat-8, Sentinel-2, and Sentinel-3. *Remote Sensing of Environment*, 270. <https://doi.org/10.1016/j.rse.2021.112860>
- Pahlevan, N., Smith, B., Schalles, J., Binding, C., Cao, Z., Ma, R., Alikas, K., Kangro, K., Gurlin, D., Hà, N., Matsushita, B., Moses, W., Greb, S., Lehmann, M. K., Ondrusek, M., Oppelt, N., & Stumpf, R. (2020). Seamless retrievals of chlorophyll-a from Sentinel-2 (MSI) and Sentinel-3 (OLCI) in inland and coastal waters: A machine-learning approach. *Remote Sensing of Environment*, 240(August 2019), 111604. <https://doi.org/10.1016/j.rse.2019.111604>
- Park, J., & Richard, J. (2020). The effect of floating plant on water purification: Comparison of the water purification capability of Water Hyacinth, Duckweed, and Azolla. *Journal of Emerging Investigators*, 1–8. <https://doi.org/10.59720/20-125>
- Pastagia, J., & Mehta, D. (2022). Application of innovative trend analysis on rainfall time series over Rajsamand district of Rajasthan state. *Water Supply*, 22(9), 7189–7196. <https://doi.org/10.2166/ws.2022.276>
- Patra, P. P., Dubey, S. K., Trivedi, R. K., Sahu, S. K., & Rout, S. K. (2017). Estimation of chlorophyll-a concentration and trophic states in Nalban Lake of East Kolkata Wetland, India from Landsat 8 OLI data. *Spatial Information Research*, 25(1), 75–87. <https://doi.org/10.1007/s41324-016-0069-z>
- Penatti, N. C., Almeida, T. I. R. de, Ferreira, L. G., Arantes, A. E., & Coe, M. T. (2015). Satellite-based hydrological dynamics of the world's largest continuous wetland. *Remote Sensing of Environment*, 170, 1–13. <https://doi.org/10.1016/j.rse.2015.08.031>
- Perna, C., & Burrows, D. (2005). Improved dissolved oxygen status following removal of exotic weed mats in important fish habitat lagoons of the tropical Burdekin River floodplain, Australia. *Marine Pollution Bulletin*, 51(1–4), 138–148.

<https://doi.org/10.1016/j.marpolbul.2004.10.050>

- Pham, T. D., Yokoya, N., Xia, J., Ha, N. T., Le, N. N., Nguyen, T. T. T., Dao, T. H., Vu, T. T. P., Pham, T. D., & Takeuchi, W. (2020). Comparison of machine learning methods for estimating mangrove above-ground biomass using multiple source remote sensing data in the red river delta biosphere reserve, Vietnam. *Remote Sensing*, 12(8), 1–24. <https://doi.org/10.3390/RS12081334>
- Pompapathi, V. Ashwin Gujrati, Shard Chander, & H. A. Solanki. (2022). Spatio-temporal variability of Turbidity over Ukai Reservoir, by using RS2/R2A LISS III Satellite datasets. *International Journal of Scientific Research in Science and Technology*, June, 377–386. <https://doi.org/10.32628/ijrst229381>
- Qian, X., Liang, L., Shen, Q., Sun, Q., Zhang, L., Liu, Z., Zhao, S., & Qin, Z. (2016). Drought trends based on the VCI and its correlation with climate factors in the agricultural areas of China from 1982 to 2010. *Environmental Monitoring and Assessment*, 188(11). <https://doi.org/10.1007/s10661-016-5657-9>
- Rajendran, S., Al-Naimi, N., Al Khayat, J. A., Sorino, C. F., Sadooni, F. N., & Al Saad Al Kuwari, H. (2022). Chlorophyll-a concentrations in the Arabian Gulf waters of arid region: A case study from the northern coast of Qatar. *Regional Studies in Marine Science*, 56, 102680. <https://doi.org/10.1016/j.rsma.2022.102680>
- Rashed, A. A. (2014). Assessment of aquatic plants evapotranspiration for secondary agriculture drains (case study: Edfina drain, Egypt). *Egyptian Journal of Aquatic Research*, 40(2), 117–124. <https://doi.org/10.1016/j.ejar.2014.07.001>
- Reinart, A., & Reinhold, M. (2008). Mapping surface temperature in large lakes with MODIS data. *Remote Sensing of Environment*, 112(2), 603–611. <https://doi.org/10.1016/j.rse.2007.05.015>
- Ritchie, J. C., Zimba, P. V., & Everitt, J. H. (2003). Remote sensing techniques to assess water quality. *Photogrammetric Engineering and Remote Sensing*, 69(6), 695–704. <https://doi.org/10.14358/PERS.69.6.695>
- Robles, W., Madsen, J. D., & Wersal, R. M. (2015). Estimating the Biomass of Waterhyacinth (*Eichhornia crassipes*) Using the Normalized Difference Vegetation

- Index Derived from Simulated Landsat 5 TM . *Invasive Plant Science and Management*, 8(2), 203–211. <https://doi.org/10.1614/ipsm-d-14-00033.1>
- Rodríguez, M., Brisson, J., Rueda, G., & Rodríguez, M. S. (2012). Water Quality Improvement of a Reservoir Invaded by an Exotic Macrophyte. *Invasive Plant Science and Management*, 5(2), 290–299. <https://doi.org/10.1614/ipsm-d-11-00023.1>
- Rouse, W. R., Oswald, C. J., Binyamin, J., Spence, C., Schertzer, W. M., Blanken, P. D., Bussi eres, N., & Duguay, C. R. (2005). The role of northern lakes in a regional energy balance. *Journal of Hydrometeorology*, 6(3), 291–305. <https://doi.org/10.1175/JHM421.1>
- Saraswati, A. W. (2022). Water Hyacinth Pros and Cons For Waters Ecosystem. Greeneration Foundation. <https://greeneration.org/en/publication/green-info/water-hyacinth-pros-and-cons-for-waters-ecosystem/>
- Saha, P., Shinde, O., & Sarkar, S. (2017). Phytoremediation of industrial mines wastewater using water hyacinth. *International Journal of Phytoremediation*, 19(1), 87–96. <https://doi.org/10.1080/15226514.2016.1216078>
- Sasaqi, D., Pranoto, P., & Setyono, P. (2019). Estimation of Water Losses Through Evapotranspiration of Water Hyacinth (*Eichhornia crassipes*). *Caraka Tani: Journal of Sustainable Agriculture*, 34(1), 86. <https://doi.org/10.20961/carakatani.v34i1.28214>
- Scheffer, M. (1999). The effect of aquatic vegetation on turbidity; how important are the filter feeders? *Hydrobiologia*, 408–409, 307–316. https://doi.org/10.1007/978-94-017-2986-4_34
- Schneider, P., Hook, S. J., Radocinski, R. G., Corlett, G. K., Hulley, G. C., Schladow, S. G., & Steissberg, T. E. (2009). Satellite observations indicate rapid warming trend for lakes in California and Nevada. *Geophysical Research Letters*, 36(22), 1–6. <https://doi.org/10.1029/2009GL040846>
- Sebasti a-Frasquet, M. T., Aguilar-Maldonado, J. A., Santamar a-Del  ngel, E., & Estornell, J. (2019). Sentinel 2 analysis of turbidity patterns in a coastal lagoon. *Remote Sensing*, 11(24), 1–17. <https://doi.org/10.3390/rs11242926>
- Sen, P.K. (1968) Estimates of the Regression Coefficient Based on Kendall’s Tau. *J Am*

- Stat Assoc 63: 1379– 1389. <https://doi.org/10.1080/01621459.1968.10480934>
- Şen, Z. (2012) Innovative Trend Analysis Methodology. *J Hydrol Eng* 17:1042–1046. [https://doi.org/10.1061/\(asce\)he.1943-5584.0000556](https://doi.org/10.1061/(asce)he.1943-5584.0000556)
- Setegn, S.G.; Srinivasan, R.; Dargahi, B.; Melesse, A.M. (2009). Spatial delineation of soil erosion vulnerability in the Lake Tana Basin, Ethiopia. *Hydrol Process* 2274, 2267–2274.
- Sewak, M., Sahay, S. K., & Rathore, H. (2018). Comparison of deep learning and the classical machine learning algorithm for the malware detection. *Proceedings - 2018 IEEE/ACIS 19th International Conference on Software Engineering, Artificial Intelligence, Networking and Parallel/Distributed Computing, SNPD 2018, July*, 293–296. <https://doi.org/10.1109/SNPD.2018.8441123>
- Shao, Y., & Lunetta, R. S. (2012). Comparison of support vector machine, neural network, and CART algorithms for the land-cover classification using limited training data points. *ISPRS Journal of Photogrammetry and Remote Sensing*, 70, 78–87. <https://doi.org/10.1016/j.isprsjprs.2012.04.001>
- Sharma, S., Gray, D. K., Read, J. S., O'Reilly, C. M., Schneider, P., Qudrat, A., Gries, C., Stefanoff, S., Hampton, S. E., Hook, S., Lenters, J. D., Livingstone, D. M., McIntyre, P. B., Adrian, R., Allan, M. G., Anneville, O., Arvola, L., Austin, J., Bailey, J., ... Woo, K. H. (2015). A global database of lake surface temperatures collected by in situ and satellite methods from 1985-2009. *Scientific Data*, 2, 1–19. <https://doi.org/10.1038/sdata.2015.8>
- Shekede, M. D., Kusangaya, S., & Schmidt, K. (2008). Spatio-temporal variations of aquatic weeds abundance and coverage in Lake Chivero, Zimbabwe. *Physics and Chemistry of the Earth*, 33(8–13), 714–721. <https://doi.org/10.1016/j.pce.2008.06.052>
- Shetty, S. (2019). *Analysis of Machine Learning Classifiers for LULC Classification on Google Earth Engine*. 8(23), 1–22.
- Shetty, S., Gupta, P. K., Belgiu, M., & Srivastav, S. K. (2021). Assessing the effect of training sampling design on the performance of machine learning classifiers for land cover mapping using multi-temporal remote sensing data and google earth engine.

- Remote Sensing*, 13(8). <https://doi.org/10.3390/rs13081433>
- Sheykhoumou, M., Mahdianpari, M., Ghanbari, H., Mohammadimanesh, F., Ghamisi, P., & Homayouni, S. (2020). Support Vector Machine Versus Random Forest for Remote Sensing Image Classification: A Meta-Analysis and Systematic Review. *IEEE Journal of Selected Topics in Applied Earth Observations and Remote Sensing*, 13, 6308–6325. <https://doi.org/10.1109/JSTARS.2020.3026724>
- Shi, K., Zhang, Y., Li, Y., Li, L., Lv, H., & Liu, X. (2015). Remote estimation of cyanobacteria-dominance in inland waters. *Water Research*, 68, 217–226. <https://doi.org/10.1016/j.watres.2014.10.019>
- Siddiqui, A., Kushwaha, G., Nikam, B., Srivastav, S. K., Shelar, A., & Kumar, P. (2021). Analysing the day/night seasonal and annual changes and trends in land surface temperature and surface urban heat island intensity (SUHI) for Indian cities. *Sustainable Cities and Society*, 75(September), 103374. <https://doi.org/10.1016/j.scs.2021.103374>
- Silva, L. I. da, & Baptista, G. M. de M. (2023). Determination of the critical threshold for the occurrence of fires in the Parque Nacional de Brasília (Brazil) through temporal analysis using spectral indices. *Sociedade & Natureza*, 1–18. <https://doi.org/10.14393/sn-v35-2023-67446x>
- Sima, S., Ahmadali-pour, A., & Tajrishy, M. (2013). Mapping surface temperature in a hyper-saline lake and investigating the effect of temperature distribution on the lake evaporation. *Remote Sensing of Environment*, 136, 374–385. <https://doi.org/10.1016/j.rse.2013.05.014>
- Singh, G., Reynolds, C., Byrne, M., & Rosman, B. (2020). A remote sensing method to monitor water, aquatic vegetation, and invasive water hyacinth at national extents. *Remote Sensing*, 12(24), 1–24. <https://doi.org/10.3390/rs12244021>
- Smith, V. H., Sieber-Denlinger, J., deNoyelles, F., Campbell, S., Pan, S., Randtke, S. J., Blain, G. T., & Strasser, V. A. (2002). Managing taste and odor problems in a eutrophic drinking water reservoir. *Lake and Reservoir Management*, 18(4), 319–323. <https://doi.org/10.1080/07438140209353938>

- Song, K., Wang, M., Du, J., Yuan, Y., Ma, J., Wang, M., & Mu, G. (2016). Spatiotemporal variations of lake surface temperature across the Tibetan Plateau using MODIS LST product. *Remote Sensing*, 8(10). <https://doi.org/10.3390/rs8100854>
- Sun, Z., Xu, R., Du, W., Wang, L., & Lu, D. (2019). High-resolution urban land mapping in China from sentinel 1A/2 imagery based on Google Earth Engine. *Remote Sensing*, 11(7), 1–22. <https://doi.org/10.3390/rs11070752>
- Takamura, N., Kadono, Y., Fukushima, M., Nakagawa, M., & Kim, B. H. O. (2003). Effects of aquatic macrophytes on water quality and phytoplankton communities in shallow lakes. *Ecological Research*, 18(4), 381–395. <https://doi.org/10.1046/j.1440-1703.2003.00563.x>
- Tauchnitz, N., Kurzius, F., Rupp, H., Schmidt, G., Hauser, B., Schrödter, M., & Meissner, R. (2020). Assessment of pesticide inputs into surface waters by agricultural and urban sources - A case study in the Querne/Weida catchment, central Germany. *Environmental Pollution*, 267. <https://doi.org/10.1016/j.envpol.2020.115186>
- Tavares, M. H., Cunha, A. H. F., Motta-Marques, D., Ruhoff, A. L., Cavalcanti, J. R., Fragoso, C. R., Bravo, J. M., Munar, A. M., Fan, F. M., & Rodrigues, L. H. R. (2019). Comparison of methods to estimate lake-surface-water temperature using landsat 7 ETM+ and MODIS imagery: Case study of a large shallow subtropical lake in Southern Brazil. *Water (Switzerland)*, 11(1), 1–21. <https://doi.org/10.3390/w11010168>
- Téllez, T. R., López, E. M. de R., Granado, G. L., Pérez, E. A., López, R. M., & Guzmán, J. M. S. (2008). The water hyacinth, *Eichhornia crassipes*: An invasive plant in the Guadiana River Basin (Spain). *Aquatic Invasions*, 3(1), 42–53. <https://doi.org/10.3391/ai.2008.3.1.8>
- Teshome, H., & Amente, G. (2022). *Estimation of Water Losses by Transpiration from Root and Leaf Clipped Eich- hornia Crassipes (Water Hyacinth) College of Natural and Computational Sciences , Haramaya University , Dire Dawa , Ethio-. 5(2).*
- Tewabe, D., & Fentahun, T. (2020). Assessing land use and land cover change detection using remote sensing in the Lake Tana Basin, Northwest Ethiopia. *Cogent Environmental Science*, 6(1). <https://doi.org/10.1080/23311843.2020.1778998>

- Thamaga, K. H., & Dube, T. (2018). Remote sensing of invasive water hyacinth (*Eichhornia crassipes*): A review on applications and challenges. *Remote Sensing Applications: Society and Environment*, 10, 36–46.
<https://doi.org/10.1016/j.rsase.2018.02.005>
- Thamaga, K. H., & Dube, T. (2019). Understanding seasonal dynamics of invasive water hyacinth (*Eichhornia crassipes*) in the Greater Letaba river system using Sentinel-2 satellite data. *GIScience and Remote Sensing*, 56(8), 1355–1377.
<https://doi.org/10.1080/15481603.2019.1646988>
- Thi Nguyen, T. H., Boets, P., Lock, K., Damanik Ambarita, M. N., Forio, M. A. E., Sasha, P., Dominguez-Granda, L. E., Thi Hoang, T. H., Everaert, G., & Goethals, P. L. M. (2015). Habitat suitability of the invasive water hyacinth and its relation to water quality and macroinvertebrate diversity in a tropical reservoir. *Limnologica*, 52, 67–74. <https://doi.org/10.1016/j.limno.2015.03.006>
- Thomas, L.; Ralph, W.; Kiefer, J.C.(2004). Remote Sensing and Image Interpretation (Fifth Edition). *Geogr. J.*, 146, 448–449.
- Tibebe, D., Kassa, Y., Melaku, A., & Lakew, S. (2019). Investigation of spatio-temporal variations of selected water quality parameters and trophic status of Lake Tana for sustainable management, Ethiopia. *Microchemical Journal*, 148(April), 374–384.
<https://doi.org/10.1016/j.microc.2019.04.085>
- Timmer, C.E. & Weldon. L.W. (1966). Evapotranspiration and pollution of water by water hyacinth. In *Hyacinth Control Journal* (Vol. 6, pp. 34–37).
<http://www.apms.org/japm/vol06/v6p34.pdf>
- Ting, W. H. T., Tan, I. A. W., Salleh, S. F., & Wahab, N. A. (2018). Application of water hyacinth (*Eichhornia crassipes*) for phytoremediation of ammoniacal nitrogen: A review. *Journal of Water Process Engineering*, 22(February), 239–249.
<https://doi.org/10.1016/j.jwpe.2018.02.011>
- Tobias, V. D., Conrad, J. L., Mahardja, B., & Khanna, S. (2019). Impacts of water hyacinth treatment on water quality in a tidal estuarine environment. *Biological Invasions*, 21(12), 3479–3490. <https://doi.org/10.1007/s10530-019-02061-2>

- Toft, J. D., Simenstad, C. A., Cordell, J. R., & Grimaldo, L. F. (2003). The effects of introduced water hyacinth on habitat structure, invertebrate assemblages, and fish diets. *Estuaries*, 26(3), 746–758. <https://doi.org/10.1007/BF02711985>
- Trumpickas, J., Shuter, B. J., & Minns, C. K. (2009). Forecasting impacts of climate change on Great Lakes surface water temperatures. *Journal of Great Lakes Research*, 35(3), 454–463. <https://doi.org/10.1016/j.jglr.2009.04.005>
- Tucker, C. J. (1979). Red and photographic infrared linear combinations for monitoring vegetation. *Remote Sensing of Environment*, 8(2), 127–150. [https://doi.org/10.1016/0034-4257\(79\)90013-0](https://doi.org/10.1016/0034-4257(79)90013-0)
- Tzortziou, M., Subramaniam, A., Herman, J. R., Gallegos, C. L., Neale, P. J., & Harding, L. W. (2007). Remote sensing reflectance and inherent optical properties in the mid Chesapeake Bay. *Estuarine, Coastal and Shelf Science*, 72(1–2), 16–32. <https://doi.org/10.1016/j.ecss.2006.09.018>
- Van Der Weert, R., & Kamerling, G. E. (1974). Evapotranspiration of water hyacinth (*Eichhornia crassipes*). *Journal of Hydrology*, 22(3–4), 201–212. [https://doi.org/10.1016/0022-1694\(74\)90075-4](https://doi.org/10.1016/0022-1694(74)90075-4)
- Vasistha, P., & Ganguly, R. (2020). Water quality assessment of natural lakes and its importance: An overview. *Materials Today: Proceedings*, 32(xxxx), 544–552. <https://doi.org/10.1016/j.matpr.2020.02.092>
- Verma, R., Singh, S. P., & Ganesha Raj, K. (2003). Assessment of changes in water-hyacinth coverage of water bodies in northern part of Bangalore city using temporal remote sensing data. *Current Science*, 84(6), 795–804.
- Villamagna, A. M., & Murphy, B. R. (2010). Ecological and socio-economic impacts of invasive water hyacinth (*Eichhornia crassipes*): A review. *Freshwater Biology*, 55(2), 282–298. <https://doi.org/10.1111/j.1365-2427.2009.02294.x>
- Wan, Z., Zhang, Y., Zhang, Q., & Li, Z. liang. (2002). Validation of the land-surface temperature products retrieved from terra moderate resolution imaging spectroradiometer data. *Remote Sensing of Environment*, 83(1–2), 163–180. [https://doi.org/10.1016/S0034-4257\(02\)00093-7](https://doi.org/10.1016/S0034-4257(02)00093-7)

- Wang, J., & Chen, X. (2024). A new approach to quantify chlorophyll-a over inland water targets based on multi-source remote sensing data. *Science of the Total Environment*, 906(July 2023), 167631. <https://doi.org/10.1016/j.scitotenv.2023.167631>
- Wang, J., & Seyed-Yagoobi, J. (1994). Effects of water turbidity and salt concentration levels on penetration of solar radiation under water. *Solar Energy*, 52(5), 429–438. [https://doi.org/10.1016/0038-092X\(94\)90120-Q](https://doi.org/10.1016/0038-092X(94)90120-Q)
- Wang, X., Shi, K., Zhang, Y., Qin, B., Zhang, Y., Wang, W., Woolway, R. I., Piao, S., & Jeppesen, E. (2023). Climate change drives rapid warming and increasing heatwaves of lakes. *Science Bulletin*, 68(14), 1574–1584. <https://doi.org/10.1016/j.scib.2023.06.028>
- Wang, Y., Xu, Y., Tabari, H., Wang, J., Wang, Q., Song, S., & Hu, Z. (2020). Innovative trend analysis of annual and seasonal rainfall in the Yangtze River Delta, eastern China. *Atmospheric Research*, 231(37), 104673. <https://doi.org/10.1016/j.atmosres.2019.104673>
- Wassie Anteneh, Minwuyelet Mengist, Ayalew Wondie, Dereje Tewabe, Woldegebrael W/Kidan, A. A. and W. E. (2014). (2014). Water hyacinth coverage survey report on lake tana; Technical report series 1. *Technical Report Series 1*, 1–29.
- Wilson, J. R., Holst, N., & Rees, M. (2005). Determinants and patterns of population growth in water hyacinth. *Aquatic Botany*, 81(1), 51–67. <https://doi.org/10.1016/j.aquabot.2004.11.002>
- Wloczyk, C., Richter, R., Borg, E., & Neubert, W. (2006). Sea and lake surface temperature retrieval from Landsat thermal data in Northern Germany. *International Journal of Remote Sensing*, 27(12), 2489–2502. <https://doi.org/10.1080/01431160500300206>
- Womber, R. Z., Atanaw, F., & Kebedew, G. M. (2022). Assessment of Spatiotemporal Variation of Water Quality of Lake Tana, Ethiopia. *Poly Journal of Engineering and Technology*, January 2023, 1–21. <https://doi.org/10.20372/pjet.v1i1.1271>
- Wondie, A., Mengistu, S., Vijverberg, J., & Dejen, E. (2007). Seasonal variation in primary production of a large high altitude tropical lake (Lake Tana, Ethiopia): Effects of nutrient availability and water transparency. *Aquatic Ecology*, 41(2), 195–207.

<https://doi.org/10.1007/s10452-007-9080-8>

- Wondie A, Seid A, Molla E, Goshu G (2012). Preliminary assessment of water hyacinth (*Eichornia crassipes*) in Lake Tana. Proceedings of the National Workshop (Biological Society of Ethiopia), Addis Ababa, Ethiopia
- Worqlul, A. W., Ayana, E. K., Dile, Y. T., Moges, M. A., Dersseh, M. G., Tegegne, G., & Kibret, S. (2020). Spatiotemporal dynamics and environmental controlling factors of the lake tana water hyacinth in Ethiopia. *Remote Sensing*, 12(17).
<https://doi.org/10.3390/RS12172706>
- Wu, B., Dai, S., Wen, X., Qian, C., Luo, F., Xu, J., Wang, X., Li, Y., & Xi, Y. (2022). Chlorophyll-nutrient relationship changes with lake type, season and small-bodied zooplankton in a set of subtropical shallow lakes. *Ecological Indicators*, 135, 108571.
<https://doi.org/10.1016/j.ecolind.2022.108571>
- Xiao, F., Ling, F., Du, Y., Feng, Q., Yan, Y., & Chen, H. (2013). Evaluation of spatial-temporal dynamics in surface water temperature of Qinghai Lake from 2001 to 2010 by using MODIS data. *Journal of Arid Land*, 5(4), 452–464.
<https://doi.org/10.1007/s40333-013-0188-5>
- Xie, C., Zhang, X., Zhuang, L., Zhu, R., & Guo, J. (2022). Analysis of surface temperature variation of lakes in China using MODIS land surface temperature data. *Scientific Reports*, 12(1), 1–13. <https://doi.org/10.1038/s41598-022-06363-9>
- Xie, Y., Qin, H., & Yu, D. (2004). Nutrient limitation to the decomposition of water hyacinth (*Eichornia crassipes*). *Hydrobiologia*, 529(1), 105–112.
<https://doi.org/10.1007/s10750-004-5494-7>
- Xie, Y., Sha, Z., & Yu, M. (2008). Remote sensing imagery in vegetation mapping: a review. *Journal of Plant Ecology*, 1(1), 9–23. <https://doi.org/10.1093/jpe/rtm005>
- Xu, H. (2006). Modification of normalised difference water index (NDWI) to enhance open water features in remotely sensed imagery. *International Journal of Remote Sensing*, 27(14), 3025–3033. <https://doi.org/10.1080/01431160600589179>
- Yagbasan, O., Demir, V., & Yazicigil, H. (2020). Trend analyses of meteorological variables and lake levels for two shallow lakes in central Turkey. *Water (Switzerland)*,

- 12(2), 1–16. <https://doi.org/10.3390/w12020414>
- Yan, S. H., Song, W., & Guo, J. Y. (2017). Advances in management and utilization of invasive water hyacinth (*Eichhornia crassipes*) in aquatic ecosystems—a review. *Critical Reviews in Biotechnology*, 37(2), 218–228. <https://doi.org/10.3109/07388551.2015.1132406>
- Yang, J., Yang, K., Zhang, Y., Luo, Y., & Shang, C. (2022). Maximum lake surface water temperatures changing characteristics under climate change. *Environmental Science and Pollution Research*, 29(2), 2547–2554. <https://doi.org/10.1007/s11356-021-15621-8>
- Yang, K., Yu, Z., & Luo, Y. (2020). Analysis on driving factors of lake surface water temperature for major lakes in Yunnan-Guizhou Plateau. *Water Research*, 184, 116018. <https://doi.org/10.1016/j.watres.2020.116018>
- Yang, K., Yu, Z., Luo, Y., Yang, Y., Zhao, L., & Zhou, X. (2018). Spatial and temporal variations in the relationship between lake water surface temperatures and water quality - A case study of Dianchi Lake. *Science of the Total Environment*, 624, 859–871. <https://doi.org/10.1016/j.scitotenv.2017.12.119>
- Yang, K., Yu, Z., Luo, Y., Zhou, X., & Shang, C. (2019). Spatial-Temporal Variation of Lake Surface Water Temperature and Its Driving Factors in Yunnan-Guizhou Plateau. *Water Resources Research*, 55(6), 4688–4703. <https://doi.org/10.1029/2019WR025316>
- Yin, F., Lewis, P. E., Gomez-Dans, J. L., & Wu, Q. (2019). *A Sensor Invariant Atmospheric Correction : Sentinel-2 / Msi and Landsat 8 / OLI*. 1–42.
- Yismaw, A. B., Workie, W. S., Alamirew, D. G., & Ayenew, W. A. (2024). Current Trend of Water Hyacinth Expasion and Investigation of Possible Cause for Water Hyacinth Using Remote Sensing in the Case Study of Lake Tana, Ethiopia. *Water, Air, and Soil Pollution*, 235(6), 1–16. <https://doi.org/10.1007/s11270-024-07215-0>
- Yu, Y., Zhang, H., & Lemckert, C. (2014). Salinity and turbidity distributions in the Brisbane River estuary, Australia. *Journal of Hydrology*, 519(PD), 3338–3352. <https://doi.org/10.1016/j.jhydrol.2014.10.015>

- Yu, Z., Yang, K., Luo, Y., Shang, C., & Zhu, Y. (2020). Lake surface water temperature prediction and changing characteristics analysis - A case study of 11 natural lakes in Yunnan-Guizhou Plateau. *Journal of Cleaner Production*, 276, 122689. <https://doi.org/10.1016/j.jclepro.2020.122689>
- Yue, S., & Wang, C. Y. (2004). The Mann-Kendall test modified by effective sample size to detect trend in serially correlated hydrological series. *Water Resources Management*, 18(3), 201–218. <https://doi.org/10.1023/B:WARM.0000043140.61082.60%3e>
- Zarkami, R., Esfandi, J., & Sadeghi, R. (2021). Modelling Occurrence of Invasive Water Hyacinth (*Eichhornia crassipes*) in Wetlands. *Wetlands*, 41(1). <https://doi.org/10.1007/s13157-021-01405-w>
- Zeng, H., Wu, B., Wang, S., Musakwa, W., Tian, F., Mashimbye, Z. E., Poona, N., & Syndey, M. (2020). A Synthesizing Land-cover Classification Method Based on Google Earth Engine: A Case Study in Nzhelele and Levhuvu Catchments, South Africa. *Chinese Geographical Science*, 30(3), 397–409. <https://doi.org/10.1007/s11769-020-1119-y>
- Zhang, G., Yao, T., Xie, H., Qin, J., Ye, Q., Dai, Y., & Guo, R. (2014) Estimating surface temperature changes of lakes in the Tibetan Plateau using MODIS LST data. *J Geophys Res Atmos* 119:8552–8567. <https://doi.org/10.1002/2014JD021615>
- Zhang, X., Xiong, Z., & Tang, Q. (2017). Modeled effects of irrigation on surface climate in the Heihe River Basin, Northwest China. *Journal of Geophysical Research*, 122(15), 7881–7895. <https://doi.org/10.1002/2017JD026732>
- Zhang, Y., Duan, H., Xi, H., Huang, Z., Tsou, J. Y., Jiang, T., & Liang, X. S. (2018). Evaluation of the Influence of Aquatic Plants and Lake Bottom on the Remote-Sensing Reflectance of Optically Shallow Waters. *Atmosphere - Ocean*, 56(4), 277–288. <https://doi.org/10.1080/07055900.2018.1454295>
- Zhang, Y. Y., Zhang, D. Y., & Barrett, S. C. H. (2010). Genetic uniformity characterizes the invasive spread of water hyacinth (*Eichhornia crassipes*), a clonal aquatic plant. *Molecular Ecology*, 19(9), 1774–1786. <https://doi.org/10.1111/j.1365->

294X.2010.04609.x

Zhao, D., Huang, J., Li, Z., Yu, G., & Shen, H. (2024). Dynamic monitoring and analysis of chlorophyll-a concentrations in global lakes using Sentinel-2 images in Google Earth Engine. *Science of the Total Environment*, 912(July 2023), 169152.

<https://doi.org/10.1016/j.scitotenv.2023.169152>

Zhao, Z., Islam, F., Waseem, L. A., Tariq, A., Nawaz, M., Islam, I. U., Bibi, T., Rehman, N. U., Ahmad, W., Aslam, R. W., Raza, D., & Hatamleh, W. A. (2024). Comparison of Three Machine Learning Algorithms Using Google Earth Engine for Land Use Land Cover Classification. *Rangeland Ecology and Management*, 92, 129–137.

<https://doi.org/10.1016/j.rama.2023.10.007>

Zimmels, Y., Kirzhner, F., & Malkovskaja, A. (2006). Application of *Eichhornia crassipes* and *Pistia stratiotes* for treatment of urban sewage in Israel. *Journal of Environmental Management*, 81(4), 420–428. <https://doi.org/10.1016/j.jenvman.2005.11.014>

APPENDIX

Table A1: Overall accuracy and *Kappa* coefficient of RF, CART, and SVM classifiers in post-rainy, dry, pre-rainy, and rainy seasons of Sentinel 2 and Landsat 8 images

Season	Classifier	Sentinel 2 MSI		Landsat 8 OLI	
		Overall Accuracy (%)	<i>Kappa</i> Coefficient	Overall Accuracy (%)	<i>Kappa</i> Coefficient
Post-rainy	RF	98.60	0.98	96.70	0.96
	SVM	97.80	0.97	93.96	0.92
	CART	98.00	0.97	95.54	0.94
Dry	RF	97.47	0.97	95.43	0.94
	SVM	97.19	0.96	93.91	0.92
	CART	96.93	0.96	94.00	0.92
Pre-rainy	RF	99.13	0.99	97.54	0.97
	SVM	98.54	0.98	95.90	0.95
	CART	97.67	0.97	96.31	0.95
Rainy	RF	98.04	0.97	97.63	0.97
	SVM	96.92	0.96	94.69	0.93
	CART	97.48	0.97	95.02	0.93

Table A2: F1 score, user and producer accuracy of water hyacinth class in post-rainy, dry, pre-rainy, and rainy season using RF, CART, and SVM algorithms in Sentinel 2 and Landsat 8 datasets

Season	Machine learning algorithms	User Accuracy (%)	Producer Accuracy (%)	F1-Score (%)
Sentinel 2 MSI				
Post-rainy	SVM	100.00	100.00	100.00
	CART	100.00	100.00	100.00
	RF	100.00	100.00	100.00
Dry	SVM	96.15	91.46	93.75
	CART	93.62	96.70	95.14
	RF	97.44	92.68	95.00
Pre-rainy	SVM	97.94	100.00	98.96
	CART	98.92	96.84	97.87
	RF	100.00	100.00	100.00
Rainy	SVM	100.00	100.00	100.00
	CART	100.00	98.78	99.39
	RF	100.00	100.00	100.00
Landsat 8 OLI				
Post-rainy	SVM	97.89	100.00	98.94
	CART	98.88	98.88	98.88
	RF	97.89	100.00	98.94
Dry	SVM	89.41	88.37	88.88
	CART	93.02	97.56	95.24
	RF	93.26	96.51	94.86
Pre-rainy	SVM	91.38	92.98	92.17
	CART	90.00	94.74	92.31
	RF	93.22	96.49	94.83
Rainy	SVM	88.24	97.4	92.59
	CART	94.44	94.44	94.44
	RF	96.04	97.00	96.52

Table A3: Water hyacinth spatial coverage in Lake Tana from 2015 to 2023

	Jan	Feb	Mar	Apr	May	Jun	Jul	Aug	Sep	Oct	Nov	Dec
2015	nd	nd	nd	nd	nd	nd	nd	nd	nd	2.51	2.81	2.49
2016	2.04	2.39	2.00	1.92	nd	1.08	nd	nd	3.95	4.47	4.98	4.28
2017	3.89	3.50	2.72	2.72	2.15	1.80	nd	nd	6.45	10.01	11.26	9.09
2018	8.80	7.52	5.91	5.13	4.09	3.54	nd	nd	16.57	17.28	20.48	20.86
2019	16.15	14.40	6.95	4.92	4.29	3.13	nd	11.09	14.16	21.91	24.69	21.42
2020	17.87	12.77	8.26	7.31	5.99	5.66	nd	nd	23.58	18.27	16.65	13.34
2021	8.74	5.94	4.14	3.02	3.17	3.35	nd	nd	20.70	23.35	22.65	16.12
2022	12.89	6.77	4.41	3.55	3.27	2.57	nd	nd	7.43	8.43	10.43	9.05
2023	6.51	4.03	2.89	2.53	2.08	2.78	nd	nd	10.62	13.64	16.13	15.25

Where nd: no data